Dissertation
submitted to the
Combined Faculties for the Natural Sciences and for Mathematics
of the Ruperto-Carola University of Heidelberg, Germany
for the degree of
Doctor of Natural Sciences

Put forward by
M.Sc. Giulia Aricó
Born in : Palermo, Italy
Oral Examination : November 23^{rd}, 2016

Ion Spectroscopy for improvement of the Physical Beam Model for Therapy Planning in Ion Beam Therapy

Referees:	Prof. Dr. Wolfgang Schlegel
	Prof. Dr. Oliver Jäkel

Ai miei genitori, per il loro amore.
A Riccardo e Mareike,
per il loro supporto costante.
A mio fratello Gabriele,
per aver sempre creduto in me.

To my parents, for their love.
To Riccardo and Mareike,
for their constant support.
To my brother Gabriele,
who has always believed in me.

Gutta cavat lapidem (Titus Lucretius Carus)

Declaration

I declare here that this Ph.D. thesis is the result of my own research, and that all sources used in this work have been duly referenced.
This thesis has not been submitted to any other university or institute for a degree award.

Date : ....
Name : ....
Signature : ....

Zusammenfassung

Im Vergleich zur Photonen- und Protonentherapie zeichnen sich Helium- und Kohlenstoffionen durch eine höhere konformale Dosisverteilung, kleinere Halbschatten und eine höhere relative biologische Wirksamkeit aus. Durch nukleare Fragmentierung im Patientengewebe können die Teilchen jedoch zerfallen und die hierdurch entstehenden sekundären Fragmente die applizierte biologische Dosisverteilung beeinflussen. Zurzeit besteht Forschungsbedarf über die nuklearen Fragmentierungsprozesse. Ein Grund hierfür ist der sehr große (bis zu mehreren Metern) experimentelle Aufbau, der für die Untersuchungen nötig ist. In dieser Arbeit wird eine neue Methode vorgestellt die auf der Bestimmung von Spurpunkten der Teilchen mit handlichen, pixel-basierten Halbleiterdetektoren (Timepix) und der Mustererkennung ihrer Signale basiert.

Die Messungen wurden am HIT durchgeführt. Es wurden gemischte Strahlenfelder untersucht, die durch 430 MeV/u Kohlenstoff- und 220 MeV/u Heliumionenstrahlen in Wasser- und PMMA-Phantomen entstehen. Die Anzahl an primären (Kohlenstoff- oder Helium-) Ionen, die hinter Phantomen mit gleicher wasseräquivalenter Dicke (water equivalent thickness - WET) detektiert wurden, stimmte innerhalb der statistischen Unsicherheiten überein. Allerdings wurden mehr Fragmente (Differenzen bis zu 20% bei H) und schmalere laterale Teilchenverteilungen hinter PMMA- als hinter Wasserphantomen beobachtet.

Die Ionenspektren hinter Gewebesurrogaten und entsprechenden Wasserphantomen mit gleicher WET wurden ebenfalls analysiert. Für Fett- und inneres Knochengewebe und den äquivalenten Wasserphantomen wurden konsistente Ergebnisse innerhalb der Unsicherheiten erzielt. Signifikante Unterschiede wurden für Lungen- und kortikales Knochengewebe – verglichen zu den Wasserphantomen – gemessen.

Die experimentellen Ergebnisse wurden mit FLUKA Monte Carlo Simulationen verglichen. Dieser Vergleich könnte dazu beitragen die Wechselwirkungsmodelle für ^{12}C-Ionen- und ^{4}He-Ionenstrahlen zu verbessern.

Abstract

Helium and carbon ions enable a more conformal dose distribution, narrower penumbra and higher relative biological effectiveness than photon and proton radiotherapy. However, they may undergo nuclear fragmentation in the patient tissues and the arising secondary fragments affect the delivered biological dose distributions. Currently there is a lack of data regarding ion nuclear fragmentation. One reason is the large size (up to some meters) of the experimental setups required for the investigations. In this thesis a new method is presented, which makes use of versatile pixelated semiconductor detectors (Timepix). This method is based on tracking of single particles and pattern recognition of their signals in the detectors.

Measurements were performed at the HIT facility. The mixed radiation field arising from 430 MeV/u carbon ion beams and 221 MeV/u helium ion beams in water and in PMMA targets was investigated. The amounts of primary (carbon or helium) ions detected behind targets with the same water equivalent thickness (WET) were found to be in agreement within the statistical uncertainties. However, more fragments (differences up to 20% in case of H) and narrower lateral particle distributions were measured behind the PMMA than the water targets.

The spectra of ions behind tissue surrogates and corresponding water targets with the same WET were analysed. The results obtained with adipose and inner bone surrogates and with the equivalent water phantoms were found to be consistent within the uncertainties. Significant differences in the results were observed in the case of lung and cortical bone surrogates when compared to the water phantoms.

The experimental results were compared to FLUKA Monte Carlo simulations. This comparison could contribute to enhance the ion interaction models currently implemented for ^{12}C and ^{4}He ion beams.

Contents

5 Method 41

1 Introduction

Radiotherapy is together with surgery the most employed and efficient technique currently used to treat cancer patients [Joiner and Kogel 2009]. In many cases it is a valid alternative to chemotherapy. More than 50% of the patients with localized malignant tumors receive radiotherapy treatments during the care process [Schardt, Elsässer, and Schulz-Ertner 2010]. The main and challenging goal of radiotherapy is to kill the malignant cells and simultaneously spare the healthy tissues as much as possible.

X-rays were first exploited, since the late 19th century, for tumor treatments. As a consequence of the free radicals formation, the DNA of cells along the photon beam can be damaged. X-rays exhibit a maximum of dose close to the patient's skin and the dose decreases with increasing depth. It is therefore challenging to spare the tissues in front and behind the target, especially in case of deep-seated tumors.

In 1946 R.R. Wilson suggested the use of accelerated protons [Wilson 1946], recognizing their advantages for cancer therapy: the depth-dose profile of a monoenergetic proton beam is characterized by a sharp peak (the Bragg peak) at the end of the particle range. Consequently, it might be easier to deliver the prescribed dose in a deep-seated tumor while the surrounding normal tissues are better spared than in conventional radiotherapy. The first clinical application of protontherapy took place in 1954, at the Lawrence Berkeley National Laboratory in USA, followed by many other facilities around the world.

Beside protons, other ion types have also been investigated, from helium to argon, to find the best suited particle species for cancer treatments [Chen, Castro, and Quivey 1981, Fowler and Perkins 1961, Tobias et al. 1964]. The depth dose curve of heavy ions is also characterized by a Bragg peak, which becomes sharper with increasing the particle mass and charge. Indeed, heavier particles show lower beam broadening and lower range straggling [Kempe, Gudowska, and Brahme 2007], which enables more conformal dose distributions in the target to be achieved. Moreover, heavy ions, e.g carbon ions, have higher linear energy transfer (LET) and therefore a higher radiobiological effectiveness (RBE) in the Bragg peak than protons [Schlegel, Bortfeld, and Grosu 2006], as well as an advantageous low oxygen enhancement ratio. These features make them particularly efficient against radioresistant tumors. However, heavy ions lose significantly more energy along their path than protons, and therefore the initial particle energy has to be significantly higher to achieve the same penetration depth. This implies larger and more expensive particle accelerators. Moreover, ions heavier than protons might undergo fragmentation in the patient tissues and the arising fragments also contribute to the dose distribution, both inside and outside the target. These processes are more relevant with increasing particle charge and energy. For example, Figure 1.1 shows the depth-dose profiles for a carbon (left) and a helium ion beam (right). The contributions to the dose from the primary particles and from the secondary fragments are illustrated. As their physical and biological properties are different to the primary ions, secondary fragments need to be properly considered in the treatment planning system to assure accurate and safe treatments of the patients. Indeed, as Figure 1.1 shows, the contribution from the fragments is mainly in front and behind the Bragg peak, where healthy tissues are usually located.

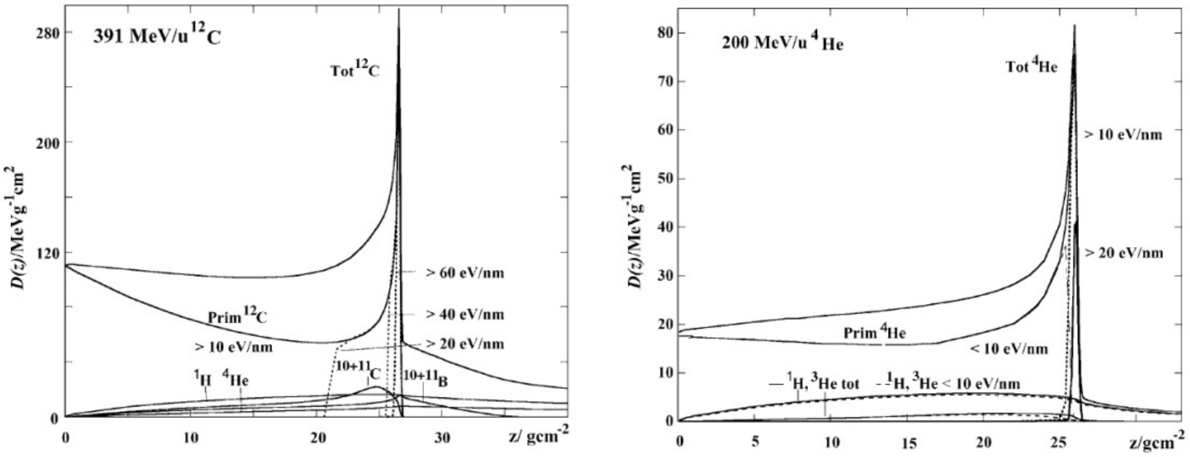

Figure 1.1: Examples of simulated dose contributions from primary and secondary particles. *Left*: Depth-Dose distribution of a 391 MeV/u carbon ion beam in soft tissue. The dose distributions of the primaries are divided based on their LET [eV/nm] components. *Right*: Depth-Dose distribution of a 200 MeV/u helium ion beam in water. The dose distributions of the particles are divided based on their LET [eV/nm] components. Reprinted from [Kempe, Gudowska, and Brahme 2007].

Carbon ions have generated the greatest interest among the heavy ion species, as they were found to provide a superior balance between tumor cell killing and normal tissue sparing. The first full clinical radiotherapy treatment with carbon ions took place in 1994 at NIRS/HIMAC in Japan, followed by GSI in Germany, in 1997. Since 2009 protons and carbon ions are used at the Heidelberg Ion-Beam Therapy center (HIT) to treat cancer patients. Relevant benefits have been achieved in the case of carcenrs of the head and neck, skull base, lung, liver, prostate, and rectal cancers, as reported in Combs et al. 2012, in Rieken et al. 2012 and in Kamada et al. 2015.
Alternative particles to protons and carbon ions are still investigated: for instance, the potential advantages of helium ions, in terms of physical characterization and biological effectiveness, were analysed in several studies [e.g. Gallas 2016, Krämer et al. 2016, Mairani et al. 2016, Tessonnier et al. 2015]. With respect to protons, helium ion beams exhibit sharper penumbra due to the greater mass [Ströbele et al. 2006]. In comparison to carbon ions, helium ion beams have reduced fragmentation tail and lower biologi-

cal effectiveness. Those characteristics might be advantageous, especially in pediatric treatments [Krämer et al. 2016], where the long term effects due to an exposure to high-RBE-particle beams haven't been sufficiently investigated yet. Moreover, helium ions can be produced and accelerated at the energies required for radiotherapy more easily than carbon ions. Hence, operating costs would be strongly diminished. Helium ion beams are planned to be used clinically at HIT from 2017 [Mairani, Tessonnier, and Dokic 2016].

An important challenge in hadrontherapy concerns the possibility to accurately calculate and predict the delivered dose in the treatment planning systems. A lack of experimental data and research investigations describing the different aspects of nuclear fragmentation processes is currently an issue. The main studies on carbon ion attenuation and build-up of the secondary fragments were carried out by Schall et al. 1996, Gunzert-Marx et al. 2008, Matsufuji et al. 2011 and Haettner et al. 2013. These studies, described in more detail in Section 3.3, required very large experimental apparatuses and provided data only in a limited range of experimental configurations.

Ionization chambers, calibrated with a ^{60}C beam, are used to measure the absorbed dose to water [Andreo et al. 2000]. However, the development of gantries and dynamic beam scanning systems for radiotherapy treatments requires different and more efficient dosimetry systems. For instance, the use of water phantoms in gantries is not possible at great rotation angles. A practical and widespread alternative is the use of solid Polymethyl methacrylate (PMMA) phantoms, for dosimetric measurements. Moreover, while the treatment planning systems calculated dose to water, the results obtained from Monte Carlo simulations refers to dose to tissue. Therefore, dose to material need to be converted into dose to water (as described in Section 3.1.5). A deeper knowledge of the influence of the material elemental composition on the ion fragmentation and scattering could enable an improvement in the accuracy of the currently used correction factors.

The goal of the present thesis was to investigate validity and limits in the equivalence between water and PMMA, and between tissue equivalent materials and water: beam attenuation, build-up of secondary particles and lateral particle distributions were analysed for carbon ion and helium ion beams.

2 Aims of the thesis

The Timepix devices, described in Section 4.2.3, were employed for single particle detection. They have been successfully used within the research group at DKFZ for several years, mainly to develop a non-invasive method for carbon ion beam monitoring [Gwosch et al. 2013] and for ion spectroscopy [Hartmann et al. 2012]. These detectors allow more manageable, more versatile and smaller experimental setups than those previously used, which exploited time of flight measurements and telescope detectors (see Section 3.3). The other experimental setups require several meters of space.
In the new method for ion spectroscopy, proposed in Hartmann et al. 2012 and based on the Timepix detectors, the pattern recognition of the particle signals generated in these detectors are used to differentiate between particle species, as explained in Section 5.4.2. The same basic principle was used in this thesis to investigate the fragmentation processes of carbon and helium ions in different materials of clinical interest. The main contribution introduced in this work with respect to the previous method regards the time coincidence measurements, which allow tracking of the single particles in front of the target (incoming primary ions) and behind the target (outgoing primary or secondary particles) and to correlate the particles belonging to the same event. An absolute normalization of the data and analysis of fragments produced by each single incoming primary ion was possible.

Three main studies were carried out:

Study 1: *Fragmentation of Carbon Ions in Water and in PMMA* (Section 6.2)

This study was designed to be sensitive to the fragmentation cross sections of carbon ions in two materials commonly used in dosimetric measurements: water and PMMA. Targets, which in pair have the same water equivalent thickness, were used to compare the products of the physical processes and the lateral particle distributions behind the targets. The experimental results were also compared with FLUKA Monte Carlo simulations. Monte Carlo codes are clinically implemented as a support and to validate the analytical treatment planning systems [Böhlen et al. 2013 and Battistoni et al. 2016]. The results from this study can be used to benchmark the Monte Carlo codes, and therefore to improve the physical beam models.

Study 2: *Fragmentation of Helium Ions in Water and in PMMA* (Section 6.3)

For helium ions, the lack of experimental data regarding the fragmentation cross sections is an even greater issue than for carbon ions. Therefore beam attenuation and build-up of the secondaries were analysed in this thesis for helium ion beams crossing the same water and PMMA targets used in Study 1. The results achieved in this study can be used to gain a deeper knowledge on the physical processes occurring in helium ion beams, prior their use in the clinical practice (planned at HIT starting from 2017). Comparisons between experimental results and FLUKA simulations were carried out also in this case.

Study 3: *Fragmentation of Carbon Ions in Tissue and in Water* (Section 6.4)

Conversion factors to compare the dose to water, calculated in the treatment planning systems, and dose to tissue, calculated in the Monte Carlo algorithms, (see Section 3.1.5 for more details), are required. This study was designed to investigate the validity and limits in the equivalence between tissue equivalent materials and water, in terms of the physical processes occurring in carbon ion beams. The achieved results can be used to improve the accuracy of the conversion factors.

3 Background

Each radiation particle used in radiotherapy traveling within a medium interacts with the material atoms and transfers a certain amount of energy. This energy can excite or ionize the atoms of the media. The ionization can be produced directly by the charged particle, or via an indirect process. For instance, x-rays, γ-rays and neutrons produce secondary charged particles, which are responsible for the chemical and biological damages. The main challenge in radiotherapy is to maximize the radiation damage in the tumor cells, maintaining the normal tissue toxicity as low as possible (ALARA principle).

Nowadays, photons are the most used particles in radiotherapy. They provide successful results in many clinical indications. However, in case of deep-seated and radioresistant tumors, charged particles like protons and heavier ions might offer some advantages over photons. Above all, a more conformal dose to the target can be achieved. The absorbed dose is the most important physical measure in radiotherapy. It is defined as the mean energy, dE, deposited in a mass element, dm:

$$D = \frac{dE}{dm} \qquad \left[Gy = \frac{J}{kg} \right] \tag{3.1}$$

However, accurate calculations of the delivered dose may be challenging, especially in case of mixed fields and in particularly complex clinical configurations. The quantities minimum dose in the tumor, and maximum dose in normal tissues are commonly used to estimate the efficacy and possible side effects of the treatment. The interaction processes of photons, protons and heavier ions in matter and the resulting depth-dose distributions are described and compared in the following.

Photons traveling through an absorber lose energy via stochastic interactions. Depending on the particle energy, the dominant process are the photoelectric effect, the Compton scattering or the pair production. The transfer of energy to the material takes place via the arising secondary electrons. The characteristic absorption curve of photons shows an initial build-up followed by an exponential decrease, as illustrated in Figure 3.1. The build-up region is due to the low amount of secondary electrons produced at the interface between media with different densities. A maximum in the delivered dose is reached when the electronic equilibrium is established. The depth of this region is roughly equal to the most probable range of the secondary electrons, which depends on the photon beam energy [Marcu, Bezak, and Allen 2012]. The characteristic of the subsequent decrease mainly depends on the material and on the initial beam energy.

Due to their depth dose profile, photons are not particularly indicated for deep-seated tumors. Moreover, they exhibit a rather high lateral spread when compared to protons and heavier particles.

Protons traversing a medium interact electromagnetically with the atomic nuclei and can be deflected, or mainly interact with the atomic electrons and are slowed down till they stop. In the therapeutic energy range (40-220 MeV), Coulomb interactions between the projectile protons and the orbiting electrons of the target atoms are the predominant effects [Linz 2012]. Due to the greater masses, protons lose only small amounts of their energies in each interaction with the electrons. The depth-dose of protons (illustrated in Figure 3.1) shows an initial plateau region. A large amount of the particle energy is deposited just at the end of the range, resulting is the so called Bragg peak. Behind the Bragg peak, the energy deposition decreases rapidly. The depth of the Bragg peak, and therefore the proton range, is proportional to the square of the kinetic energy.
In many cases, proton beams allow to better localize the dose in the target than conventional radiotherapy, especially in case of deep-seated tumors.

Ions heavier than protons, like helium and carbon ions, have a depth dose profile similar to protons, as shown in Figure 3.1. However, heavier particle beams are characterized by sharper Bragg peaks and a lower lateral spread. Therefore, a more conformal dose into the target and a better spare of the tissues surrounding the tumor might be achieved. However, ions heavier than protons exhibit a tail behind the Bragg peak, due to lighter fragments produced from nuclear collisions with the target nuclei.

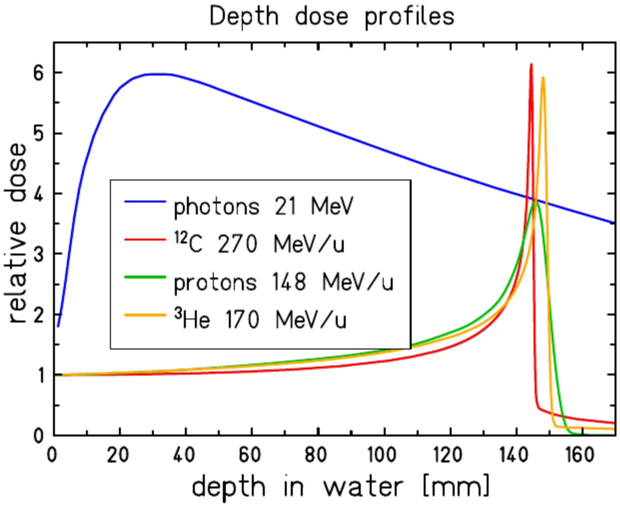

Figure 3.1: Simulated dose distributions for a 21 MeV photon beam, a 148 MeV/u proton beam, a 170 MeV/u ^{3}He beam and a 270 MeV/u ^{12}C. Reprinted from Krämer et al. 2016

In this thesis the nuclear interactions of helium and carbon ions were investigated in different materials. The secondary particles may deliver dose to healthy tissues surrounding the tumor. Therefore, they need to be accurately considered in the treatment planning, for an accurate estimation of the side effects. In this chapter the physical and biological characteristics of helium and carbon ion beams are presented.

3.1 Physical basis of ion radiotherapy

3.1.1 Stopping power and range

The main physical quantities of interest in ion radiotherapy are the particle energy loss and the particle range. The stopping power, S, refers to the mean energy loss, $\overline{dE}$, by a particle in a path length dx of a material:

$$S = -\left(\frac{\overline{dE}}{dx}\right) \tag{3.2}$$

In general, three factors contribute to the total stopping power: the energy lost in inelastic collisions with the target electrons (collision stopping power, S_{col}), the energy transferred to the target nuclei (nuclear stopping power, S_{nucl}), and the energy lost due to bremsstrahlung (radiative stopping power, S_{brem}). However, for charged particles heavier than electrons and with typical energies used in radiotherapy, the energy lost because of interactions with the target nuclei and because of bremsstrahlung can in general be neglected. Indeed, the nuclear stopping power becomes significant only at ion energies below 10 kev/u. As those energies are reached just in the last few μm of the particle path, the contribution to the delivered dose arising from the nuclear interactions is negligible. Hence, the collision stopping power, S_{col}, is the most dominant component for ions in the therapeutic energy range. Bethe first provided a formula to calculate S_{col}, in 1930. This formula was then enhanced for low energetic particles and additional correction factors were added. The relativistic version, including shell and density effect correction terms, is [Zeitling et al. 2007]:

$$S_{col} = \frac{4\pi n Z_{eff}^2}{m_e c^2 \beta^2} \left(\frac{e^2}{4\pi\epsilon_0}\right)^2 \left[ln\left(\frac{2m_e c^2\beta^2}{(1-\beta^2)}\right) - \beta^2 - ln < I > - \frac{C}{z} - \frac{\delta}{2}\right] \tag{3.3}$$

where n is the electron density of the target, Z_{eff} is the projectile effective charge, m_e is the rest mass of the electron, c is the speed of light, $\beta = v/c$, v is the velocity of the projectile particles, e is the electron charge, ϵ_0 is the vacuum permittivity, I is the mean excitation potential of the target, C is the shell correction factor, z is the atomic number of the target, and δ is the density correction factor.
The term Z_{eff} takes into account the possibility that some projectiles capture electrons

from the target. Consequently, their effective charges may be reduced. These effects decrease with increasing beam energy.
The mean ionization, $< I >$, corrects for the quantized energy levels of the target electrons, band gaps in solids and material phase changes.
The shell correction factor, C/z, takes into account the non-stationary state of the electrons in the target, i.e. corrects for the assumption that the projectile velocity is much higher than those of the bound electrons.
The density effect term, $\delta/2$, takes into account polarization effects due to dielectric properties of the target [Zeitling et al. 2007]. This effect increases with increasing beam energy and density of the material.

From the Bethe-Bloch formula (Equation 3.3), it can be derived that the maximum energy loss rate is achieved when the projectile velocity is equal to $Z_{eff}^{2/3}v_0$, where v_0 is the Bohr velocity ($v_0 = e^2/\hbar$).

The mean particle range, R, is the mean path length traveled by a particle before stopping within a medium. In the continuous slowing down approximation (CSDA), the mean particle range can be obtained from the stopping power as:

$$R(E) = \int_0^E \left(\frac{dE}{dx}\right)^{-1} dE \tag{3.4}$$

Due to multiple Coulomb scattering (discussed in Section 3.1.3) along the particle path, the projected particle range is shorter than the total one. This effect is lower for heavier ions. Statistical fluctuations in the energy loss also influence the particle range, as discussed in the next section.

3.1.2 Energy loss straggling and range straggling

The Bethe Bloch formula (Equation 3.3) only refers to the mean particle energy loss in the unit path length dx. Beside the initial beam energy spread, statistical fluctuations in the number of interactions the particles are subjected to also occur. These fluctuations cause an energy loss straggling and consequently a smearing of the Bragg peak. The effect is less relevant for heavier particles, as it can be seen in Figure 3.1.
The statistical fluctuations in the energy deposited in the detector are important in this work, as they limit the resolution of the energy measurements. Pattern recognition of the particle signal generated in the used Timepix detectors was exploited to differentiate between particle species (see Section 4.2.3 and Section 5.4.2 for more details).
The energy loss distributions depend on the number of interactions occurring within the media. The discriminating parameter, k, is defined as the ratio between the mean energy loss, $\overline{\Delta E}$, and the maximum energy which can be transferred by the projectile particle in a single collision with the atomic electrons, E_{max}:

$$k = \frac{\overline{\Delta E}}{E_{max}} \tag{3.5}$$

Ignoring the logarithmic term and the correction factors in the Bethe Block equation, $\overline{\Delta E}$ can be obtained by the free electron (Rutherford) cross section and approximated by:

$$\overline{\Delta E} = \frac{2\pi Z^2 e^4 N_A z \rho x}{m_e \beta^2 c^2 A} \tag{3.6}$$

where Z is the projectile charge, N_A is the Avogadro's number, z, A, ρ and x are the atomic number, the atomic weight, the density and the thickness of the medium.
E_{max} is given by:

$$E_{max} = \frac{2m_e \beta^2 \gamma^2}{1 + 2\gamma m_e/M + (m_e/M)^2} \tag{3.7}$$

where m_e is the rest mass of the electron, $\beta = v/c$, v is the velocity of the projectile particle, c is the speed of light, $\gamma = E/M$, E and M are the energy and the mass of the projectiles. The theoretical calculations of the energy loss distributions have different regions of applicability, depending on the thickness of the medium. Thick absorbers are defined for k>10, whereas an absorber is considered thin for $k \leqslant$10.
In the first situation (k>10), a high number of interactions occurs in the medium. Although a small amount of energy is lost in each collision with the target electrons due to the higher masses of the incoming particles, the cumulative effect of multiple processes leads to the loss of all or most of the projectile energy within the thick absorber. Applying the central limit theorem, the energy loss distribution, f, can be approximated by a Gaussian distribution:

$$f(\Delta E) = \frac{1}{\sqrt{2\pi}\sigma} e^{(\Delta E - \overline{\Delta E})^2/2\sigma^2} \tag{3.8}$$

where ΔE is the energy loss in the target and σ is the standard deviation of the distribution.
For thin targets, two theoretical calculations of the distributions were provided by Landau (for $k \leqslant$0.01) [Landau 2007] and by Vavilov (for 0.01$\leqslant$ $k \leqslant$10). The Landau probability distribution, f_L, of a particle of mass M is given by:

$$f_L(x, \Delta E) = \frac{\phi(\lambda)}{\overline{\Delta E}} \tag{3.9}$$

where $\phi(\lambda)$ is the Landau function, defined as:

$$\phi(\lambda) = \frac{1}{2\pi i}\int_{c+i\infty}^{c-i\infty} e^{(u\ln u+\lambda u)du} \qquad c \geq 0 \tag{3.10}$$

with:

$$\lambda = \frac{\epsilon - \bar{\epsilon}}{\overline{\Delta E}} - \gamma' - \beta^2 - \ln\frac{\overline{\Delta E}}{E_{max}} \tag{3.11}$$

where ϵ is the actual energy loss in the target, $\overline{\Delta E}$ is the mean energy loss, $\gamma' = 1 - \gamma$ and γ is the Euler's constant. The Landau distribution is asymmetric, with a tail till E_{max}, and a peak at the most probable energy loss, ΔE_P, given by [Meroli, Passeri, and Servoli 2011]:

$$\Delta E_P = \overline{\Delta E}\left[\ln\frac{2m_e c^2\beta^2\gamma^2}{I^2} + \ln\frac{\Delta E}{I} + 0.2 - \beta^2 - \delta\right] \tag{3.12}$$

where I is the mean ionization potential and δ is the density correction (discussed in Section 3.1.1). The ΔE_P value is lower than the mean energy loss in the Bethe-Bloch formula (Equation 3.3). This formalism is valid in the approximation that the energy loss is much smaller than the maximum energy transferred in each collision ($k \leqslant 0.01$), and that the energy loss is great in comparison to the binding energy of the most bounded electrons.
Vavilov considered the spin of the incident particle and kinematic limits on the maximum energy which can be transferred in each collision [Meroli, Passeri, and Servoli 2011], in order to obtain a more accurate theory. In the Vavilov formalism, the assumption that the typical energy loss is smaller than the maximum energy transferred in each collision is removed. The Vavilov theory tends to the Landau distribution for $k \leqslant 0.01$, and coincides with the Gaussian distribution for $k>10$. Further corrections on the Vavilov theory were introduced by Blunch, Leisegang, Shulek and Bichsel to take into account the electron binding energy and the atomic shell structure [Meroli, Passeri, and Servoli 2011]. The resulting energy straggling function can be obtained as a convolution of the Landau distribution with a normal distribution.

As a consequence of the energy loss straggling, a range straggling also occurs. In thick targets (that is for 2 cm$<$*target thickness*$<$40 cm), the distribution of ranges of a monoenergetic beam can be approximated by a Gaussian distribution. The width of the distribution is almost proportional to the particle residual range and inversely proportional to the square root of the particle mass number [Ma and Lomax 2012]. The dependency of the range straggling, s_R, on the mass, M, of any particle heavier than proton is given by [Ahlen 1980]:

$$s_R \propto \sqrt{\frac{m_p}{M}}R \tag{3.13}$$

where m_p is the proton mass. As examples, the range straggling in tissue is about 1% of the mean range for protons, and about 0.3% for carbon ions. Moreover, it is about 50% lower for helium ions than for protons [Linz 2012]). The relationship between range of a proton and of any heavier ion is:

$$R_{Heavy\,Ion} = \frac{M}{Z^2} R_{proton} \tag{3.14}$$

where M and Z are the mass and atomic number of the heavy particle, and

3.1.3 Lateral scattering

Charged particles traversing a medium interact with the Coulomb field of the target nuclei. This results in a deflection of the particle trajectory, called Coulomb scattering. The Rutherford collision cross section, σ_R, can be used to describe the Coulomb scattering. Neglecting spin and screening effects, it is given by:

$$\frac{d\sigma}{d\Omega} = \left(\frac{Zze^2}{16\pi\epsilon_0 E}\right)^2 \frac{1}{\sin^4\left(\frac{\theta}{2}\right)} \tag{3.15}$$

where Z and E are the projectile particle charge and kinetic energy, z is the target nucleus charge, and θ is the deflection angle. Although deflections at small angles have higher probability than large angle scattering, the cumulative effect of many deflections (called multiple Coulomb scattering) along the particle path may result in a significant lateral spread of the beam. The effect is more relevant for lighter than for heavier ions: in general, the lateral beam spread is about 2 times lower for helium ions than for protons, and about 3.5 times lower for carbon ions [Linz 2012].
The lateral distribution of ion beams for small scattering angles can be described by the Moliére theory [Bethe 1952]. According to it, in the central part of the beam, the lateral displacement can be approximated by a Gaussian distribution, whose standard deviation, σ_θ, was obtained empirically [Highland 1975]:

$$\sigma_\theta[rad] = 14.1MeV \frac{Z}{p\beta c}\sqrt{\frac{x}{L_{rad}}}\left(1 + \frac{1}{9} log_{10}\left(\frac{x}{L_{rad}}\right)\right) \tag{3.16}$$

where Z, p and $v = \beta c$ are the projectile charge, momentum and velocity, respectively, x is the penetration depth, and L_{rad} is the radiation length of the target material (L_{rad} values are available in Tsai 1974).

In this thesis the lateral distributions of the primary and secondary particles were investigated behind different materials. The measured lateral distributions of the outgoing particles can be due to the cumulative effect of small angle scattering or to single deflections at great angle. The probability of large angle deflections decreases with increasing angle and particle mass, while the cumulative effect of many small angle deflections becomes higher with increasing target thickness. Moreover, for two materials with different chemical compositions, the lateral spread at the same thickness normalized to density is larger for the target with heavier elements [Schardt, Elsässer, and Schulz-Ertner 2010].

3.1.4 Fragmentation

As mentioned at the beginning of this chapter, the depth-dose profile of ion beams is particularly advantageous in case of deep-seated tumor. However, the benefits offered by ion radiotherapy may be deteriorated by nuclear fragmentation of the primary ions along the beam path. As a consequence, a loss of primary particles and a production of secondary lighter fragments can be observed. These effects become more relevant with increasing the primary particle masses, the particle energies, the density of the medium and the penetration depth.

A simple model used to describe the fragmentation processes of the primary particles is the so called abrasion-ablation model [Schardt, Elsässer, and Schulz-Ertner 2010]. It is based on geometrical arguments and it is illustrated in Figure 3.2.

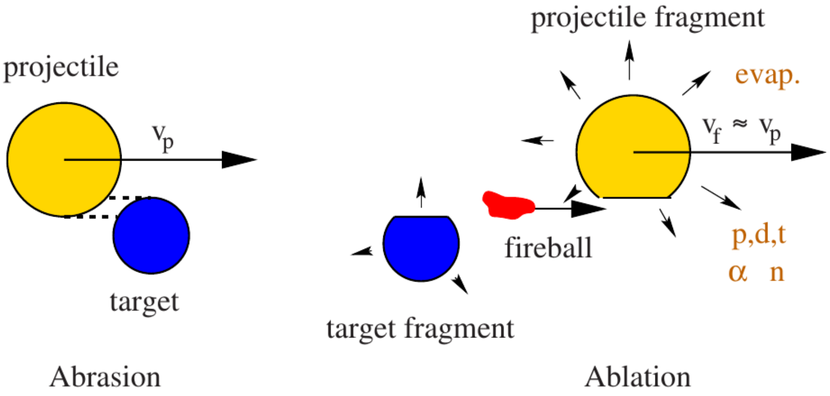

Figure 3.2: Illustration of the abrasion-ablation model, which describes the peripheral interactions of high energetic particles with target nuclei, based on geometrical arguments. Reprinted from Schardt, Elsässer, and Schulz-Ertner 2010.

When a projectile particle interacts with a target nucleus, nucleons in the overlapping area are sheared off (abrasion), while the other nucleons are slightly affected by the interaction process. The projectile-fragment and target-fragment have smaller charges and masses than the original projectile and target nucleus. However, the influence on the velocity and direction of the projectile are rather small, and the momentum transferred to the target nucleus can, in first approximation, be neglected. In addition to

the projectile-fragment and target-fragment, a hot area, called fireball, is created, which contains highly excited nucleons both from the projectile and from the target nuclei. Therefore, the fireball travels with an intermediate velocity between the projectile's and the target's one.
Subsequently to the interaction process, the highly excited projectile-fragment, target-fragment and fireball de-excite by evaporation of nucleons and clusters (ablation).
Nucleons arising from the target-fragment are emitted isotropically and at low velocities. As these nucleons have short ranges, they deposit their energy locally in the proximity of the target-fragment. The nucleons arising from the projectile-fragment and the projectile-fragment itself have approximately the same velocity as the projectile particle, but smaller masses and charges. Therefore, they may travel farther than the primary particles and generate the fragmentation tail shown in Figure 3.1. This tail becomes more relevant with increasing mass and energy of the primary particles. Just behind the Bragg peak, the main contribution arises from the heavier fragments, till they are slowed down. At larger depth, only lighter fragments are present, which are produced from the primary particles or are generated from subsequent fragmentation processes of the heavier fragments [Gunzert-Marx et al. 2008]. The lateral distributions of the fragments emitted from the projectile-fragment and from the fireball are rather forward peaked, due to the high velocity of the projectile-fragment and of the fireball. However, they contribute to broaden the beam laterally, and the effect is higher with decreasing particle mass. Moreover, scattering along the particle paths also influences the beam spread. Due to the lower masses, the cumulative effect of multiple Coulomb scattering is higher for lighter particles, as discussed in Section 3.1.3.

In this thesis beam attenuation, build-up of secondary particles and lateral distributions both of the primary and of secondary particles were investigated. The gained information can be used to evaluate the contribution to the dose from the fragments and to improve the physical beam models in the treatment planning systems.
In the Monte Carlo codes more advanced and accurate models than the abrasion-ablation one are implemented to reproduce the inelastic nucleus-nucleus interactions. A description of the FLUKA Monte Carlo code, used in this thesis, and of its physics models, as regards applications in ion radiotherapy, can be found in Section 4.3.

3.1.5 Dose to water and dose to material

The ion fragmentation processes depend on the initial particle type and energy, and also on the chemical composition and thickness of the medium. Therefore, the physical properties of the material influence the calculations and the measurements of the dose distributions.

In dosimetry water phantoms are widely used. However, PMMA targets are sometimes used in place of the water phantoms, as they enable a higher positioning accuracy and also measurements at greater rotation angles in a gantry [Lühr et al. 2011]. The differences in the chemical compositions and geometrical thicknesses between water and PMMA targets may influence the outcomes of the dosimetric measurements. To compare the results from the treatment planning systems (TPS) and from the Monte Carlo simulations, conversion factors are required. Indeed, in the TPS, patient tissues are converted to equivalent water depth, based on their WEPLs [Jäkel et al. 2001], and calculations of the physical and biological quantities are then performed in water. No conversion of the patient tissues into equivalent water depth takes place in the Monte Carlo algorithms.

The conversion factors currently used consider the water over material stopping power ratio (STPR) and fluence correction factors. The ratio of dose to water at a certain water equivalent depth, $D_w(z_{w-eq})$, and dose to a material at a certain depth, $D_m(z_m)$, is given by [Lühr et al. 2011]:

$$\frac{D_w(z_{w-eq})}{D_m(z_m)} = \frac{\sum_i \int_0^{E_{max,i}} \phi_{w,i}(E, z_{w-eq}) \left(\frac{S_{col,i}(E)}{\rho}\right)_w dE}{\sum_i \int_0^{E_{max,i}} \phi_{m,i}(E, z_m) \left(\frac{S_{col,i}(E)}{\rho}\right)_m dE} \tag{3.17}$$

where $\phi_{w,i}$ and $\phi_{m,i}$ are the charged particle fluence for any particle type i in the beam, respectively in water and in the material, $S_{col,i}$ is the collision stopping power for the particle i, ρ is the density of the material and E is the particle energy.

As the whole spectrum of particle species (primary and secondary) has to be considered, calculation of the correction factors becomes more complex for heavier primary ions and a deep knowledge of the physical processes occurring along the beam path is necessary.

In this thesis the nuclear interactions were investigated and compared in water and non-water materials (PMMA and tissue surrogates), for carbon and helium ion beams. The results achieved might contribute to improve the quality of the dosimetric measurements and the accuracy of the conversion factors.

However, it should be noted that the quantity dose to tissue might replace the dose to water in the future. Indeed, Monte Carlo simulations allow a more realistic representation of the patient tissues, and a more accurate description of the nuclear interactions and of the lateral spread of the beam particles [Battistoni et al. 2016]. Therefore, treatment planning systems fully based on Monte Carlo methods might replace the analytical TPS in the next future. The only issue which need to be solved prior the implementation of Monte Carlo treatment planning systems in the clinical routine regards the still too high calculation times.

3.2 Biological basis of ion radiotherapy

To achieve high precision in radiotherapy treatments, not only the physical but also the biological aspects of the interaction between the particle beams and the patient tissues need to be known and considered. Ionizing radiation can damage the deoxyribonucleic acid (DNA), the ribonucleic acid (RNA) and protein molecules. However, lower dose is required to damage the DNA and to cause cell cycle arrest or apoptosis. The damage can be directly induced by the radiation or indirectly induced by free radicals that travel far enough to reach and damage the DNA. Free radicals are atoms or molecules with unpair electrons in their outer shells. In case of interactions between the charged particles and human body, the most important free radical is the OH•, arising from the water molecules (about 80% of the cell is water) [Bentzen et al. 2008].

Some of the advantages offered by helium and carbon ions with respect to photons are the higher probabilities to produce direct and clustered damage in the DNA. A single-strand break in the DNA molecule is usually not sufficient to cause cell apoptosis, as this damage can be repaired easily using the opposite strand as a template. The basis in the DNA helix are indeed complementary in pairs: adenine-thymine, guanine-cytosine. Double-strand breaks, i.e. two strands opposite one another or close enough, are more difficult to repair or are misrepaired.

In this chapter the main radiobiology characteristics of helium and carbon ion beams are presented.

3.2.1 Linear energy transfer and relative biological effectiveness

The linear energy transfer (LET) is widely used to quantify radiation quality. It is defined as the kinetic energy, dE, transferred by a charged particle to secondary electrons in a path length dx of a given medium:

$$LET = \frac{dE}{dx} \tag{3.18}$$

In this definition, all possible energy transfers are included. For high energetic charged particles heavier than electrons, the (unrestricted) LET and the stopping power (defined in Section 3.1.1) are nearly the same. Alternatively, a restricted LET can also be defined, which takes into account only secondary electrons with energy below a given threshold. The difference between restricted LET and stopping power arises as the transferred energy can be deposited also far away from the primary particle track, mainly via secondary electrons and in smaller amount also via Cerenkov radiation and bremsstrahlung photons. The restricted LET provides information on the ionization density on a microscopic level, and it is therefore correlated to the particle physical properties. The stopping power indeed depends both on the projectile and material characteristics.

The radial dose distribution of ion tracks can be described by two main processes: (i) due to Coulomb interactions between the projectile and target atoms, δ electrons are produced; (ii) these secondary electrons travel within the medium and may undergo elastic and inelastic collisions. As an example, the tracks of protons and carbon ions are compared in Figure 3.3: it can be seen that the dose distribution is more localized for heavier particles. Consequently, multiple strand breaks and base damages are more probable. Since clustered DNA damage is more difficult to repair, the biological effectiveness of helium and carbon ions is higher than for protons and photons [Amaldi and Kraft 2005 and Ma and Lomax 2012]. Therefore, higher-LET-radiation is more efficient against radioresistant tumors containing many hypoxic cells: the oxygen concentration is relevant in case of photon beams, where the DNA damage is caused by the free radicals (like OH•), whereas it plays a minor role in case of helium and especially carbon ion beams, as the damage to the DNA helix is caused directly by the charged particles. Moreover, the high LET contribution to the dose increases faster in the Bragg peak than in the plateau region with increasing particle charge. Therefore, in general, high LET radiation allows to better spare the organs at risk, which are usually located in the plateau region or behind the Bragg peak.

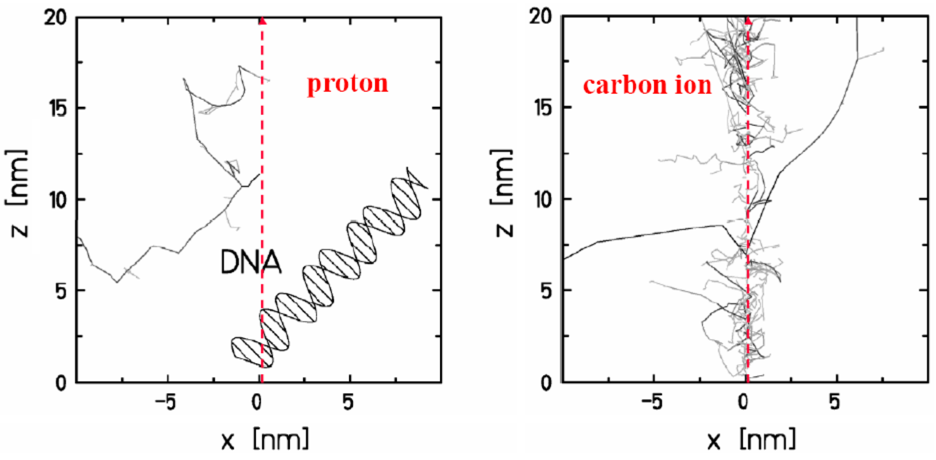

Figure 3.3: Proton and carbon ion tracks at a microscopic level. Due to the high density of the secondary electrons produced, the energy deposited by carbon ions is highly localized along the particle tracks. Reprinted from Amaldi and Kraft 2005.

However, despite the wide use made of the LET to compare different radiation types and their characteristics, the dependency of the LET on the projectile particle charge, energy and track introduces some limitations on its use, especially in case of fixed particle beams and when the fragmentation processes are not negligible. Another quantity, the relative biological effectiveness (RBE), was then introduced to take into account the different pattern of energy depositions. The RBE is the ratio between the dose of a reference radiation, D_{ref}, (e.g. x-rays or ^{60}Co gamma rays) and the dose of any radiation, D_{rad}, which produces the same biological effect in tissue:

$$RBE = \left.\frac{D_{ref}}{D_{rad}}\right|_{iso-effect} \tag{3.19}$$

The RBE depends on the radiation type, particle energy, delivered dose, level of oxygenation, target tissue, clinical endpoint and fractionation. Figure 3.4 shows the dependency of the RBE on the LET for various particle species. The RBE initially increases with the LET and a maximum is reached when the delivered dose is the one required to cause the cell death. For higher LET values the RBE decreases as the greater delivered dose do not cause additional damage in the cells ("overkill" region).
However, as the ionization tracks depend on the particle energy, an accurate prediction of the RBE from the LET is not possible. Models to estimate the RBE in the clinical radiotherapy practice are presented in the next section.

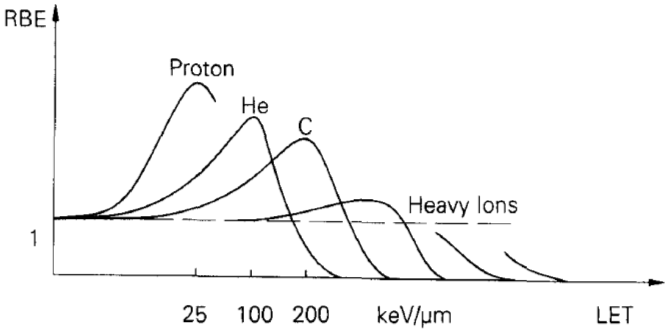

Figure 3.4: RBE as a function of the LET, for a 25 keV/μm proton beam, a 100 keV/μm helium ion beam and a 200 keV/μm carbon ion beam. The maximum of the RBE shifts to higher LET with increasing the particle charge. Reprinted from Kraft 1999.

3.2.2 Biological models

The sensitivity of the cells to radiation is measured via the cell survival-dose curve, which indicates the percentage of surviving cells as a function of the delivered radiation dose. A schematic example is shown in Figure 3.5, where the survival-dose curves are compared for a photon and a charged particle beam. At low doses, most of the damages can be repaired, and the sensitivity of the cells to radiation is low. With increasing dose the survival curve bends downwards. Moreover, the curve becomes more linear with increasing LET.
However, the biological and physical background of the interactions between tracks are still controversial [Joiner and Kogel 2009]. Different models have been proposed to predict the shape of the cell survival curves. The most commonly used is the so called

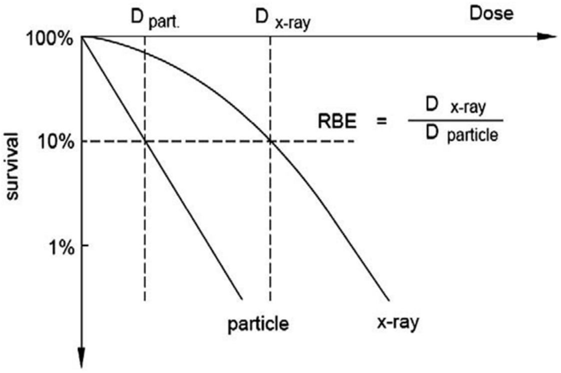

Figure 3.5: Schematic illustration of the survival-dose curves of cells irradiated with x-rays and with heavy particle ions (e.g. carbon ions). The curve becomes more linear with increasing LET.

linear quadratic (LQ) model, which describes the cell survival-dose curve by means of a second order polynomial equation:

$$-ln(S) = \alpha D + \beta D^2 \tag{3.20}$$

where S is the surviving fraction, D is the dose, and α and β are two parameters derived experimentally. α and β are tissue specific and determine the shape of the survival curve. Indeed, according to the most conclusive interpretation of the LQ model, the αD parameter arises from single-track events, and gives the shape of the survival-dose curve at low doses; the βD^2 parameter is related to two-track events, and influences the curve at high doses [Garciá-Ramos et al. 2015]. The more linear shape of the survival curve with increasing LET indicates that double hits become less important to cause cell deaths for higher LET-radiation. That is probably due to the greater probability to cause double strand breaks in the DNA with a single particle [Jäkel 2008].
In the clinically relevant dose range (<5-6 Gy) the LQ model is able to predict and to explain rather well cell survival curves, changes of the biological effectiveness with the LET and the dose-rate effect observed experimentally [Joiner and Kogel 2009]. Other proposed models divide the effects of ionizing radiation into non-repairable lesions (equivalent to the linear term of the LQ model) and into repairable lesions (equivalent to the quadratic term). However, these models give rise to cell survival curves which are rather similar.

The LQ model was implemented in the local effect model (LEM) developed at GSI and currently used in most of the treatment planning systems in Europe (including the SynGo PT treatment planning system used at HIT). LEM takes into account the track structure to define the RBE of high-LET radiation. Indeed, for carbon and helium ions, unlike for photons and protons, a unique definition of the RBE along the particle path is not recommended [Ma and Lomax 2012]. The RBE in the Bragg peak is about three times higher than in the initial plateau region, for carbon ions, and it is about 1.5 times higher for helium ions. In the LEM model the RBE is defined at any position in the irradiation field. The dose level, biological endpoint, target tissue and composition of the radiation field are considered to optimize the biological (i.e. RBE-weighted) dose distributions.

A deep knowledge of the beam contamination, energy spectra and lateral particle distributions is required, not to spoil the validity of the predictions of the treatment planning systems [Garciá-Ramos et al. 2015]. In this thesis the physical processes occurring in carbon and helium ion beams were investigated. These studies can contribute to improve the physical beam models and their accuracies.

3.3 Previous studies on ion nuclear fragmentation

As discussed in Section 3.1.4, due to nuclear interactions between projectile ions and medium atoms, secondary fragments may be produced. These secondary particles, which have lower masses and charges but approximately same velocity like the primary ions, cause the fragmentation tail visible in Figure 3.1. Fluence, energy, LET and lateral distribution of the primary and secondary particles need to be well known in radiotherapy for an accurate estimation of the delivered dose distributions.

3.3.1 Carbon ion beams

Clinical treatments with carbon ions started at NIRS/HIMAC (Japan) in 1994 and at GSI (Germany) in 1997. Several studies were carried out in those centers, before and after the beginning of the radiotherapy treatments, to deepen the knowledge on carbon ion fragmentation. In the following the most relevant works of interest for this thesis are presented.

Standard works at GSI
A schematic illustration of the experimental setup used at GSI to investigate ion nuclear interactions is shown in Figure 3.6. The position of the particles are obtained via multiwire chambers and a ionisation chamber. Identification of the different particle species is performed combining energy loss measurememts in the ionization chamber and time-of-flight measurements in a plastic scintillator detector. In order to reach high resolution in the time-of-flight measurements, the detectors need to be placed some meter far from the target. Due to its characteristic, this experimental setup can provide useful and accurate information on the fragment spectra and angular distributions, but it would rather difficult to implement in clinical facilities.

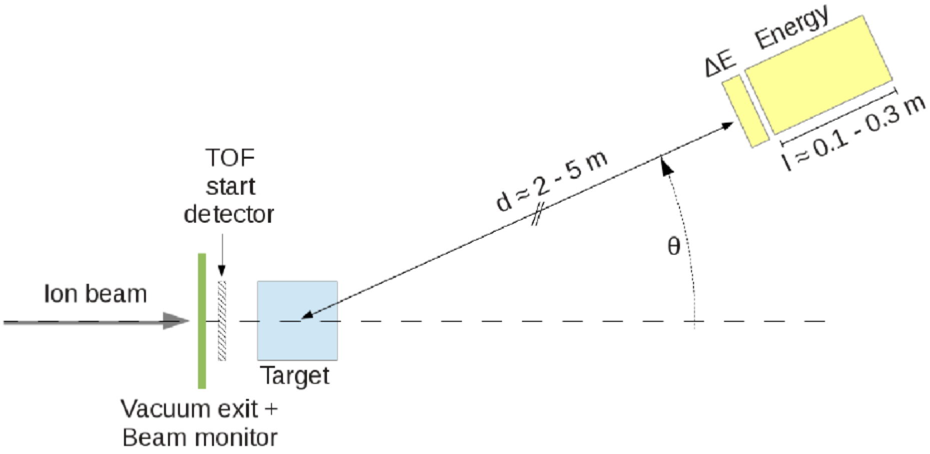

Figure 3.6: Schematic illustration of a measurement setup used at GSI to investigate ion nuclear fragmentation. Reprinted from Hartmann 2013.

In the initial measurements performed in the 1990s [Schardt et al. 1995, Schall et al. 1996] the detectors were centered in the beam axis (i.e. θ=0). Ion beams in the range from ^{10}B to ^{20}Ne, and therefore including ^{12}C, were investigated. Beam energies between 200 MeV/u and 670 MeV/u and thick targets made of water, lucite, polyethylene and aluminum were used. The results on the beam attenuation and on the build-up of the secondary fragments enabled a better understanding of the shape of the depth-dose curves. Mean free path lengths, partial and total charge-changing cross section were also calculated. The latter one was found to be very low in case of carbon ions, among the particle species investigated. This finding contributed to increase the interest on carbon ions for radiotherapy applications.
In Gunzert-Marx et al. 2008 yields and dose contribution of the secondary fragments were estimated for a 200 MeV/u carbon ion beam stopping in water. Both experiments and simulations with the PHITS code were performed. Figure 3.7 shows the calculated contributions of the secondary particles to the dose, in front and behind the Bragg peak. It was found that, shortly behind the Bragg peak, the major contribution arises from boron fragments. At larger depths only H and He contribute, as the heavier fragments have shorter ranges than the lighter ones. The detectors were also rotated up to 30° from the beam axis (as shown in Figure 3.6) and the particle energy spectra were investigated. Good agreement was found between the experiments and Monte Carlo simulations for protons and deuterons, while significant differences in the energy spectra were observed for triton and helium at small angles ($\leqslant$10°).
In Haettner 2006 carbon ion attenuation in water was analysed for two energies, 200 MeV/u and 400 MeV/u. The build-ups of secondary fragments were investigated at different depths along the Bragg curve, and the lateral particle distributions were analysed at different angles from the beam axis, up to 10°.

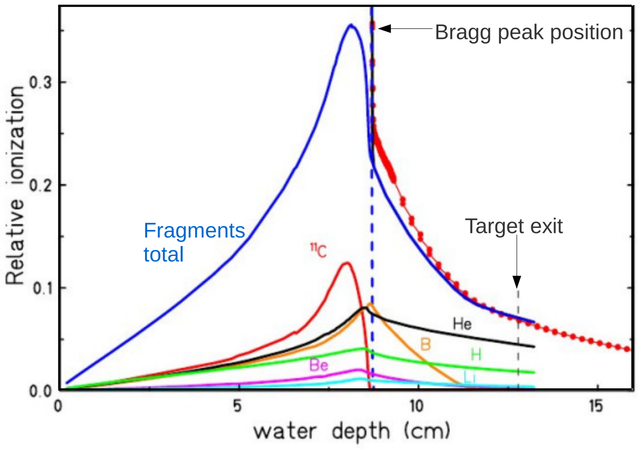

Figure 3.7: Simulated contribution to the dose from the fragments produced in a 200 MeV/u carbon ion beam in water. Position of the Bragg peak and thickness of the targets are indicated by arrows. The heavier fragments mainly contribute to the dose shortly behind the Bragg peak. Only the lighter fragments can be found at greater depths. Reproduced from Gunzert-Marx et al. 2008.

The experimental data from Haettner 2006 have been used in several studies as reference. For instance, in Böhlen et al. 2010 they have been compared with the results obtained from FLUKA and from GEANT4. As an example, Figure 3.8 shows the build-up of secondary fragments obtained from the experiments of Haettner et al. 2013 and from the simulations. It can be seen that the number of H and He were lower in both simulation codes. GEANT4 overestimated the amount of Li, Be and B detected, while FLUKA better reproduced the experimental data for those particle species. Regarding the measurements at larger angles to the beam axis, FLUKA slightly underestimated the particle yields, especially for H and Li. Instead, GEANT4 underestimated the fragmentation yields at small angles and overestimated them at large angles.

To improve the beam and the nuclear interaction models, experimental data on the fragmentation cross sections are needed. The lack of data in the whole range of beam energies and in different experimental configurations, which can be of interest for clinical applications, is currently an issue.

Research works at NIRS/HIMAC

Due to the limitation in the size of the therapy room, which did not enable time-of-flight measurements, a slightly different experimental setup was employed at NIRS/HIMAC. In the works of Matsufuji [Matsufuji et al. 2003, Matsufuji et al. 2011]] a counter telescope, composed of a 1 mm NE102A plastic scintillator (to count the number of incoming particles), of a gas-flow proportional counter (for LET measurements) and of a BGO scintillator (for ΔE-E measurements), was used. Information from the BGO scintillator enabled to differentiate between particle species. This setup was used to investigate the

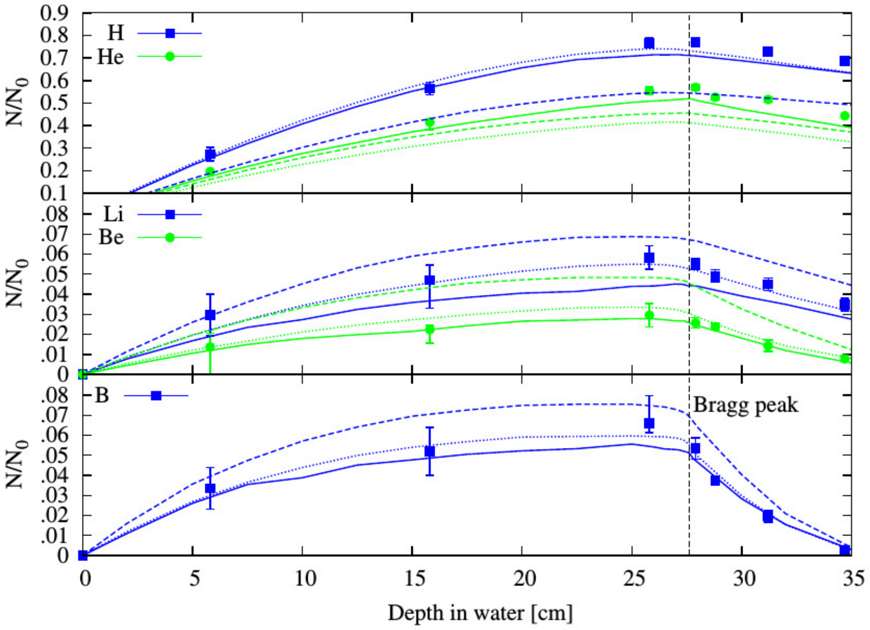

Figure 3.8: Build-up of secondary fragments produced in a 400 MeV/u carbon ion beam in water. The experimental data from Haettner et al. 2013 are shown as full points. Simulations with FLUKA are shown as solid line. The dashed and the dotted lines indicate the calculations performed with GEANT4 using the BIC LI and the G4QMD model, respectively. The results are normalized to the number of incoming primary ions. Reprinted from Böhlen et al. 2010.

fragmentation of a 290 MeV/u carbon ion beam in PMMA targets of various thicknesses (between 0 cmWET and 13 cmWET). PMMA was used as a substitute of water. The trajectories of the projectile fragments were found to be rather parallel to the initial projectile particle trajectories. The secondary particles produced, LET spectra and spatial fragment distributions were also analysed. The contribution of each fragment species to the total dose were investigated and found to be less relevant with decreasing particle mass and charge. However, even if the fragment contribution remains minor with respect to the dose delivered by the primary particles, it increases in thicker targets and should be considered in the treatment planning.

The new approach proposed in this thesis

All the studies described in this section suggest that additional data are required to further improve the nuclear reaction models, and to estimate the beam contamination and its clinical effects more accurately. In the present thesis the Timepix detectors were used, which allow a smaller and more versatile experimental setup than those previously used. Further experimental data and knowledge on the nuclear interaction processes of therapeutic ion beams in different materials can be gained with the new investigation method developed here.

3.3.2 Helium ion beams

Pioneering treatments with helium ion beams started in 1977 at the Berkeley National Laboratory (USA), where about 858 patients were treated. Results and benefits achieved with helium ion radiotherapy were well summarized in Castro et al. 1996. Although treatments with helium ions stopped in 1992, a great interest on these particles is growing again in the last years. However, many changes have occurred in the delivery systems and fractionation schema with respect to the initial techniques employed at LBNL. Therefore, a new method to calculate the dose in the treatment planning systems is necessary for the future radiotherapy with helium ions.
In Krämer et al. 2016 beam attenuation and build-up of secondary charged particles were investigated for a 200 MeV/u helium ion beam in water. TRiP98, the TPS developed in the pilot project with carbon ion at GSI, was used for the calculations. LEM in version IV, which has been optimized for low LET radiation, was implemented in the TPS. The results were then compared with experimental data acquired at the HIT facility. Figure 3.9 shows that the residual number of primary particles obtained in the experiments and in the calculations were in good agreement within the uncertainties. However, a higher amount of secondary H, and especially of protons, was found in the calculations. Deviations between calculated and measured absorbed dose were also observed, especially at the distal edge. These deviations need to be reduced as much as possible to improve the accuracy of the TPS predictions.

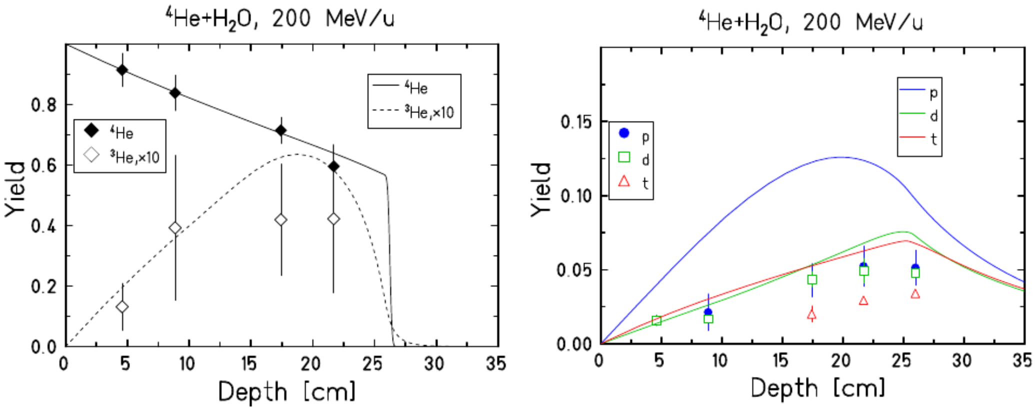

Figure 3.9: Attenuation of He ions (*left*) and build-up of secondary H (*right*) of a 200 MeV/u helium ion beam in water. Symbols represent the experimental dara; lines are the calculations with the TPS. Reprinted from Krämer et al. 2016.

Helium ions are promising candidates for clinical applications in radiotherapy. However, more experimental data are required to verify both their physical and their biological properties. The present thesis aims to provide some of the missing data: nuclear interactions of a 220 MeV/u helium ion beam were investigated and compared in water and in PMMA targets with the same water equivalent thickness between 5 cm$_{\text{WET}}$ and 18 cm$_{\text{WET}}$.

4 Material

4.1 Accelerator and beam delivery systems

Despite the higher construction, maintenance and operating costs in comparison to conventional radiotherapy, the number of proton and ion beam therapy facilities is increasing worldwide. Currently, 52 proton therapy centers and 5 carbon ion therapy centers are in operation, and other 5 centers offer both protons and carbon ion treatments [PTCOG-website 2016]. One of these is the HIT facility in Heidelberg (Section 4.1.2).

4.1.1 Overview

Cyclotrons, synchrotrons or synchrocyclotrons can be used to accelerate protons up to 220 MeV; only synchrotrons are used to accelerate carbon ions up to 430 MeV/u. These energies correspond to a penetration depth in tissue of approximately 30 cm, which enables to meet about 95% of the desired treatment plans [Linz 2012].
Cyclotrons have a fixed extraction energy and therefore degrading materials need to be added along the beam line. On the contrary, synchrotrons allow to directly change the energy and to track the extraction field by means of transport line magnets. As multiple scattering, range straggling and nuclear reactions along the beam transport line are reduced, higher beam quality and lower energy spread ($<0.1\%$) can be achieved with the synchrotrons [Ma and Lomax 2012, Linz 2012].
Besides the desired particle accelerator, another important choice which new centers have to make is the beam delivery method. Nowadays, the principal techniques are passive scattering and active scanning.
In the first approach (shown in Figure 4.1, left) a degrader (usually a rotating wheel with variable thickness or alternatively a static filter) is used to modulate the monoenergetic beam coming from the accelerator. Subsequently, a scatterer or a pair of wobbler magnets spread the beam laterally. A range shifter can be added to place the Bragg peak at the desired depth, and finally a patient specific collimator and a patient specific compensator are used to adjust the beam profile, both laterally and in depth. The main disadvantages of the passive beam shaping method are the nuclear interactions occurring in the extra materials along the beam line, and the lower accuracy and flexibility achievable in the depth dose profile [Schulz-Ertner, Jäkel, and Schlegel 2012].
Conversely, in the active beam shaping method (shown in Figure 4.1, right) no passive absorbers or patient specific devices are required. Magnetic dipoles are used to laterally

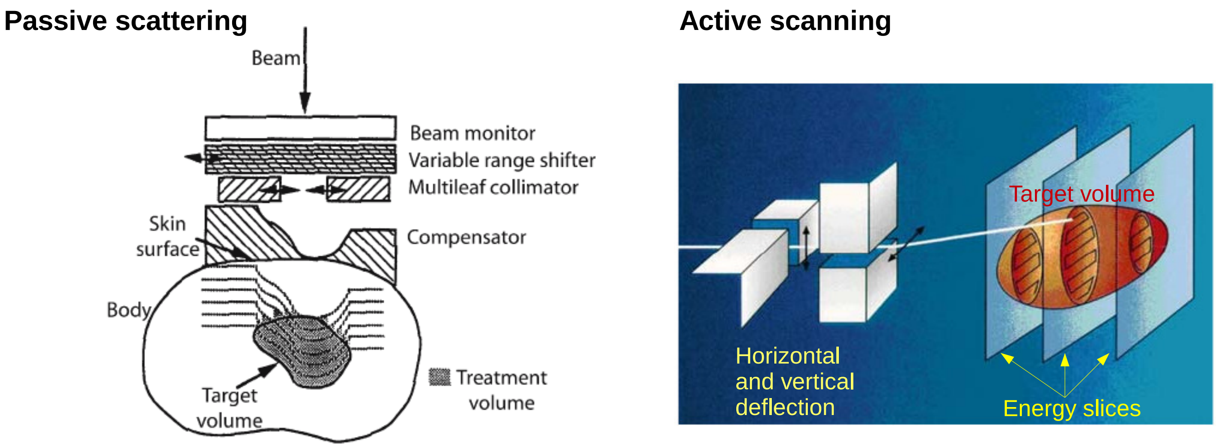
Passive scattering

Active scanning

Figure 4.1: Schematic representation of the passive scattering (*left*) and the active scanning (*right*) beam delivery systems. Reproduced from Schlegel, Bortfeld, and Grosu 2006.

deflect the beam and thus cover the whole target. To adjust the Bragg peak in depth, additional material can be placed before the patient, like at the Paul Scherrer Institute in Switzerland. A different approach is used at the Heidelberg Ion-Beam Therapy in Germany, where a synchroton is available: the beam energy is directly set at each pulse, and consequently no range shifter is required. The main advantage of the active scanning technique is the possibility to conform the dose both at the distal and at the proximal edge of the target. Moreover, as the beam parameters can be automatically set via a computer, patient specific components are not necessary.

Beam position, fluence and spot are monitored during the treatment delivery by means of detectors placed at the end of the beam line. For instance, the beam and application monitoring system (BAMS) implemented at HIT is composed of two multi-wire proportional chambers and three ionization chambers.

4.1.2 The HIT facility

The Heidelberg Ion-Beam Therapy (HIT) center (Figure 4.2) is a hospital-based particle therapy facility, in operation since 2009. More than 3500 patients have been treated since then, with protons and carbon ions. The synchrotron ring circumference is 65 m, and the injection energy is 7 MeV/u. Per each acceleration cycle, 10^9 carbon ions and 4×10^{10} protons are achieved. Two treatment rooms have horizontal beam lines, while a third room is equipped with a 360° rotating gantry, with a diameter of 13 m, a length of 25 m and a total weight of 600 tons [Haberer et al. 2004]. Currently, this is the only carbon ion gantry available for treatments; another one, at the HIMAC facility in Chiba, should start to operate by the end of 2016. In addition to the treatment rooms, a third horizontal beam line provides an extra quality assurance and experimental room. Here,

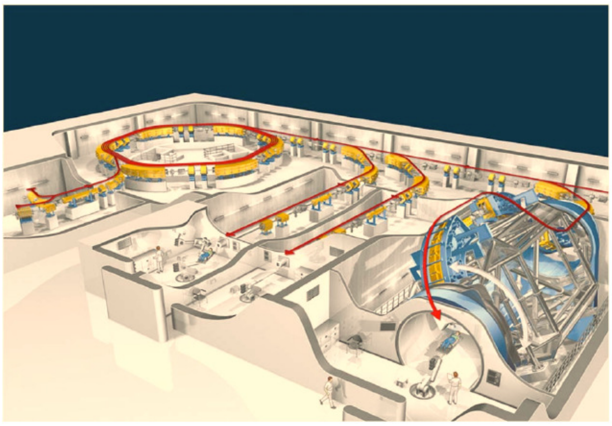

Figure 4.2: The HIT accelerator. Reprinted from Jäkel, Karger, and Debus 2008.

beside protons and carbon ions, also helium and oxygen ions can be used for preclinical studies and other research purposes.
The active raster scanning technique, developed at GSI in Darmstadt [Haberer et al. 1993], is employed at HIT. The tumor is divided in several slices by the treatment planning software and for each slice the required beam penetration depth is calculated. The beam is then moved laterally over each slice, so to deliver the desired dose in the target [Combs et al. 2010b]. Thanks to the 255 energy levels, 10 intensity values and 4 beam widths available, high accuracy in the tumor irradiation can be reached. The most relevant characteristics of the HIT facility are summarized in Table 4.1.
The treatment planning is based on MR- and CT-images, which are used for target and organ at risk contouring [Combs et al. 2010a]. The three dimensional treatment planning system, SynGo PT Planning (developed by Siemens Oncology Care System), is based on biological plan optimization for the calculation of the RBE. RBE equal to 1.1 is clinically used for protons, while for carbon ions the local effect model (LEM) is implemented. This model, developed at GSI, takes into account the tissue types and the endpoints for the calculation of the RBE (see Section 3.2.2 for more information about LEM). The Monte Carlo FLUKA code (described in Section 4.3) is exploited for research applications and to support treatment planning.

The clinical results achieved at the HIT center since 2009 have shown the benefits arising from the use of protons and carbon ions in place of photons, and of the beam scanning instead of the beam scattering technique. The lower integral delivered dose enables to reduce the long-term side effects, which are a main concern in general and for pediatric patients in particular [Combs et al. 2012]. The main clinical treatments at the HIT include tumors of the brain, skull, and head-and-neck regions, soft tissue sarcomas and osteosarcoma, prostate, and gastrointestinal cancers.
From 2017 treatments with helium ions are also planned. Helium ion beams have sharper penumbra than proton beams [Ströbele et al. 2006] and reduced fragmentation tail than carbon ion beams.

Table 4.1: Main characteristics and parameters of the HIT facility

Particle species	H, He, C, O
Type of accelerator	Synchrotron
Beam delivery technique	Intensity controlled rasterscan
Maximal energy	H: 221 MeV He: 221 MeV/u C: 430 MeV/u O: 515 MeV/u
Maximal beam intensity	H: 4×10^{10} He: 1×10^{10} C: 1×10^{9} O: 5×10^{8}
Beam width	4-15 mm FWHM
Treatment field	20×20 cm^2
Range resolution	Proximal : 1.0 mm Distal : 1.5 mm

4.2 The experimental equipment

4.2.1 The materials

The used equipment and materials are listed and described in the following. Details of the experimental setup and parameters can be found in Section 5.1.

- **Detecting equipment** (described in more detail in Section 4.2.3) :
  - 4 Timepix detectors, used for particle species identification and particle tracking.
  - Two FITPix devices to read-out the signal generated in the detectors.
  - Two motherboards to connect the detectors to the FITPix devices.

- **Targets**:
    - Water boxes[1] with 15×15 cm^2 faces and various thicknesses. They have 0.3 cm thick PMMA walls and were filled with purified water. Information on their geometrical thickness, WET, and WEPL are available in Table 6.1 and Table 6.2.
    - PMMA targets (chemical composition $C_5O_2H_8$), built by combining together PMMA slabs[2] with thicknesses between 0.1 cm and 5 cm. The measured densities of these targets are listed in Table 4.2, whilst geometrical thicknesses, WET, and WEPL values are available in Table 6.1.
    - Tissue equivalent slabs[2], manufactured by Gammex RMI, Middleton, WI. In this work lung (LN300, Model 455), adipose (AP6, Model453), inner bone (IB3, Model 456) and cortical bone (SB3, Model 450) surrogates were used. Each tissue equivalent target was built by 4 slabs, each 1 cm thick. Details on the main characteristics of the Gammex slabs are listed in Table 4.3.
- **PTW PEAKFINDER water column**: used to measure the WET of the targets. It is described in Section 4.2.2.

Table 4.2: Density of the PMMA targets

Target labeling	Density (g/cm^3)
PMMA 5 cm$_{\text{WET}}$	1.178 ± 0.012
PMMA 7 cm$_{\text{WET}}$	1.183 ± 0.011
PMMA 10 cm$_{\text{WET}}$	1.182 ± 0.011
PMMA 15 cm$_{\text{WET}}$	1.188 ± 0.009
PMMA 18 cm$_{\text{WET}}$	1.186 ± 0.010

---

[1] built in-house at the DKFZ workshop

[2] provided by Dr. S. Brons at HIT

Table 4.3: Density and elemental compositions of the Gammex slabs, provided by the manufacturer. Each target is 4 cm thick.

Target labeling	Density (g/cm^3)
Lung	0.29
Adipose	0.920
Inner Bone	1.133
Cortical Bone	1.819

	Composition								
Target labeling	H (%)	C (%)	N (%)	O (%)	Mg (%)	Si (%)	P (%)	Cl (%)	Ca (%)
Lung	8.46	59.38	1.96	18.14	11.19	0.78		0.10	
Adipose	9.06	72.30	2.25	16.27				0.13	
Inner Bone	6.67	55.64	1.96	23.52			3.23	0.11	8.86
Cortical Bone	3.41	31.41	1.84	36.50				0.04	26.81

4.2.2 The PEAKFINDER

The PEAKFINDER water column shown in Figure 4.3 (PTW PEAKFINDER^{TM}, Model T41030 Water Column, with servo control unit T41027 from PTW Freiburg) is widely used in radiotherapy to measure the Bragg curve of proton and heavy ion beams. It contains two Bragg peak chambers, one of which operates as a reference. Peak depths up to 35 cm$_{w-eq}$ can be measured, and the sampling step can be set down to 10 μm. In this thesis, it was used to measure the water equivalent thickness (WET) of the investigated phantoms. The PEAKFINDER was connected to a pulse generator, which in turn was connected to the trigger port of an electrometer. In such way, the PEAKFINDER received a trigger when the particle beam was “ON”.
Details of the experimental parameters used for the measurements are described in Section 5.2.1, while the results are reported in Section 6.1.1.

4.2.3 The Timepix detectors

The pixelated semiconductor detectors of the Timepix family (Figure 4.4, left) were initially developed for photon imaging [Llopart et al. 2007]. Due to their imaging properties, they have subsequently been implemented also in hadrontherapy, neutron radiography [Jakubek M. et al. 2013], dosimetry for space radiation applications [Pinsky et al. 2011, Turecek et al. 2011], and in the ATLAS detector at CERN LHC [Vykydal et al. 2009]. For ions they provide 100% detection efficiency, single particle detection and fast data acquisition in small and versatile setups [Granja et al. 2007].

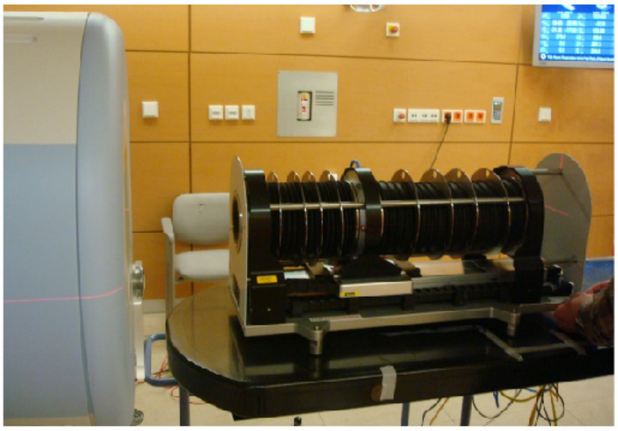

Figure 4.3: The PEAKFINDER T41030 Water Column from PTW was used to measure the WET of the targets. Reprinted from Sánchez Parcerisa 2012.

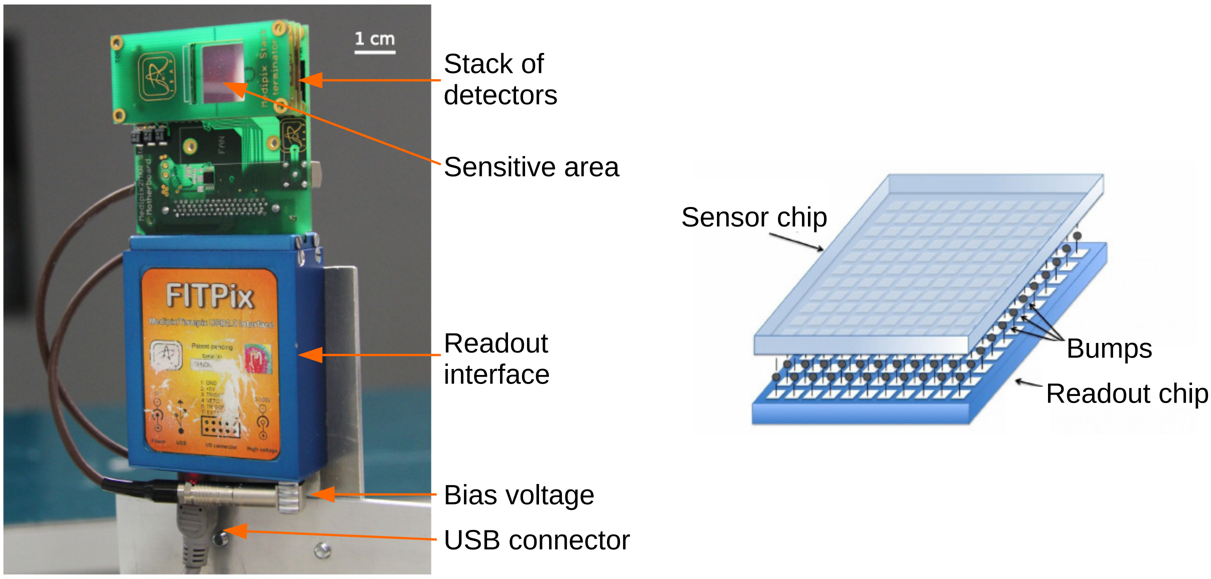

Figure 4.4: *Left:* A stack of three Timepix detectors. *Right:* Timepix chips: the sensitive and readout layers are connected using bump bonds. Reproduced from Gwosch 2012.

The Medipix chips (Figure 4.4, right) consist of a sensitive and a read-out layer, connected via a bump bonded technique. The more used materials for the chips are Si, GaAs and CdTe [Jakubek 2009b], while the bumps are made of 63/37 Sn-Pb, the most common alloy implemented for electrical soldering.
The sensitive and the read-out chips consist of a matrix of 256×256 pixels, with 55 μm pitch. For the chips made of silicon, the thickness can currently vary between 50 μm and 1000 μm. A thicker sensitive layer implies a higher energy deposited by the crossing particles in the detector, but also a higher scattering component. Therefore, depending on the experimental purposes, different thicknesses should be considered. If multiple layers are used for particle tracking, like in this thesis, the insensitive layer should then be as thin as possible, since it affects the particle energies and trajectories.
The detectors used in this work have sensitive and insensitive chips made of silicon, and thickness of 300 μm and 100 μm, respectively.

Particle signal generation

Each pixel is connected to a preamplifier, a discriminator and a counter implemented on the read-out chip. As each pixel has its own electronics, it can operate independently. The measured signal has the characteristic shape of the preamplifier analog output response (Figure 4.5, left). The slopes of the rising and falling edges are determined by the setting parameters [Llopart et al. 2007]. The generated signal is compared to a threshold value, set specifically for each pixel, and collected only when it is above the pre-set level. Threshold values equal to several eV are a good compromise between reduction of the background noise and cut on the particle signals.
Each ion crossing the sensor creates a column of charges (electron-hole pairs), which are then collected driven by the electric field applied in the sensor chip (Figure 4.5, right).

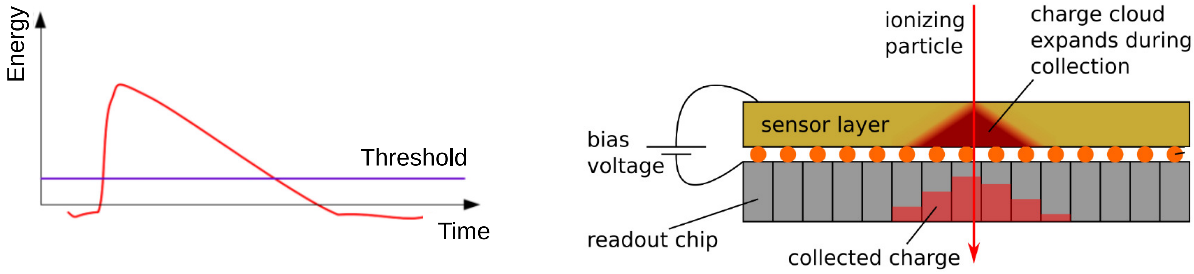

Figure 4.5: *Left:* Schematic representation of the preamplifier analog output response of the Timepix detectors. *Right:* The charge created by a ionizing particle is driven by an externally applied electric field. During collection, the charge expands forming a so called cluster. Reprinted from Jakubek 2009b.

In case of heavy charged particles, the energy deposition and the resulting number of electron-hole pairs can be high enough to distort the local electric field. Consequently, in addition to the diffusion and drift processes, the plasma effect, the charge column erosion and the funneling affect the collection of the particle charges [Bouchami et al. 2009, Campbell et al. 2008]. The plasma effect consists in the lateral diffusion of the ionized column, due to the lower density of carries in the rest of the sensor. The carriers at the edge of the column might escape and be influenced by the longitudinal electric field. As a result, the number of carriers in the plasma decreases. The carriers which do not undergo recombination are funneled to the collecting electrodes. The funneling effect is stronger for low electric fields, as it enables to collect charges that otherwise would have been in the non-depleted area [Campbell et al. 2008]. The main consequence of all those processes is a lateral spread of the charge due to Coulomb repulsion: the signal is collected in multiple adjacent pixels, forming a so called cluster (examples are shown in Figure 5.3). The number of involved pixels, named cluster size, and the cluster shape depend in general on the bias voltage applied to the sensor chip and on the particle type, energy, and impinging angle [Granja et al. 2007].

Cluster size and shape

With the used detectors, bias voltages between 5 V and 100 V can be set. The effect of different bias voltages on the cluster size is shown in Figure 4.6, for different particle species (protons, α-particles, carbon ions, and oxygen ions).

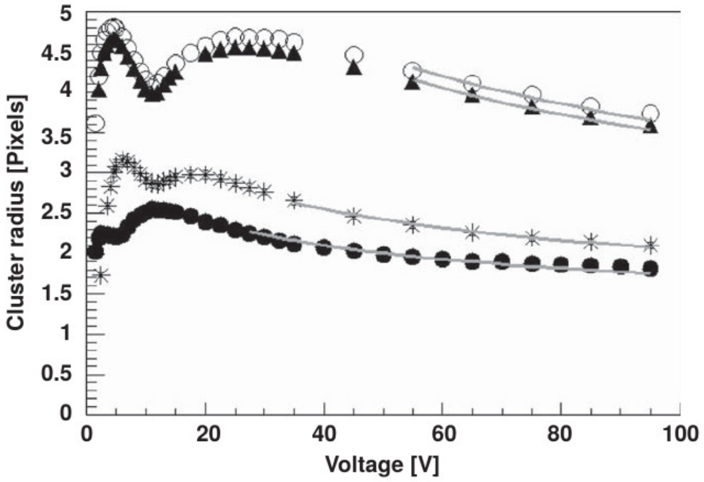

Figure 4.6: Dependence of the cluster radius (and consequently size) on the externally applied bias voltage, for protons (●), α-particles ($*$), carbon ions (▲), and oxygen ions (○). The lines are the model fits considering plasma effect, charge column erosion, funneling, diffusion and drift processes. Reprinted from Bouchami et al. 2009.

The initial increase is due to diffusion processes on the long term; the main contribution to the following decrease arises from to funneling effect (the charge density inside the column decreases and therefore also the lateral spread); increasing the voltage values, the charge lateral diffusion is reduced; the second peak occurs when the depleted area equals the particle tracks; finally, the whole particle tracks are included in the sensitive layer and the cluster size decreases, due to the increasing strength of the electric field [Campbell et al. 2008].

The response of the detector depends on the radiation type, as described here.
Heavy charged particles hitting the detector perpendicularly produce high ionization and energy deposition: the charge expands laterally due to diffusion and Coulomb repulsion. Consequently, the clusters created by these particles are usually rather round shaped and cover tens of pixels. However, if the trajectory gets more parallel to the detector, the cluster shape becomes more elongated. Moreover, the cluster size depends directly on the particle charge and indirectly on the particle energy.
Light particles, such as electrons and positrons, generally create straight or curly tracks, as they are diffused within the sensitive layer. The peculiar shape of the resulting clusters makes the identification of these particles in the detector very easy.
The signal from X-rays or low energetic particles is usually collected only in 1 or 2 pixels [Bouchami et al. 2010, Holy et al. 2008].
Therefore, pattern recognition of the generated clusters allows to differentiate between particle species in a mixed beam. This method was developed and exploited in Hartmann 2013 for ion spectroscopy studies with carbon ion beams. In this thesis the method has been enhanced and used to investigate carbon and helium fragmentation processes.

Detector operation modes
Three operation modes, illustrated in Figure 4.7, were used in this work:

1. The Medipix mode counts the number of incoming particles reaching the detector within a given frame, i.e. the pixel counter is incremented by a unit for each event above the predefined threshold. This mode was used to check the alignment of the detectors (see Section 5.2.2).

2. The Time mode provides information on the particle arrival time in the detector. The counting starts when the signal is above the threshold and runs till the end of the frame. The highest pixel value within a cluster is therefore an inverse measure of the particle arrival time (higher values correspond to particles arrived earlier). In this work three detectors were set in Timepix mode and their counting clocks were synchronized, so to enable time coincidence measurements and particle tracking (as described in Section 5.1).

3. In the Time over Threshold (ToT) mode the counter is incremented while the signal is above the preset threshold. Since the amplitude of the signal is proportional to the collected charge, the sum of the pixel values within a cluster (cluster signal) is related to the deposited particle energy. However the response of the pixels varies over the

detector area. Therefore an appropriate energy calibration needs to be performed to correctly calculate the deposited particle energy [Jakubek 2009a]. Moreover, the calculated sum may be lower than the theoretical value, e.g. because of the charge lost as it is below the threshold level or because of quenching in the detector. In this work one detector was set in ToT mode and used to distinguish between particle species (as described in Section 5.1 and Section 5.4.2).

Besides the three standard operation modes, a so called masking mode can be used, which sets the pixel to "off". It was applied to damaged or malfunctioning pixels.

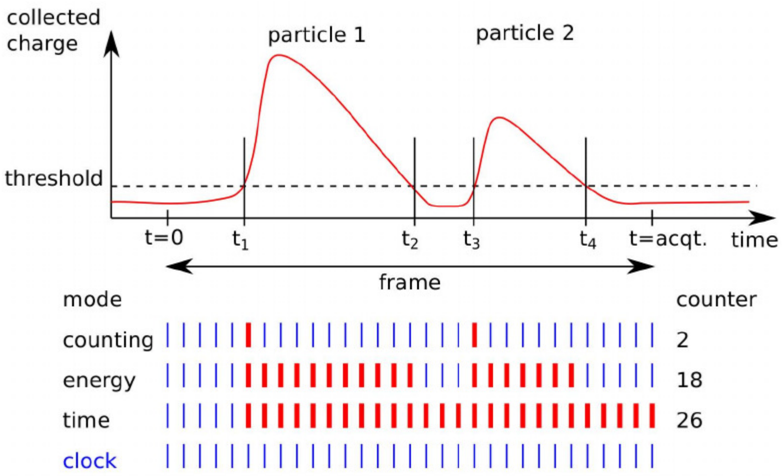

Figure 4.7: Representation of the detector operation modes used in this work: Medipix mode (or counting mode), Time mode (or time mode), ToT mode (or energy mode). Reprinted from Gwosch et al. 2013.

Energy calibration of the detector response

The energy calibration is specific to each detector and each single pixel. It was performed by the research group at the IEAP in Prague, and currently done by the Advacam s.r.o. company in Prague. Checks and adjustments of the calibration curves are performed approximately every year for each detector. The procedure is described in the following. Two well known γ-emitters (^{55}Fe: 5.9 KeV, and ^{241}Am: 59.5 KeV) and 6 fluorescent materials emitting X-rays ($_{26}$Fe: 6.4 KeV, $_{29}$Cu: 8.0 KeV, $_{40}$Zr: 15.8 KeV, $_{42}$Mo: 17.5 KeV, $_{48}$Cd: 23.2 KeV, $_{49}$In: 24.2 KeV) are used. Only events producing single pixel clusters are taken into account and the experimental calibration curve is parametrized as [Jakubek 2010]:

$$f(E) = aE + b - \frac{c}{E-t} \tag{4.1}$$

where the 4 parameters a, b, c, d are determined by least-squares fit, for each pixel.

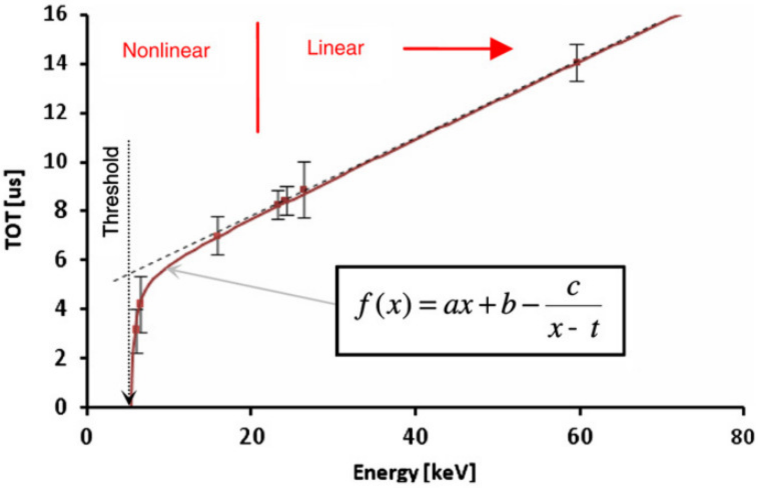

Figure 4.8: Example of a single-pixel energy calibration curve of the Timepix detectors. Reprinted from Jakubek 2010.

The curve is not linear at low energies, as shown in Figure 4.8; however, the linear behavior at high values allows to extrapolate the calibration values up to 900 KeV. For higher pixel values the measured signal starts to be distorted [Jakubek 2010].
Dedicated studies have been performed and are ongoing within the research group, to better understand the detector response to heavy ions and to improve the calibration curves.

Data acquisition software

The detectors were connected to a laptop just by means of a standard USB. The software Pixelman, used to operate the detectors, was originally developed by the Czech technical university in Prague. Recently, a new package, Pixetpro, has been provided for the same purposes and applications by the Advacam s.r.o. company.
The desired bias voltage, threshold, clock frequency and operation mode can be easily set. The parameters used in this work are discussed in Section 5.1. Simple data visualization and processing are possible on-line. For instance, the current frame images, distributions of cluster size, cluster signal and pixel values can be displayed during the data acquisition. The output data are saved in frame-based text files containing information on the frame number, acquisition time, x and y coordinates of the pixels forming a cluster and their pixel values. In the post-processing stage, these files were read and processed by self-written C++ and MATLAB routines.

4.3 The FLUKA Monte Carlo code

In the present work the experimental data and results were compared with those obtained with the FLUKA Monte Carlo code ([Ferrari et al. 2005, Battistoni et al. 2007]). This code was chosen as it is used at the HIT center for clinical and research purposes. General information on FLUKA is provided in the following, while settings and parameters used in this work are described in Section 5.3.2.

The FLUKA code can simulate about 60 different particle species plus heavy ions, with energies from 1 keV to 20 TeV. A friendly graphical interface, flair, was developed to support the FLUKA's users. Flair is based on Python and Tkinter, and enables to edit, to compile, to debug and to run the input files. In combination with flair, GeoViewer allows to visualize the geometry and easily check for errors.
In order to run a FLUKA simulation, the following definitions have to be specified:

A) Physics settings
Several separate packages (default or more specific) can be implemented for the physics models, depending on the required needs. Only the most relevant information regarding particle therapy applications are provided here.
The Bethe-Bloch theory is implemented to calculate the energy loss due to electromagnetic interactions. It takes into account the Barkas Z^3 and Bloch Z^4 effects to the first Born approximation. The electron-ion Mott cross section is also considered and used to correct the average stopping power, secondary electron production cross section and energy loss fluctuation [Battistoni et al. 2016]. The multiple Coulomb scattering formalism is based on the Molière theory.
Inelastic hadron-nucleus interactions in the therapeutic energy range are described in FLUKA by the PEANUT model (valid for interactions with momentum <5 GeV/c; above that value the Glauber-Gribov multiple scattering is considered). PEANUT includes a generalized intranuclear cascade (GINC) followed by a pre-equilibrium stage, with standard assumptions on exciton number or excitation energy, and by an equilibrium phase. In the thermally equilibrated system of the produced nuclei, evaporation of nucleons, fragments or γ-rays, or even fission processes can take place. The evaporation-fission stage of light residual nuclei (A<16) is modeled by Fermi break-up.
Heavy ion reactions are treated in FLUKA via the Boltzmann master equation (BME) (for energies below 150 MeV/u) or via the modified relativistic quantum molecular dynamics (RQMD) (for energies between 0.1 GeV/u and 5 GeV/u). In the latest version of the RQMD, a pre-equilibrium stage for the residual fragments is also included. Both the BME and the RQMD are interfaced with the PEANUT module, and FLUKA automatically switch between the two depending on the particle energies.
In the final step, FLUKA also consider de-excitation of the remaining equilibrated nucleus via evaporation, fission and fragmentation.

B) Transport thresholds
By default, high energy hadrons and muons are always generated in the FLUKA simulations and transported. However only the ionization energy loss is taken into account by default. To simulate also the nuclear interactions, the command IONTRANS can be used. Furthermore, the command THRESHOLD enables to set a lower energy limit for hadron elastic scattering and inelastic reactions.

C) Radiation source
In simple cases, FLUKA input cards as BEAM and BEAMPOS can be used to define the radiation source and its features (particle type and energy, source position, size and shape). For heavy ion sources the general name HEAVYION has to be used, and further characteristics can be specified via the card HI-PROPErt.
To handle with more complex experimental apparatuses, as the beam line at HIT, a user routine, SOURCE, can be used. It allows to specify source parameters and characteristics, like the distribution in energy, space and angle of the incoming particles, in more detail.

D) Geometry
The combinatorial geometry used by FLUKA is based on two concepts: bodies and regions. Planes, cylinders, spheres, cones and parallelepipeds are available as bodies, and their size can be set by the users. Regions are combinations (unions, subtractions or intersections) of bodies. The main reason to define regions is to normalize the scored quantities per cm^3.

E) Materials
For each region, a material has to be specified. A black hole around the whole geometry is required to discard the particles as soon as they reach the outer boundaries. For the other regions, any material available in the FLUKA list can be used. Tissue compositions are based on the ICRU and ICRP reference data. Alternatively, the cards MATERIAL, MAT-PROP and COMPOUND enable to define new materials by specifying their chemical and physical properties (e.g. atomic number, atomic weight, density and ionization potential).

F) Scoring
The final score is performed by detectors, or estimators, which are the equivalent of experimental instruments. The detector features and scoring quantities are defined by the user. Energy deposition, particle fluence, track length, double differential yield in a surface are some of the available pre-defined estimators.

The results can be displayed in colour plots (using Gnuplot), or saved in binary files or in ASCII files. The latter ones were used in this work and further post-processed.

5 Method

In the present thesis three main studies were carried out, in which interaction of

1) carbon ion beams in water and in PMMA targets with the same WET
2) helium ion beams in water and in PMMA targets with the same WET
3) carbon ion beams in tissue surrogates and in water targets with the same WET

were investigated. The water equivalent thickness (WET) of any material is the thickness of water required to cause the same amount of particle energy loss.
The experimental setup is described in Section 5.1. The novel method developed for the data analysis is described in Section 5.4.

5.1 The experimental setup and used parameters

A schematic representation of the experimental setup is shown in Figure 5.1. It consists of an incoming particle beam (carbon or helium ions), a target along the beam path, and four Timepix detectors placed perpendicular to the beam direction.

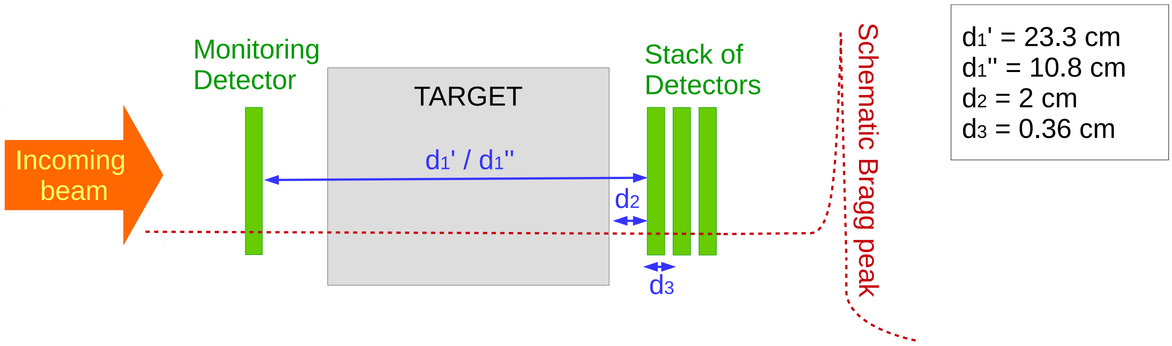

Figure 5.1: Schematic representation (not in scale) of the experimental setup. d_1 is the distance between first and second detector (d_1' in the first and second studies, *Fragmentation of Carbon/Helium Ions in Water and in PMMA*, d_1'' in the third study, *Fragmentation of Carbon Ions in Tissue and in Water*). d_2 is the distance between the target edge and the second detector. d_3 is the distance between the detectors in the stack.

One detector was placed in front of the target and other three were placed behind the target. The distance between the first and second detector was 23.3 cm in the first and second studies (*Fragmentation of Carbon/Helium Ions in Water and in PMMA*), and 10.8 cm in the third study (*Fragmentation of Carbon Ions in Tissue and in Water*). These distances were the minimum allowed by the thickest targets used in each study. The second detector was placed at the isocenter (1.05 m from the beam nozzle) in order to exploit the lasers in the experimental room for the detector positioning. This choice should improve accuracy in the detector positioning and reproducibility of the experiments. The distance between the distal edge of the targets and the second detector was also the minimum reachable, equal to 2 cm. A small distance between target and second detector improves the solid angle covered by the detectors and consequently the amount of detected particles.

Within a given study, the detectors were maintained at the same positions for all targets, and measurements were performed consecutively to reduce experimental uncertainties related to the detector positions. These choices enable to compare the results achieved within a given study, for different target materials and thicknesses.

Targets, beam and detector parameters used for the investigations are described in more detail in the following.

Ion beams

The targets were irradiated with carbon and/or helium ion beams. The used beam parameters are listed in Table 5.1. In the first two studies (*Fragmentation of Carbon/Helium Ions in Water and in PMMA*), the highest energies available at HIT were used to reduce unwanted particle scattering. In the third study (*Fragmentation of Carbon Ions in Tissue and in Water*), more common clinical beam energies were implemented. In particular, for adipose, inner bone and cortical bone targets, a beam energy suitable for a prostate treatment was chosen. For the case of lung, a lower beam energy which better suits to a lung treatment was used.

All measurements were performed in the plateau region of the depth dose curve, where healthy tissues are usually located.

Targets

General information on the targets characteristics can be found in Section 4.2.

For the first two studies, the same targets were used. They were 5 water and 5 PMMA targets, with WET between 5 cm and 18 cm. The water targets were built first; subsequently, the single PMMA slabs available, with geometrical thicknesses between 0.1 cm and 5 cm, were combined together such that the PMMA targets had WETs as close as possible to the corresponding water targets (the results are listed in Table 6.1).

In the third study, 4 Gammex tissue equivalent materials (lung, adipose, inner bone and cortical bone) were compared to 4 corresponding water targets. The WETs of the Gammex materials were first measured (see Table 6.2 for the results) and subsequently the water targets were built.

Table 5.1: Beam parameters used in the measurements

	Targets	Primary particle	Beam energy	Range in water
Study 1	Water - PMMA	Carbon ions	430 MeV/u	30 cm
Study 2	Water - PMMA	Helium ions	221 MeV/u	30 cm
Study 3	Lung - Water	Carbon ions	270 MeV/u	14 cm
Study 3	Adipose - Water	Carbon ions	351 MeV/u	22 cm
Study 3	Inner Bone - Water	Carbon ions	351 MeV/u	22 cm
Study 3	Cortical Bone - Water	Carbon ions	351 MeV/u	22 cm

Detectors

The silicon pixelated Timepix detectors, described in Section 4.2.3, were used for single particle registration. They can provide information on the particle position, arrival time and energy deposited in the sensitive area of the detectors. Only a laptop is required to operate the detectors, via the Pixetpro software. Additionally, another laptop was placed in the control room and used in remote mode. It enabled to check and change the detector parameters without the need to enter the experimental room. Various cables were also used to apply the bias voltage to the detectors, to connect the detectors to the laptop, and to provide power to the detectors. The last one is not strictly required, as the detectors can receive power via the USB cable as well; however, higher stability is reached when the power supplier is used.

The detector settings used are listed in Table 5.2, and the selection criteria discussed in the following.

Table 5.2: Detector parameters used in the measurements

Acquisition Time (Frame duration)	1 ms
Clock Frequency	10 MHz
Bias Voltage	30 V

- The acquisition time has to be long enough to allow measurement of the whole particle signal. In the present thesis, however, the acquisition time should be short enough to register a sufficiently low number of particles for each frame. This is particularly important for the data analysis, described in Section 5.4. A frame length of 1 ms was a good compromise for the purposes of this work.

- The clock frequency was set equal to 10 MHz as it was the same used for the detector calibration. Otherwise, correction factors for the measured pixel values were required.

- The bias voltage influences the particle charge collected in the detector and the resulting cluster size, as described in Section 4.2.3 and shown in Figure 4.6. Higher voltage values may improve the resolution of the particle energy measurements, as the lateral charge spread is reduced. However, higher voltages also lead to smaller cluster sizes for a given particle type. A narrower spectrum of cluster sizes for a mixed particle beam would then result, which is disadvantage in the present work, where the analysis of the cluster sizes enables to differentiate between particle species (see Section 5.4.2). A bias voltage of 30 V was used: on one hand, it allows a full depletion of the sensitive layer and thus a complete measurement of the particle charge; on the other hand good accuracy in the investigation of the ion spectra could be achieved.

The first detector operated in Time mode and was used to monitor the incoming beam particles (see Figure 5.1). Three detectors were placed behind the target and operated in ToT, Time and Time mode, respectively. The detector in ToT mode allowed particle species identification, while the last two detectors were used: 1) to correlate the particles behind the target with the corresponding primary ion in the monitoring detector; 2) for particle tracking. A detailed description of the particles matching procedure is provided in Section 5.4.
Alternatively, the last three detectors could be set in Time, ToT, Time mode, respectively, like in the work of Reinhart 2014. This choice might enable to increase the accuracy in the reconstruction of the particle trajectories and therefore the efficiency of the particles matching process. However, particle fragmentations and scattering in the second detector would affect the number, type and position of the particles registered in the third detector, operating in ToT mode. For the purposes of this thesis, the configuration ToT, Time, Time mode was found to be more convenient as it allows a higher quality in the particle species identification and quantification.

To minimize the detector misalignment, two identical PMMA supports[1] (shown in Figure 5.2) for the FITPix devices were used. They enabled to place the detectors at the same height with respect to the working table, and to reduce the lateral offsets between the first detector and the detectors in the stack. Moreover, a phantom support[1] was used to center the target with respect to the detectors.
Measurements to calculate the relative detector offsets were carried out at the beginning, during and at the end of each study. They are described in Section 5.2.2 and the results are shown in Section 6.1.2.

---

[1] built in-house at the DKFZ workshop

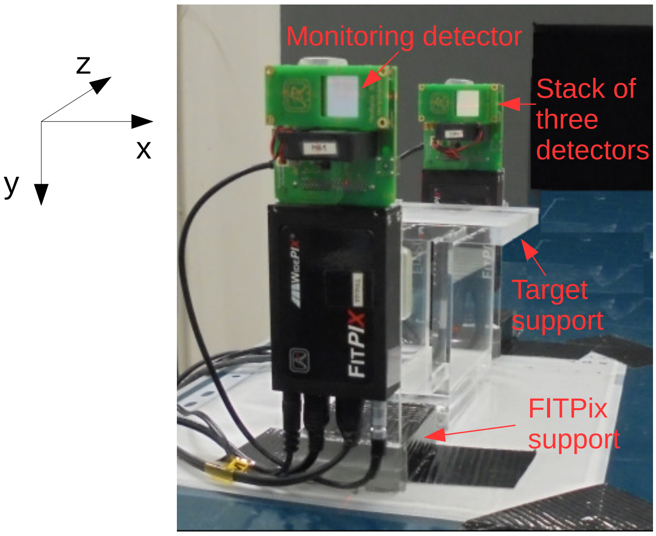

Figure 5.2: The experimental setup: one Timepix detector was placed in front of the target while three Timepix detectors were placed behind it.

5.2 Measurements prior the experiments

5.2.1 Measurements of the target thicknesses in terms of WET

The PTW PEAKFINDER water column was used to measure the WETs of the targets. The PeakScan software allows to operate and calibrate it. Adjustment of the electrometer parameters and a preliminary reference run were performed before starting the measurements. Subsequently, reference measurements of the Bragg peak positions for carbon ion beams were acquired without any sample, for three beam energies (200 MeV/u, 242 MeV/u, 329 MeV/u). Low energies are usually preferred as they allow sharper Bragg peaks and hence a more precise estimation of the Bragg peak position. However, due to the rather broad range of target thicknesses investigated in this work, three energies were necessary. A sampling step of 5×10^{-3} cm was set, which provided satisfactory precision in the measurements.

The Bragg peak positions were measured for all targets and were compared with the reference measurements (without the target), for the same beam energy. The WET of each target was then obtained as the difference between the two Bragg peak positions (with and without the target). Knowing the WET and the geometrical thickness of the targets along the beam direction (*Thickness*), the WEPL is given by:

$$WEPL = \frac{WET}{Thickness} \tag{5.1}$$

Uncertainty in the Bragg peak position measurements

An incorrect positioning of the PEAKFINDER or of the target in front of the PEAKFINDER could affect the results. Despite the use of the laser systems available in the experimental room, some degree of mis-positioning of the devices may take place.

Influences of a PEAKFINDER misalignment on the Bragg peak position were assessed in Sánchez Parcerisa 2012. For a Bragg peak placed at 30 *cm* in depth in the water column, it was estimated that an angle of 0.16° of the PEAKFINDER with respect to the beam axis leads to an error in the Bragg peak position of about 1μm. This uncertainty is much smaller than the experimental one related to the sampling step used here and therefore it was neglected.

The effect of a target mis-positioning in front of the PEAKFINDER was investigated in the present thesis. A PMMA target, 5 cm$_{\text{WET}}$ thick, and a lung equivalent material, 1.2 cm$_{\text{WET}}$ thick, were used. These two targets were selected to consider different target thicknesses and chemical compositions. The Bragg peak positions were measured with the two targets placed in front of the PEAKFINDER. Subsequently, the targets were rotated by about 5° degrees with respect to the beam axis, or shifted 1 cm far away from the PEAKFINDER's chamber entrance. The measurements of the Bragg peak positions were then repeated for the new target positions. The shifts in the Bragg peak positions obtained with the same target were compared to the sampling step used, in order to obtain the experimental uncertainty associated to the Bragg peak position measurements. The results can be found in Section 6.1.1.

5.2.2 Correction of the detector misalignment

To check and correct for detector misalignments, irradiations of the detectors without any target were performed. Carbon ions, with the highest available beam energy (430 MeV/u) and the smallest focus (0.34 cm FWHM) were used. With these choices, particle scattering, fragmentation in air and in the detectors, and beam divergence were considered minimal. In each detector the primary ions were selected using cluster size constrains and the mean positions of every clusters were calculated. The beam profile along the x and y (horizontal and vertical) axis were reproduced and were fitted by Gaussian curves. The positions of the peaks were used as the best estimation of the mean beam position in each detector. The first detector was set as reference, and the relative shifts (Dx and Dy) of the other detectors were calculated with respect to the position of the first detector.

At least 10^5 incoming particles were collected to assure high precision in the offset values: uncertainties below 1 pixel ~ 55 μm were achieved. The alignment measurements were repeated several times for each study: at the beginning, during and at the end of the measurements. This allowed to check unwanted but possible shifts in the experimental apparatus over time.

To verify the reproducibility of the calculated offsets and also to find the optimal experimental parameters, the alignment measurements were once performed with the detectors operating in different modes and using both carbon and helium ion beams.

5.3 Data acquisition and clustering

5.3.1 The experiments

As described in Section 4.2.3, each particle reaching the detector generates a signal which is collected in one or many adjacent pixels, forming a so called cluster. In general, size and shape of the cluster depend on the particle type, energy and impinging angle [Granja et al. 2007]. In this work particle trajectories are sufficiently perpendicular to the detector surface to generate round clusters.
In Figure 5.3 examples of frames obtained by two detectors, working respectively in Time mode (left) and in ToT mode (right), are shown. The first detector was placed in front of a water target, 18 cmWET thick, whereas the second detector was placed behind it. Secondary fragments produced within the phantom were registered in the second detector. It can be seen that carbon ions generated rather circular and much bigger clusters than those produced by the lighter secondary fragments.

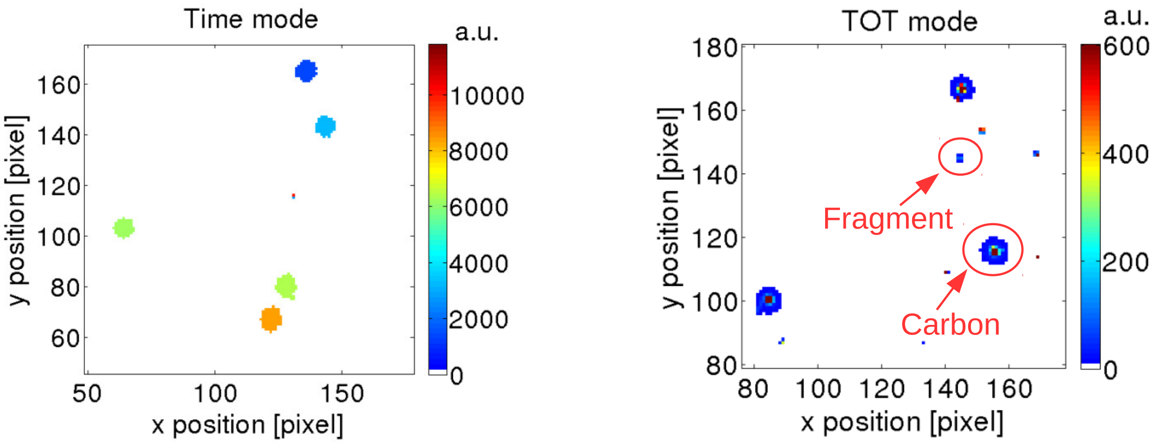

Figure 5.3: Examples of frames obtained by two detectors irradiated with a 430 MeV/u carbon ion beam. On detector (*left*) was placed in front of the target (a water phantom, 18 cmWET thick) and operated in Time mode. The other detector (*right*) was placed behind the target and operated in ToT mode. This image shows that the clusters produced by carbon ions are larger than those created by the secondary lighter fragments.

The software Pixetpro provides frame-based output files containing information on the x and y coordinates of the pixels forming a cluster and their pixel values. The particle arrival positions, particle arrival times, cluster size (number of pixels forming the cluster) and cluster signal (sum of pixel values within the cluster) were calculated and further analysed, as described in Section 5.4. For the detectors in Time mode, the particle arrival positions were obtained as the geometrical center of the clusters, while the highest pixel values within each cluster gives information on the particle arrival time. For the detector in ToT mode, the particle arrival positions were determined as the cluster centers weighted by the pixel values, whilst the sum of all the pixels values in a cluster (the cluster signals) is related to the particle deposited energies.

5.3.2 The simulations with FLUKA

In the present work the following versions of FLUKA were used: FLUKA 2011.2c.4 ([Ferrari et al. 2005, Battistoni et al. 2007]) for carbon ions, and a version currently under development (FLUKA devel [Böhlen et al. 2014]) for helium ions. The latter one was provided in advance from the FLUKA developers, and includes improvements on the nuclear interaction cross sections, especially as regards helium ion beams. General information on the settings and implementation of FLUKA in this work are described in the following.

A) Physics settings and B) Transport thresholds
The DEFAULTS physics card HADROTHErapy was used to optimize the particle scattering, by means of an inelastic form factor correction to Compton scattering, and to restrict the ionization fluctuations, which cause range straggling. In addition to the default settings provided by the HADROTHErapy card, the EVAPORAT and COALESCE cards were implemented to activate the evaporation and coalescence mechanisms, i.e. to take into account the residual nuclei and fragment productions, as well as the emission of energetic light fragments. The DECAYS card was also used to consider the decay processes of pions, muons and kaons. Particle transport threshold and δ-ray production threshold were set equal to 100 keV. Therefore, all particles with energies lower than 100 keV were not transported.

C) Radiation source
The radiation source was implemented by means of the SOURCE card. The phase space files developed at HIT [Tessonnier et al. 2016] were used. They describe the beam line geometry and provide the physical characteristics of the particles at the end of the beam line. Specific phase space files were provided for carbon and helium ion beams, and for each beam energy used in this thesis (listed in Table 5.1).

D) Geometry and E) Materials
The detector sensitive and insensitive layers were modeled like silicon layers, 300 μm and 100 μm thick respectively, and with a surface of 1.416×1.416 cm^2. The detector area was divided into 256×256 bins along the x and y axis, in analogy to the experimental pixels. The 256×256 bump bonds, made of a mixture of tin (63%) and lead (37%), were also included in the detector geometry. The card LATTICE, which enables to duplicate defined objects, was used for this purpose. As the detector sensitive area was divided into 256×256 pixels (55 μm pitch), like in the experiments, if particles hit the edge of

two or more pixels, the information was shared among the involved pixels. A clustering process was therefore required for the data provided by the simulations, too. The detectors were placed at the same positions like in the experiments (an illustration of the experimental set-up can be found in Figure 5.1).
The targets were modeled according to their experimental thicknesses, chemical compositions and densities:

- The water boxes have the same geometrical thicknesses like the experimental ones (Table 6.1 and Table 6.2). The PMMA walls, 0.3 cm thick each, were also included. For these targets, the default PMMA and WATER materials provided by FLUKA were used.
- The PMMA targets have same densities (Table 4.2) and geometrical thicknesses (Table 6.1) as in the experiments. The ionization potential was set equal to 75 eV, as suggested by ICRU-49.
- For the tissue targets, the densities and elemental compositions provided by the Gammex manufacturer were used (Table 4.3). Each target was 4 cm thick, like in the experiments.

F) Scoring
EVENTBIN was used together with the user routine COMSCW to score event by event and to register deposited particle energy and positions. The default COMSCW routine was adjusted to differentiate between lithium, beryllium, boron and carbon ions, which otherwise are classified together as general HEAVYION.

For each target configuration, 10 cycles with 10^5 initial particles were run, for a total of 10^6 incoming particles. The number of particles in the simulations was about 4-5 times higher than in the measurements.

5.4 Data analysis

Experimental and simulated data were analysed with self-written routines in C++ and MATLAB. C++ was mainly used in the first part of the data analysis to benefit from the higher flexibility, performance and speed provided by this programming language. MATLAB was used to finalise the data analysis and for the result visualizations.

5.4.1 The particles matching method

The development of the particles matching method was a major part in the present thesis and it is the core of the data analysis. In previous ion spectroscopy studies carried out within the research group [Hartmann 2013], only one detector behind the target was used. In this work four detectors were implemented (see Figure 5.1), operating in synchronization. Time coincidence measurements were then possible and enabled to correlate corresponding particles registered in front and behind the phantoms. Indeed, particles with the same arrival time (within the experimental uncertainty) belonged to the same event. Here “same event” can refer to two different scenarios:

1) a given particle recorded in the first detector traveled through the target and crossed the detectors behind it;

2) a given particle recorded in the first detector underwent fragmentation within the target and the arising secondary fragments were measured behind the target.

Hence, both residual primary ions and secondary fragments registered behind the investigated phantoms could be matched to the corresponding primary particle in the first detector. As a result, single events could be analysed and the fragmentation of each single primary ion could be investigated. Moreover, the results could be normalized to the number of incoming primary ions.
The only requirement for this method to work properly is a sufficiently low beam intensity. Otherwise, separation of different events in time is not possible. With the used detector settings (Table 5.2), the detectors time resolution is of the order of few ns. The beam intensity was then set such to be lower than 10^4 particles/s (which corresponds to about several incoming particles per frame).
The particles matching procedure is described in detail in the following.

Step 1 : Selection of the incoming primary ions

1.1) Selection of the particle positions

Particles registered in the first detectors may not be detected in the detectors behind the target mainly because of fragmentation in the phantom, scattering, beam divergence, great angle trajectories, detector misalignment. For particles reaching the first detector close to the edge, the probability not to find matching particles in the detectors behind the target is higher. Therefore, only particles impinging the first detector in the central area were selected. The maximal distance allowed between the particle positions and the center of the detector was 46 pixels ($\sim$ 0.25 cm). This value was chosen as it provides the best compromise between the cut here performed and a subsequent cut which is applied in *Step 3 : Selection of the particles in the second detector* (described later in the text). All the particles beyond 46 pixels ($\sim$ 0.25 cm) from the center were excluded from the data analysis.
The total number of incoming particles was reduced by about 50%. Despite the consequent increase in the statistical uncertainties, this cut enabled to improve the quality of the data analysis significantly.

An analogous selection was performed both in the experimental and in the simulated data.

1.2) Selection of the primary particle type

In FUKA each single event was scored separately and different particle species were clearly and unequivocally labeled. Therefore, selection of the primary ions was rather easy to perform.

In the experimental data, instead, analysis of the cluster size was required to identify the primary ions in the first detector. Examples of cluster size distributions are shown in Figure 5.4, for carbon and for helium ions. At the used energies, the carbon ions generated clusters of 30-80 pixels, while the cluster size for helium ions were between 5 and 20 pixels. A cut on the minimum and maximum cluster size enabled to select the primary ions and therefore to get rid of most of the detector artifacts, lighter particles produced in the BAMS and overlapping particles. These particles usually produce smaller or bigger clusters than the primary beam particles.

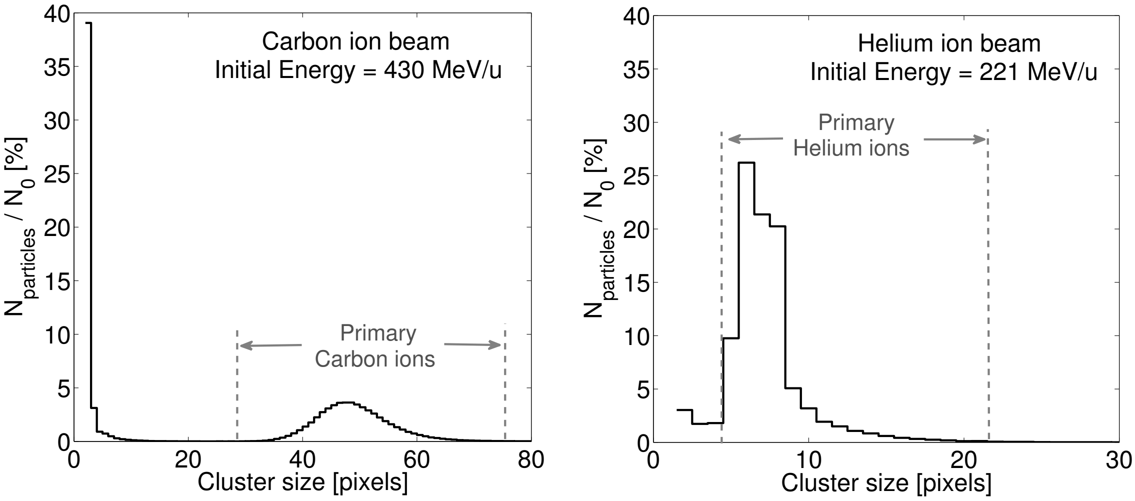

Figure 5.4: Examples of cluster size distributions obtained in a Timepix detector irradiated with a 430 MeV/u carbon ion beam (*left*) and a 221 MeV/u helium ion beam (*right*). The peaks for the primary particles are clearly distinguishable from detector artifacts and signal due to lighter particles.

1.3) Selection of the primary particle arrival times

- All the particles arriving before 0.3×10^{-6} s from the beginning of the frame were excluded. 0.3×10^{-6} s was the maximum difference in time allowed to consider two events in coincidence. This value is the experimental uncertainty related to the synchronization of the two Fitpix devices. It was derived by Figure 5.6, left, and it is further discussed in the next paragraph (*Step 2 : Matching of particles belonging to the same event*).

- Particles arriving close to the end of the frame were also excluded, as there was not enough time to fully measure the particle signal. For those particles, the registered signals were lower than the expected ones, and therefore they would have contributed to the final findings with incorrect information. The maximum of the highest pixel values over the all clusters registered in the detector operating in ToT mode was a good estimation of the minimum time required to measure the entire particle signal. This time value depends on the particle energy and therefore varied for each experimental configuration. Depending on the target thickness, the estimated value was between 40% and 60% of the total frame duration (1 ms). Therefore, this cut strongly reduced the number of primary particles considered, but it improved the quality of the data analysis.

1.4) Selection of the maximum number of primary particles per frame

In order to reach the desired low intensity (less than 10^4 particles/s), the standard clinical settings, with beam intensities between (10^6 - 10^8) particles/s, could not be used. The beam intensity was adjusted by specialized personnel in the accelerator control room. The main disadvantage of this approach was a more unstable beam intensity over time. As a consequence, in some frames the number of registered incoming particles was too high to allow a clear and unequivocal separation of the particles in time and in space. Frames with more than 6 incoming primary ions were then excluded from the data analysis. Up to that number, correlation of the particles in front and behind the targets was possible with a low percentage of ambiguities ($\leqslant$2%, as further discussed in *Step 2 : Matching of particles belonging to the same event*). This cut reduced the number of primary particles in the data sets by about 1% - 2%.

1.5) Exclusion of the ambiguities

Despite the very low beam intensity and the cuts described above, in some cases two primary ions were registered in the first detector at the same time. These particles were excluded from the further data analysis as they do not allow an unequivocal matching between particles detected in front and behind the targets. However, their percentage was very low ($<$0.3%), as most of these events were already excluded with the previous cuts.

The number of remaining primary ions in the first detector after all the cuts and constrains described in *Step 1 : Selection of the incoming primary ions* was used as normalization factor.

Step 2 : Matching of particles belonging to the same event

Experiments

A schematic representation of the matching process is shown in Figure 5.5. Particles in the third and fourth detectors were correlated to the respective primary particle in the first detector based on their arrival time in the detectors. The low beam intensity was necessary here to enable a clear separation of the particles in time and hence to avoid ambiguities.

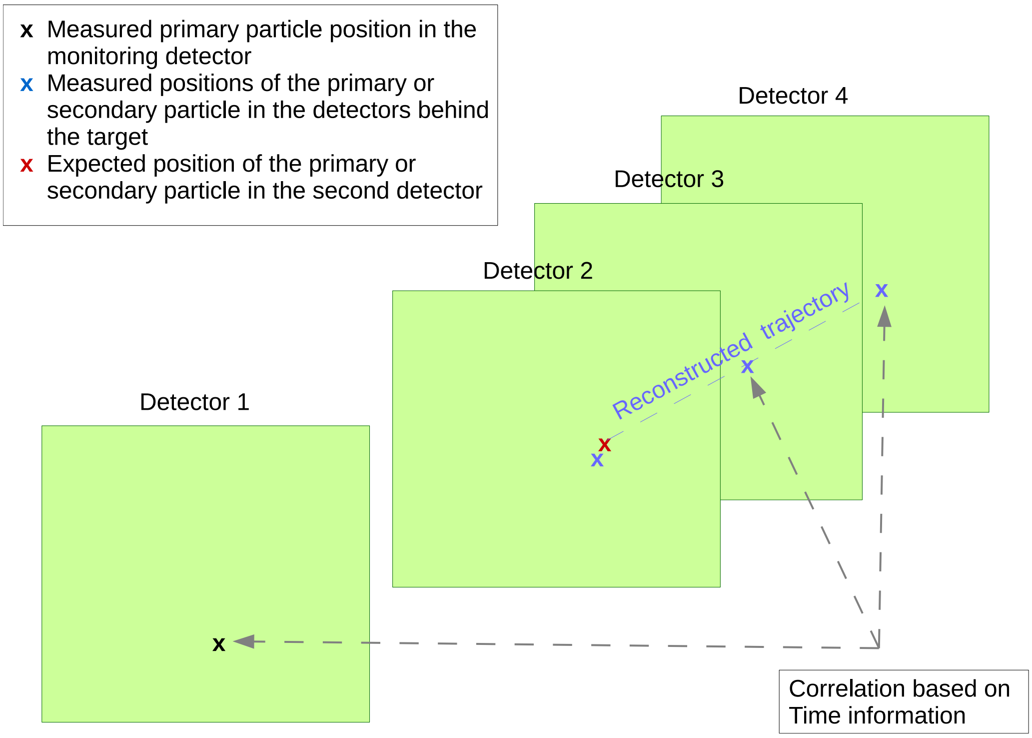

Figure 5.5: Schematic illustration of the particles matching process. Particles in the first, third and fourth detectors were correlated based on their arrival time in the detectors. The corresponding particle in the second detector was then found reconstructing the particle trajectory. A distance up to 5 pixels (∼ 0.03 cm) between expected and measured particle positions was allowed. *Note*: the target, placed between the first and second detector, is not shown here; see Figure 5.1 for a representation of the whole experimental setup.

Figure 5.6, left, is a typical example of the smallest differences between particle arrival times registered in the first detector and particle arrival times registered in the third detector. These values were usually smaller than 0.3×10^{-6} s. Based on this result, a maximal difference in time equal to 0.3×10^{-6} s was allowed to consider two particles belonging to the same event. This value can be considered as the experimental uncertainty associated to the synchronization of the two Fitpix devices.

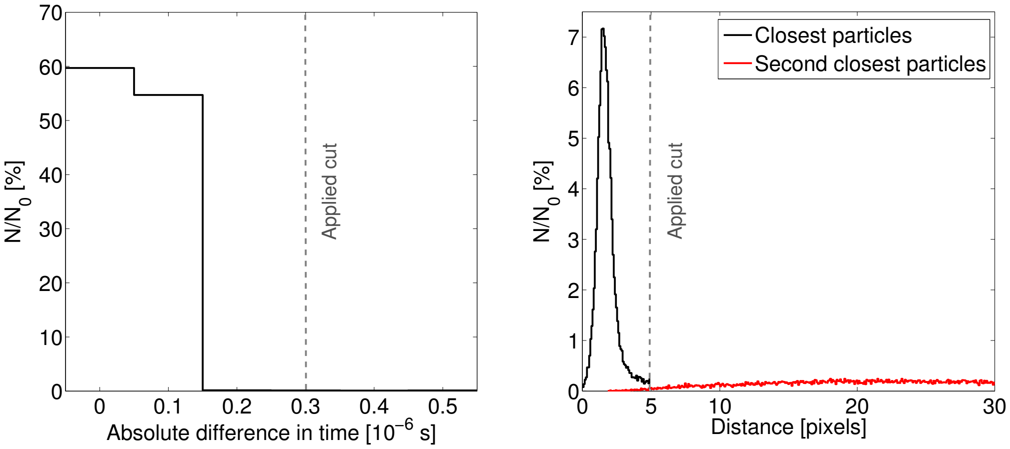

Figure 5.6: A water target, 18 cm WET thick, was irradiated with a 430 MeV/u carbon ion beam. *Left*: Smallest differences between the particle arrival times registered in the first and in the third detector. Based on this result, differences in time smaller than 0.3×10^{-6} s were accepted for particles in coincidence. *Right*: Distribution of the distances between expected and measured particle positions in the second detector. The black line refers to the particles closest to the expected positions, whereas the red line refers to the second closest particles. The image shows only values up to 30 pixels (~0.17 cm).

As the second detector operated in ToT mode, no information on the particle arrival times was provided. The positions of matching particles in the third and forth detectors were then used to reconstruct the particle trajectories and to obtain the expected particle position in the second detector (as shown in Figure 5.5). This position was compared with all particle positions registered in the second detector, and the closest one was selected. However, a limit on the maximum distance allowed between the expected and the closest measured particle positions needed to be applied. The black line in Figure 5.6, right, shows an example of distribution of the distance values, calculated between expected and closest particle positions. The results were obtained with a 430 MeV/u carbon ion beam, crossing a water target, 18 cm WET thick. A peak is clearly visible, centered at about 3 pixels (~ 0.015 cm). This shift can be related to three factors: 1) scattering effects in the detectors, which distort the particle trajectories; 2) residual misalignment between the detectors, despite the alignment corrections; 3) experimental uncertainties on the calculation of the cluster centers, which affect the reconstruction of the particle trajectories. However, despite the measured shift, this peak was much sharper than the distribution of the distances between the expected particle positions and the second closest particle positions (red line in Figure 5.6, right). The second closest particles are random particles belonging to a different event. The low beam intensity played an important role here, as it guaranteed a clear separation in space between the particles in the second detector. Based on those results, a maximum distance of 5 pixels (~ 0.03 cm) between the expected and the measured particle positions in the second detector was allowed for matching particles.

When multiple fragments were detected, for a single primary ion more than one particle in the third and fourth detectors were registered with the same arrival time as the primary particle in the first detector. All the possible combinations of particle trajectories were then considered, using the positions of the fragments in the third and in the fourth detectors. For each potential trajectory, the corresponding particle in the second detector was searched. If no particle was found within a distance of 5 pixels ($\sim$ 0.03 cm) from the expected position, the trajectory was considered wrong and consequently the two fragments in the third and fourth detectors were not a correct match. In this way, only good matches and good trajectories were selected.

In few cases (about 1-2 %) a given particle in the second detector could satisfy the requirements for two different trajectories or conversely two particles in the second detectors were found within 5 pixels ($\sim$ 0.03 cm) from the expected particle position. These cases were further analysed, comparing e.g. the cluster size of the particles in three detectors placed behind the target. If this analysis allowed to clearly identify the correct trajectory, this one was selected while the other one was discarded. If an unequivocal identification of the correct trajectory was not possible, the whole frame was deleted in the data set. This choice was considered to be the safest option to preserve the quality of the final findings. The percentage of the excluded frames was less than 1% of the total number.

Simulations

In the data files obtained from the simulations, information on the particle species was provided. Moreover, each event was scored individually, so matching particles were already gathered together. However, for an unbiased comparison between measurements and simulations, the analysis approach previously described was applied to the simulated data, too. Using the positions of the particles in the third and fourth detectors, the particle trajectories were reconstructed. The distances between the expected and the closest measured particle positions in the second detector were calculated. If the distance was greater than 5 pixels ($\sim$ 0.03 cm), the particle was rejected, as it was done in the experimental data. Multiple fragments, repetitions and ambiguities were treated like in the experimental data.

Step 3 : Selection of the particles in the second detector

The positions of the primary particles were registered in the first detector. The trajectories of these particles would be straight lines parallel to the beam axis, if no physical processes (e.g. particle fragmentation, scattering) and experimental uncertainties (e.g. beam divergence) take place. The expected primary particle positions in the second detector were then obtained as the projection of their positions in the first detector along lines parallel to the beam axis. The projected primary particle positions and the positions of the corresponding particles (primary or secondary) measured in the second detector were compared. For the reasons mentioned previously (physical processes and

experimental uncertainties), differences between the projected and the measured positions were observed. Moreover, in some cases no matching particles behind the target were found for a given primary particle registered in the first detector.
In the following, two scenarios of possible events are described and they are illustrated in Figure 5.7:

- Case a) : the primary particle reaches the first detector close to the center; the corresponding particle (primary or secondary) hits the second detector at a certain distance, d, to the projected primary particle position in the second detector.
- Case b) : the primary particle position reaches the first detector closer to the edge of the detector. The relative distance, d, between the projected primary particle position in the second detector and the position of the corresponding particle measured in the second detector is the same as in *Case a)*. However, in this scenario, the outgoing particle travels out of the area covered by the second detector.

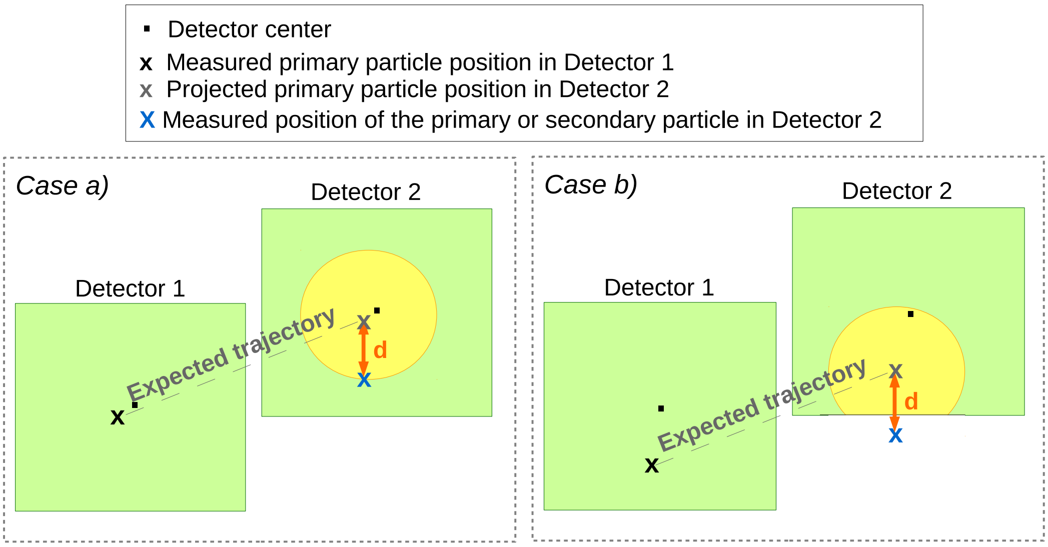

Figure 5.7: A primary particle is registered close to the center of the first detector (*Case a)*) or closer to the edge of the first detector (*Case b)*). The relative distance, d, between the particle position recorded in the second detector and the primary particle position registered in the first detector and projected in the second detector is the same in *Case a)* and in *Case b)*. However, in the second case, the particle travels out of the second detector area. *Note*: the target, placed between the first and second detector, is not shown here; a representation of the whole experimental setup is available in Figure 5.1.

This comparison shows that the probability of not finding matching particles for a given primary ion in the first detector increases with increasing its distance to the center of the detector. To avoid an influence of the primary particle arrival position on the results, an additional constrain on the maximum distance allowed between the particle positions in the first and in the second detector was introduced. A value equal to 64 pixels (∼0.35 cm) was used, as a consequence of the detector size and of the cut performed in *Step 1.1): Selection of the particle positions*. This is illustrated in Figure 5.8, where the extreme scenario is depicted.
A primary particle reaches the first detector at a distance $R_1^{max} = 0.25$ cm to the center (maximum distance allowed in *Step 1.1): Selection of the particle positions*); the corresponding particle in the second detector has a distance $R_2^{max} = 0.35$ cm to the projected primary particle position. The sum of these values, $R_1^{max} + R_2^{max} = 0.6$ cm, still leaves a margin of $L - R_1^{max} + R_2^{max} \sim 0.1$ cm to the detector edge. This residual margin was considered to take into account experimental uncertainties related to the detector positioning, and to guarantee a sufficient number of pixels for the lateral charge spread and therefore for the collection of the entire particle signal.

The same maximum lateral distance between the positions of the particles in the first and in the second detector was used in the simulations.

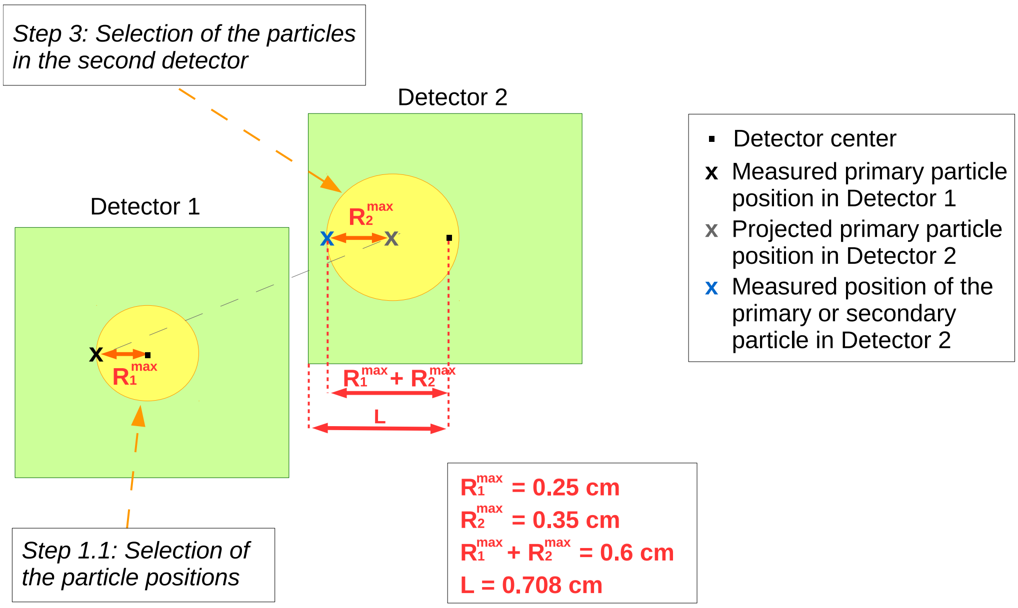

Figure 5.8: A primary particle reaches the first detector at the maximum distance to the detector center, R_1^{max}, allowed in *Step 1.1): Selection of particle positions*. The corresponding particle in the second detector has the maximum distance to the projected primary particle position, R_2^{max}, allowed in *Step 3 : Selection of the particles in the second detector*. A margin of 0.1 cm to the detector edge remains. *Note*: the target, placed between the first and second detector, is not shown here; a complete representation of the experimental setup is shown in Figure 5.1.

5.4.2 Investigations of the ion spectra in mixed fields

As demonstrated in Hartmann 2013, cluster structures and features depend on the particle species. Therefore, analysis of the cluster size and cluster signal enables to identify and differentiate between particle species. Figure 5.9 shows an example of a 2D distribution of the measured clusters in variables of cluster signal and cluster size. The detector was operating in ToT mode and placed behind a 18 cmWET thick water phantom irradiated with a 430 MeV/u carbon ion beam. Different regions belonging to different particle types (primary ions or secondary particles produced in the target) are recognizable. In a semi-log plot, these regions have approximately round or elliptical shapes. Quantification of the particles registered behind the targets was performed via hand drawn regions in the 2D scatter plots of cluster signal and cluster size.

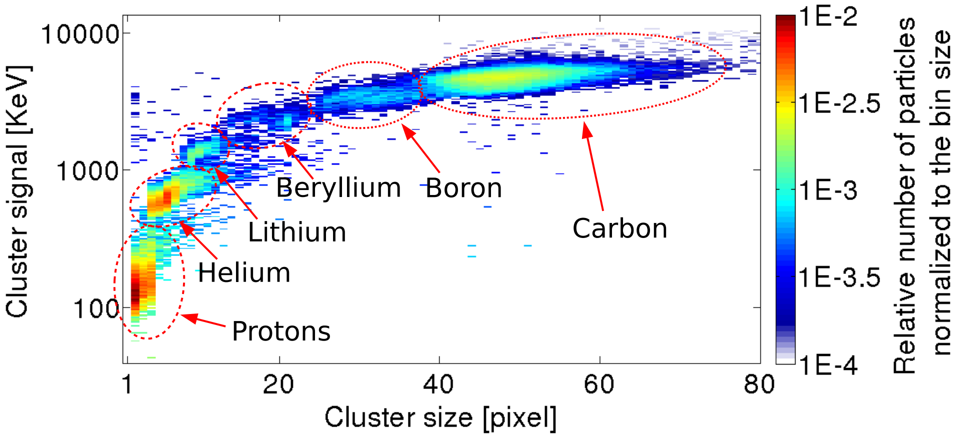

Figure 5.9: Example of a 2D distribution of measured clusters in variables of cluster signal and cluster size, obtained behind a water target, 18 cmWET thick, irradiated with a 430 MeV/u carbon ion beam. Different particle species can be distinguished based on their cluster signal and cluster size.

Figure 5.10 shows examples of 2D scatter plots of cluster signal and cluster size, before and after applying the particles matching procedure described in Section 5.4. In the plot on the left, obtained from the raw data, particles arriving during the detector dead time, particles arriving close to the end of the frame, as well as electrons and background signals are visible. The first group is characterized by high cluster signals and small cluster sizes. They mainly contribute in the upper-left area of the 2D scatter plot. The second group have the expected cluster size but lower cluster signals, as the lateral charge diffusion took place but not the whole signal was collected. Hence, they mainly contribute to widen the particle regions downward. Finally, electrons and background signal are characterized by small cluster sizes (1-2 pixels) and low cluster signals, and therefore their contribution can be found on the lower-right part of the 2D scatter plot. After application of the particles matching procedure, most of these unwanted contributions have been excluded, as shown in Figure 5.10, right.

With respect to the previous studies [Hartmann 2013], the particles matching procedure enables to improve the accuracy in the identification of the particle species, which is performed via hand drawn regions in the 2D scatter plots of cluster signal and cluster size. A quantitative analysis of the uncertainties related to this method can be found in Section 5.5.3.

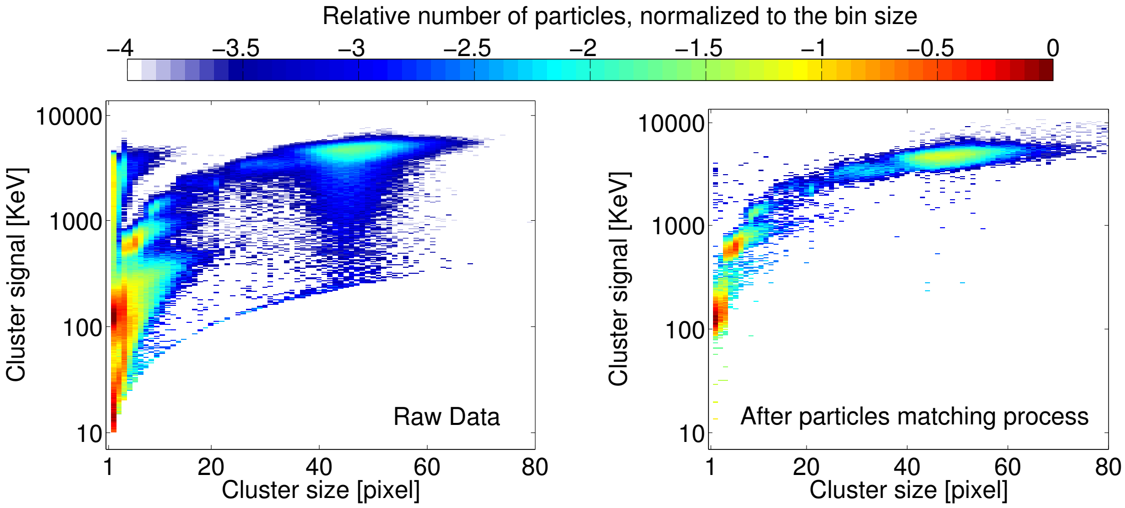

Figure 5.10: Examples of 2D distribution of measured clusters in variables of cluster signal and cluster size, obtained behind a water target 18 cmWET, irradiated with a 430 MeV/u carbon ion beam. *Left*: Raw data were used for the plot. *Right*: The particles matching method, described in Section 5.4, was applied to the raw data, and the resulting new data set was used for the plot.

5.4.3 Analysis of the lateral particle distributions

The lateral distances between the primary particle positions in the first detector and the measured positions of the corresponding particles in the second detector were determined. A maximum distance equal to 0.35 cm was allowed (see Section 5.4, *Step 3 : Selection of the particles in the second detector*). This constrain, combined with the others, assures that all the primary particles contribute equivalently to the results, without any dependency on their arrival positions in the first detector.

In the measurements with carbon ion beams (Study 1, *Fragmentation of Carbon Ions in Water and in PMMA*, and Study 3, *Fragmentation of Carbon Ions in Tissue and in Water*), particles were gathered in three groups:

1. carbon ions (^{12}C, ^{11}C, ^{10}C)
2. light fragments : H + He
3. heavy fragments : Li + Be + B

This grouping allows a more meaningful comparison of the results and also to reduce the statistical uncertainties. The latter one is particularly convenient for the heavy fragments, which were detected in small abundance.

In the measurements with helium ion beams (Study 2, *Fragmentation of Helium Ions in Water and in PMMA*), two groups were used:

1. helium ions (^{4}He, ^{3}He)
2. secondary H (protons, deuterons and tritons)

The distributions of the particles behind the targets as a function of their lateral distances to the incoming primary particle positions were analysed up to 0.35 cm. As the sampling step was kept constant, the annulus area around the primary particle position became larger with increasing distance value. The results were hence normalized to the annulus area. The width of the distance distributions were compared between targets with the same WET, as well as for different target thicknesses, particle species, and between measurements and simulations.

Mean distance values, d_{mean}, were calculated to enable further comparisons between the results, especially among different target thicknesses and particle species.

Additionally, the maximum distances achieved by 80% of the particles, $d_{max(80\%)}$, were estimated. As these values were extrapolated by the distance distributions (examples are shown in Figure 6.8), the associated uncertainty should be half of the sampling step used. However, irregularities in the distributions may influence the results significantly. Therefore, to improve the accuracy in the results, three adjacent bins were considered (the one corresponding to 80% of the particles, the previous one and the following one) and an average of the amount of particles measured on those bins was calculated. The standard rules of error propagation were used to determine the uncertainties associated to the $d_{max(80\%)}$ values.

Finally, d_{mean} and $d_{max(80\%)}$ were compared for different target thicknesses, particle species, and between measurements and simulations, to obtain a qualitative information on the width of the lateral particle distributions: the greater is d_{mean} with respect to $d_{max(80\%)}$ the sharper is the lateral distribution, and vice versa.

5.5 Analysis of the experimental uncertainties

Particle scattering and a residual misalignment between the detectors in the stack, despite the corrections applied and described in Section 5.2.2, were taken into account during the particles matching program (Section 5.4), allowing a distance of 5 pixels ($\sim$ 0.03 cm) between the expected and the measured particle positions in the second detector (see *Step 2 : Matching of particles belonging to the same event*).

Regarding possible relative rotations of the detectors, it was estimated that detector angles up to 10° with respect to the beam axis would influence the registered particle

positions by just 1 pixel (~ 55 μm) in the worst case. The effects of detector misorientations were then considered negligible.
Other experimental uncertainties which were considered in this work are:

1. Statistical uncertainties (given by the square root of the number of detected particles)
2. Uncertainties on the calculation of the offsets between the first and second detector. They may cause a residual misalignment between those detectors, despite the alignment corrections (described in Section 5.2.2).
3. Differences between the WETs of the targets investigated. They would influence the residual particle energies behind the targets.
4. Uncertainties on the quantification of the particles detected behind the targets, performed via hand drawn regions in the 2D scatter plots of cluster signal and cluster size (as described in Section 5.4.2).

In the next sections, these uncertainties and their influence on the results are analysed in more details.
Propagation of the uncertainties was performed over the whole thesis by using the basic standard rules, unless otherwise specified.

5.5.1 Uncertainties on the calculation of the offsets between the detectors

Assessment of the uncertainties
To assess the accuracy of the calculated offsets between the first and second detector, the first detector was shifted with respect to the other one, between -5 pixels and +5 pixels (~0.03 cm), along the x or the y (horizontal and vertical) axis. These shifts were applied offline on the experimental data sets, so no real movements of the detector were performed during the measurements. The effects of the shifts on the particles matching efficiency were investigated. “Particles matching efficiency” refers to the efficiency of the particles matching method described in Section 5.4. It was determined as the number of incoming primary ions having at least one matching particle in the second detector, normalized to the number of incoming primary particles. However, as the position of the first detector does not play any role in the first two steps of the data analysis procedure, the shifts applied on the first detector actually affect only *Step 3 : Selection of the particles in the second detector*.
From the results achieved here, the uncertainty in the relative positions between the first and second detector was obtained.

Influence of a residual detector misalignment on the results

In the previous paragraph, the uncertainties in the calculation of the offset values between the first and second detector were assessed. They were found to be $\leqslant$1 pixel ($\sim$55 μm) (results are available in Section 6.5.1). Due to these uncertainties, a residual misalignment between the two detectors was considered, and its influence on the results was investigated. The first detector was shifted by ± 1 pixel along the x or the y (horizontal and vertical) axis, with respect to the other detector. Also in this case, the shifts were applied offline to the data sets, and not to the detector during the experiments. The number of particles detected behind the phantoms were quantified by means of hand drawn regions in the 2D scatter plots of cluster signal and cluster size. The particle species quantification was repeated for the same target, with and without applying the shifts on the first detector. The differences in the number of particles obtained were compared to the statistical uncertainties. For a given target, the same hand drawn regions were used to minimize the influence of the region sizes and shapes on the results. The influence on the lateral particle distributions were also analysed. Comparisons of the d_{mean} values obtained for different positions of the first detector are shown in this thesis.

5.5.2 Uncertainties due to the different WETs of the targets

Due to experimental limits, coupled targets have WET as close as possible, but not identical. To estimate the influence of the different WETs between the targets on the results, two targets were used: PMMA 15 cm$_{\text{WET}}$, with a WET equal to (14.54±0.03) cm, and a thicker PMMA phantom, named PMMA 15^{+} cm$_{\text{WET}}$, with a WET equal to (14.61±0.03) cm. The WETs of the two phantoms are not consistent whithin their uncertainties. The targets were irradiated with a 430 MeV/u carbon ion beam. Quantification of the particles detected behind the phantoms were performed via hand drawn regions in the 2D scatter plots of cluster signal and cluster size (as described in Section 5.4.2). The same regions were used for the two targets, so to exclude any dependency on the region sizes and shapes. The lateral distributions of the carbon ions and of the lighter fragments behind the two targets were also compared.

5.5.3 Uncertainties related to the hand drawn regions

Particle species detected behind the investigated targets were quantified in 2D scatter plots of cluster signal and cluster size by means of hand drawn regions, as described in Section 5.4.2. To minimize the influence of the region sizes and shapes on the calculated number of particles, same hand drawn regions were used for targets with the same WET. This enables a direct comparison of the results obtained for coupled targets.

However, to assess the uncertainty related to this method, the influence of different regions on the quantification of the detected particles was investigated. For a given phantom, the numbers of particles registered behind the target were calculated for each particle species. Those values were used as reference. Subsequently, smaller and larger regions were drawn in the same 2D scatter plot of cluster signal and cluster size, for all particle species . The numbers of detected particles were then recalculated using the new regions. These new numbers can be considered as a under- (from the smaller regions) and an over- (from the larger regions) estimation of the particles detected behind the target. The differences between the under- and the over-estimations with respect to the reference values were compared to the statistical uncertainties.

This analysis was carried out for phantoms with different thicknesses and chemical compositions, and both for measurements with carbon ion and with helium ion beams. The various experimental configurations may influence the results differently.

6 Results

6.1 Measurements prior the experiments

6.1.1 Measurements of the target thicknesses in terms of WET

The aim of this thesis is to compare the nuclear interactions of carbon and helium ions in water and in PMMA (Study 1 and Study 2) or in tissue surrogates and in water (Study 3). Details on the targets used can be found in Section 4.2.1.

To allow a direct comparison of the results between different target materials, the investigated targets should have in pairs WETs as close as possible. A PTW PEAKFINDER water column (described in Section 4.2.2) was used to measure the WET of the phantoms. The WEPL values were obtained using Equation 5.1. The results are listed in Table 6.1 and Table 6.2.

Good agreement was reached for the targets in pairs, with differences smaller than the experimental uncertainty. The WEPL values of PMMA and of the tissue surrogates differ from the value of 1. This factor together with the experimental limits on the constructions of the PMMA and of the water targets cause differences in the geometrical thickness between coupled phantoms. As Table 6.3 and Table 6.4 show, the greatest differences were found in the case of Lung and Cortical Bone (71% and 63% respectively) with respect to their corresponding water targets. In the other cases the absolute differences were between 7% and 13%.

Uncertainty in the WET measurements

In order to assess the experimental uncertainty in the WET measurements, the changes in the Bragg peak positions measured with the PEAKFINDER for two test targets (PMMA 5 cm_{WET} and Lung) were analysed. Measurements were repeated for different positions and orientations of the targets in front of the PEAKFINDER device, as described in Section 5.2.1. Variations between 0.015 cm and 0.02 cm in the Bragg peak positions were observed. As these values are greater than the uncertainty arising from the sampling step (3×10^{-3} cm), an uncertainty of 0.02 cm was associated to the Bragg peak position measurements performed in this thesis. The phantom thicknesses were measured by means of a Vernier caliper and the associated uncertainty was 0.01 cm. The resulting uncertainty of the WET values were then equal to 0.03 cm.

Table 6.1: Measured WET and corresponding WEPL of the used water and PMMA targets. The uncertainties of the WET and geometrical Thickness are 0.03 cm and 0.01 cm, respectively, as explained in the text. The uncertainties of the WEPL were calculated according to the rules for error propagation.

Target labeling	WET (cm)	Thickness (cm)	WEPL
Water 5 cm_{WET}	5.17	5.09	-
PMMA 5 cm_{WET}	5.15	4.51	1.143 ± 0.007
Water 7 cm_{WET}	7.59	7.50	-
PMMA 7 cm_{WET}	7.60	6.60	1.151 ± 0.005
Water 10 cm_{WET}	9.84	9.27	-
PMMA 10 cm_{WET}	9.84	8.56	1.149 ± 0.004
Water 15 cm_{WET}	14.57	14.50	-
PMMA 15 cm_{WET}	14.54	12.64	1.151 ± 0.003
Water 18 cm_{WET}	18.04	17.98	-
PMMA 18 cm_{WET}	18.06	15.65	1.154 ± 0.002

Table 6.2: Measured WET and corresponding WEPL of the used Gammex materials and water targets. The uncertainties of the WET and geometrical Thickness are 0.03 cm and 0.01 cm, respectively, as explained in the text. The uncertainties of the WEPL were calculated according to the rules for error propagation.

Target labeling	WET (cm)	Thickness (cm)	WEPL
Lung	1.22	4	0.305 ± 0.008
Water(Lung)	1.22	1.16	-
Adipose	3.85	4	0.962 ± 0.008
Water(Adipose)	3.84	3.8	-
Inner Bone	4.52	4	1.129 ± 0.008
Water(Inner Bone)	4.50	4.48	-
Cortical Bone	6.58	4	1.644 ± 0.009
Water(Cortical Bone)	6.55	6.51	-

Table 6.3: Comparison of the measured WET and geometrical Thickness for the used water and PMMA targets.

Targets	Difference in Thickness (%)
Water vs PMMA, 5 $\mathrm{cm}_{\mathrm{WET}}$	+11.4
Water vs PMMA, 7 $\mathrm{cm}_{\mathrm{WET}}$	+12.0
Water vs PMMA, 10 $\mathrm{cm}_{\mathrm{WET}}$	+7.7
Water vs PMMA, 15 $\mathrm{cm}_{\mathrm{WET}}$	+12.8
Water vs PMMA, 18 $\mathrm{cm}_{\mathrm{WET}}$	+13.0

Table 6.4: Comparison of the measured WET and geometrical Thickness for the used Gammex materials and water targets.

Targets	Difference in Thickness (%)
Lung vs Water	+71.0
Adipose vs Water	+5.0
Inner Bone vs Water	-12.0
Cortical Bone vs Water	-62.8

6.1.2 Correction of the detector misalignment

For the investigations carried out in this thesis, four detector layers were used, as shown in Figure 5.1. Measurements to address the experimental misalignment between the detectors were performed at the beginning, during and at the end of each study. The relative offsets were determined as described in Section 5.2.2. In the post-processing of the data, the detector positions were shifted to correct the misalignment.

To check the reproducibility in the estimation of the offset values and to find the optimal configuration (i.e. beam particle, beam energy, detector setups) for this kind of measurements, several tests were performed. The detectors were kept in fixed positions and the beam and detector readout parameters were varied. As an example, Table 6.5 shows the relative shifts determined with:

- carbon ions and all the detectors in Medipix mode;
- carbon ions and the detectors in Time, ToT, Time, Time mode respectively;
- helium ions and the detectors in Time, ToT, Time, Time mode.

The first detector was used as reference.

Table 6.5: Comparison of alignment measurements performed with C or He ion beams and with different combinations of detector operation modes. Detector 1 was used as reference; Dx and Dy are the shifts of the other detectors with respect to the first one. 1 pixel ∼55 μm.

	430 MeV/u C ion beam Medipix mode		430 MeV/u C ion beam T-, ToT-, T-, T-mode		221 MeV/u He ion beam T-, ToT-, T-, T-mode	
	Dx (pixels)	Dy (pixels)	Dx (pixels)	Dy (pixels)	Dx (pixels)	Dy (pixels)
Detector 1	-	-	-	-	-	-
Detector 2	-4.3	-7.6	-4.2	-8.1	-4.3	-7.8
Detector 3	-3.7	-5.3	-3.5	-5.2	-3.9	-4.7
Detector 4	-3.6	-9.3	-2.7	-9.4	-3.8	-8.7

The differences between the values calculated in the three configurations do not exceed 1 pixel (∼55 μm). As no significant dependency on the particle type and detector mode was observed, the final alignment measurements were performed with 430 MeV/u carbon ion beams. This high beam energy and the great mass and charge of the carbon ions guarantee a low scattering component along the beam path. The same detector mode configuration as in the experiments (Time, ToT, Time, Time mode) was used.
Table 6.5 also shows that greater misalignment occurred between the first detector and the others. Smaller shifts were measured between the detectors in the stack. In general within this work, shifts below 10 pixels (∼0.06 cm) were measured with respect to Detector 1, and below 4 pixels (∼0.02 cm) between the detectors in the stack.

6.2 Fragmentation of Carbon Ions in Water and in PMMA

Water and PMMA targets, which have in pairs the same water equivalent thickness (see Table 6.1), were irradiated with a 430 MeV/u carbon ion beam. In Section 5.1 the experimental setup and parameters used are presented in detail. The distribution of the different outgoing ions behind the targets and their lateral distributions were investigated and compared for coupled targets. The experimental results were also compared with simulations performed using the FLUKA code.

6.2.1 Investigation of the ion spectra

The different particle species registered behind the targets were quantified using the 2D distributions of the measured clusters in variables of cluster signal and cluster size, as described in Section 5.4.2. An example of 2D scatter plot and of the regions used to distinguish between particle species is provided in Figure 6.29. In the following, $N_{particles}$ denotes the number of particles (H, He, Li, Be, B or C, as specified) detected behind the targets, while N_0 is the number of incoming primary carbon ions. All results were normalized to N_0.

Carbon ions detected behind the targets

Figure 6.1 shows the number of carbon ions registered behind the water and the PMMA targets, as a function of the WET. The experimental results and the simulations are compared. The number of detected particles decreases with increasing target thickness. Indeed, due to the higher amount of material along the particle paths, more fragmentation and scattering processes occur within ticker targets.

The experimental data for the water and the PMMA targets are in good agreement within their statistical uncertainties. Small differences (<1%) were observed only between the two thinnest targets.

The carbon ion attenuation curves obtained in the experiments and in FLUKA have different slopes. More particles were found in the simulations behind thin targets, and less particles behind thick targets. Within the range of investigated target thicknesses, the greatest differences (∼ 6%) between measurements and simulations were found between the thinnest targets (Water and PMMA 5 cm_{WET} thick).

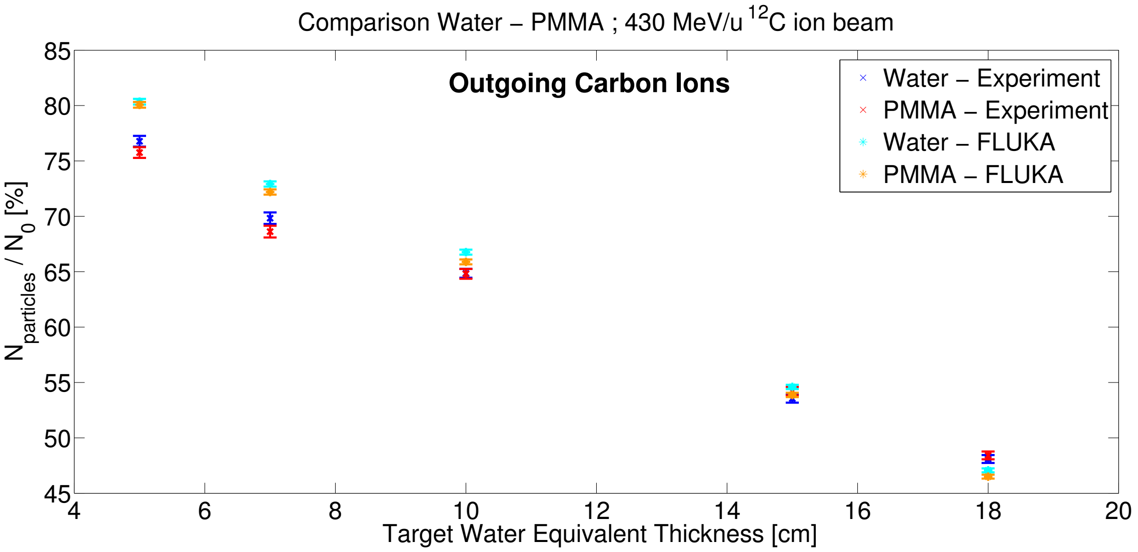

Figure 6.1: Number of carbon ions detected behind water and PMMA targets with the same WET, irradiated with a 430 MeV/u carbon ion beam. The experimental results are compared with those obtained by FLUKA Monte Carlo simulations. The data are normalized to the number of primary carbon ions.

Fragments detected behind the targets

The secondary fragments produced in the targets were also investigated, and the number of particles detected are shown in Figure 6.2, Figure 6.3, Figure 6.4 and Figure 6.5, for H, He, Li and Be respectively. The results for boron are not shown, as the identification of this particle type could not be performed accurately (see Section 6.5.3).

For all fragment species, both behind the water and the PMMA targets, and both in the measurements and in the simulations, a similar trend of the number of detected particles as a function of the target thickness was observed: a build-up to a certain target thickness and a subsequent decrease. The final decrease could be due to fragmentation processes occurring at the beginning of thick phantom, and therefore at greater distances to the detectors behind the targets. As the solid angle subtended by the detectors became smaller with increasing distance to them, the probability that fragments produced at the beginning of thick targets travel out of the detection area is higher. Moreover, those particles may undergo scattering or further fragmentation along the target. Scattering is in general more relevant with decreasing particle mass. Further fragmentations would instead influence the amount of detected heavy fragments more, as a higher amount of heavy particles would be lost in favour of lighter ones. The observed shifts in the maximum positions to greater target thicknesses with increasing particle mass (Figure 6.2, Figure 6.3, Figure 6.4 and Figure 6.5) are hence in agreement with the expectations. Those shifts were found to be similar in measurements with the water and the PMMA targets, both in the experiments and in the simulations.

Less secondary fragments were registered behind the water than the PMMA targets, both in the experiments and in the simulations. In the experimental data, the greatest differences (1-2%) between the water and the PMMA targets were found in the case of light fragments (H, He). Those differences correspond to relative differences of about 20% due to the low amount of detected particles. In the simulations, more fragments were detected behind all targets. Also in this case the greatest differences with respect to the experimental data were observed in the amount of light particles registered (absolute differences ∼3%, which correspond to relative differences of about 30%).

The heavier elements present in PMMA ($C_5O_2H_8$) than in water may cause more fragmentation processes within the target, or may lead to a higher production of light fragments. To gain a deeper understanding of the fragmentation processes, type and number of fragments detected from each single primary carbon ion were investigated and the results are shown in the next paragraph. Different lateral particle distributions behind the targets can also influence the amount of particles detected. The lateral particle distributions are analysed in Section 6.2.2.

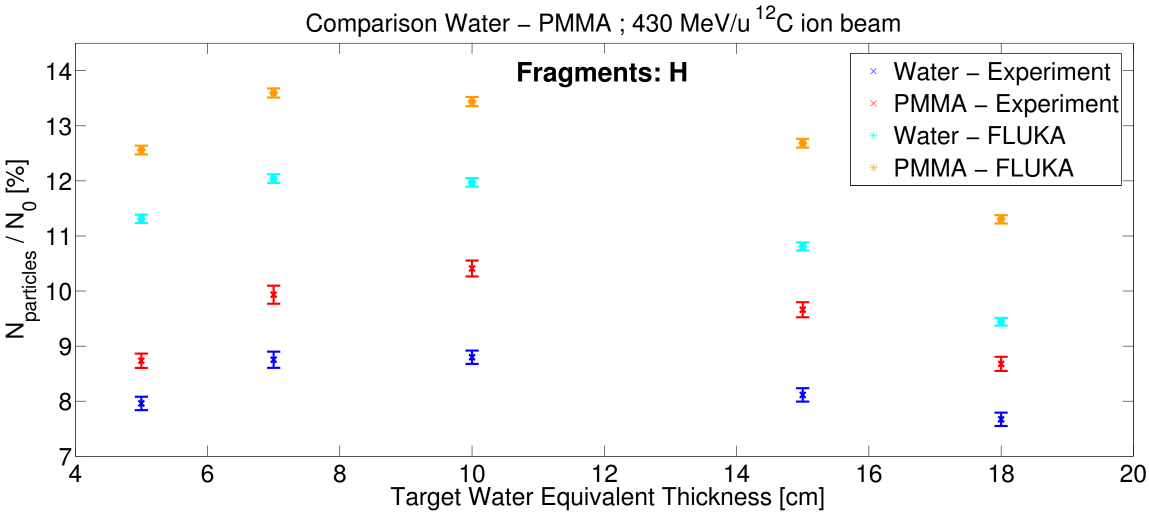

Figure 6.2: Number of secondary H detected behind water and PMMA targets with the same WET, irradiated with a 430 MeV/u carbon ion beam. The experimental results are compared with those obtained by FLUKA Monte Carlo simulations. The data are normalized to the number of primary carbon ions.

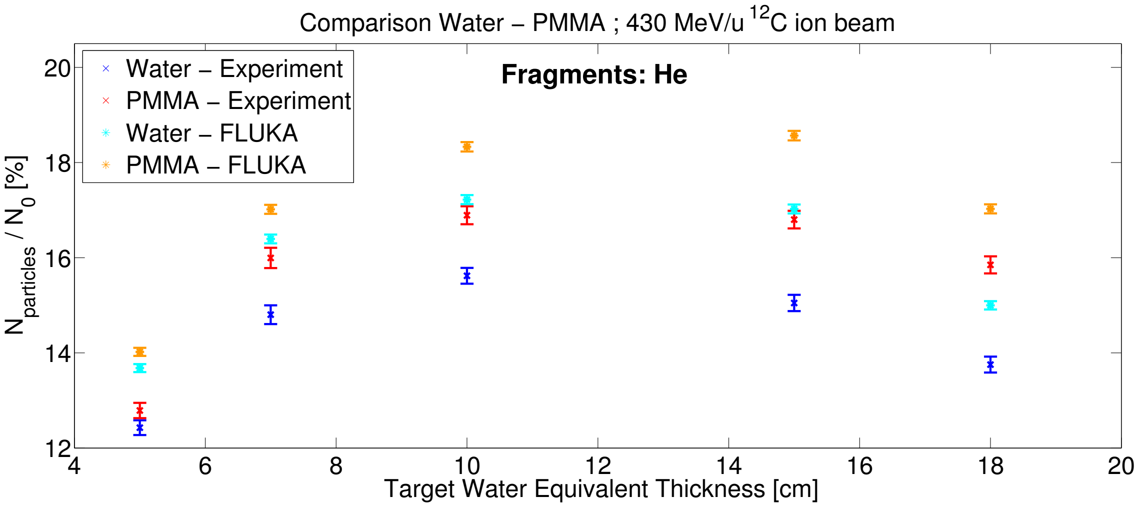

Figure 6.3: Number of secondary He detected behind water and PMMA targets with the same WET, irradiated with a 430 MeV/u carbon ion beam. The experimental results are compared with those obtained by FLUKA Monte Carlo simulations. The data are normalized to the number of primary carbon ions.

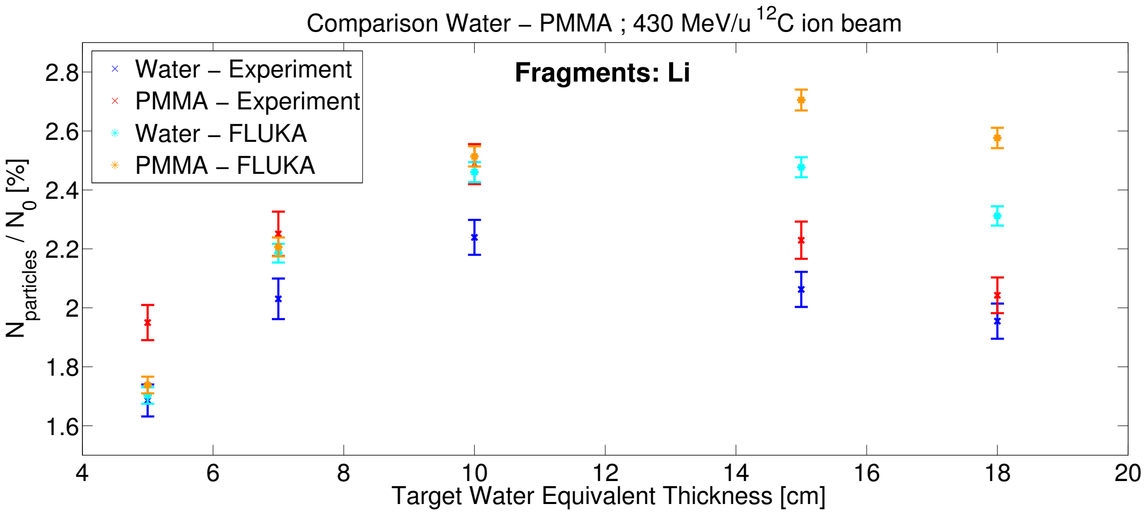

Figure 6.4: Number of secondary Li detected behind water and PMMA targets with the same WET, irradiated with a 430 MeV/u carbon ion beam. The experimental results are compared with those obtained by FLUKA Monte Carlo simulations. The data are normalized to the number of primary carbon ions.

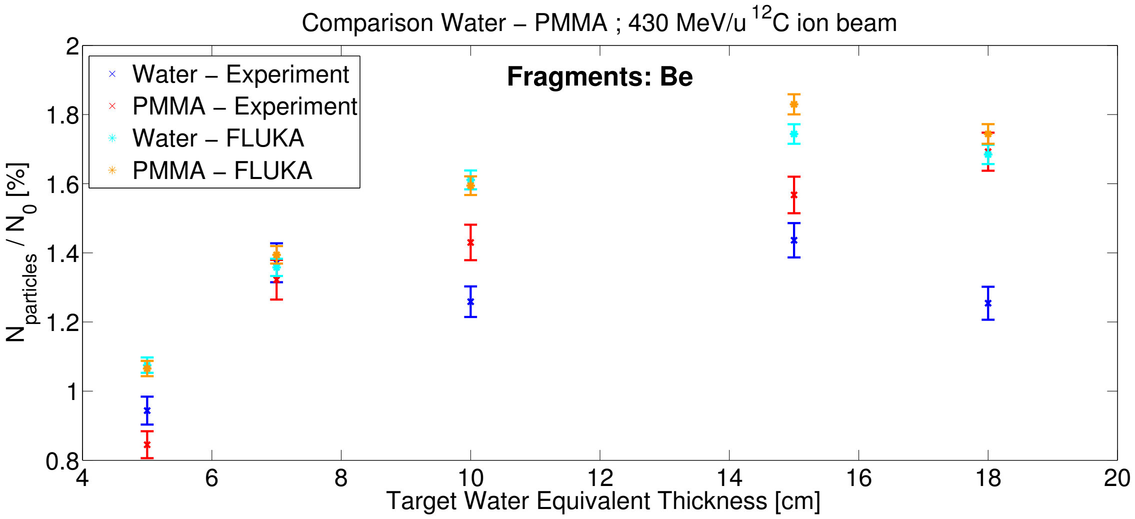

Figure 6.5: Number of secondary Be detected behind water and PMMA targets with the same WET, irradiated with a 430 MeV/u carbon ion beam. The experimental results are compared with those obtained by FLUKA Monte Carlo simulations. The data are normalized to the number of primary carbon ions.

Types and multiplicity of fragments detected from a single primary ion
In the results from FLUKA, the number of secondary fragments detected were always greater than in the measurements, although the number of carbon ions registered behind the thin phantoms was also higher in the simulations. To better understand these results, the amount of fragments registered from a single primary ion was analysed and compared between simulations and experiments. This analysis could be performed exploiting the information provided by the time coincidence measurements. The probabilities of detecting a given number of fragments from each primary ion are shown in Figure 6.6, for three target thicknesses (5 $\mathrm{cm_{WET}}$, 10 $\mathrm{cm_{WET}}$ and 18 $\mathrm{cm_{WET}}$).
The probability of detecting one or multiple fragments from a single primary particle was higher behind the PMMA than the water targets. The differences between the two materials increase for thicker targets, where the differences in the chemical compositions have a greater influence.
The probability of detecting multiple fragments was found to be higher in FLUKA than in the experiments, whereas the probability of not finding any matching particle behind the target was higher in the measurements. Furthermore, different trends were observed between the experiments and the simulations, as described in the following:

- in the experimental data, a monotonic decrease in probability as a function of the number of fragments registered from a single primary ion was observed in all cases;
- in the simulations, for water and PMMA targets 5 $\mathrm{cm_{WET}}$ thick, a maximum of probability at two fragments was found (Figure 6.6, top);
- in the simulations, for water and PMMA targets 10 $\mathrm{cm_{WET}}$ thick, an initial plateau followed by a drop in probability was observed (Figure 6.6, middle);
- in the simulations, for water and PMMA targets 18 $\mathrm{cm_{WET}}$ thick, a monotonic decrease, similar to the experimental one, was found (Figure 6.6, bottom).

These differences lead to the greater amount of fragments detected in FLUKA, despite the lower loss of primary particles observed for the thin targets (see Figure 6.1).

To gain more information, the various combinations of fragments detected from a single primary carbon ion were analysed. The probabilities of registering those combinations were evaluated and compared between experimental and simulated data. Figure 6.7 shows the results only for the most probable combinations, and for the two extreme target thicknesses (5 $\mathrm{cm_{WET}}$ and 18 $\mathrm{cm_{WET}}$), as examples.
The experimental results obtained with water and PMMA targets with the same WET are in general consistent within their uncertainties. The comparison between the experiments and the simulations shows that the probabilities of registering a given combination of fragments were always higher in FLUKA, except for He+He detected from a single carbon ion behind targets 5 $\mathrm{cm_{WET}}$ thick (Figure 6.7, top). In general, differences $\leqslant$1% were measured in each combination of fragments, in the case of targets 5 $\mathrm{cm_{WET}}$ thick. The differences increase, up to 2.5%, for targets 18 $\mathrm{cm_{WET}}$ thick (Figure 6.7, bottom).

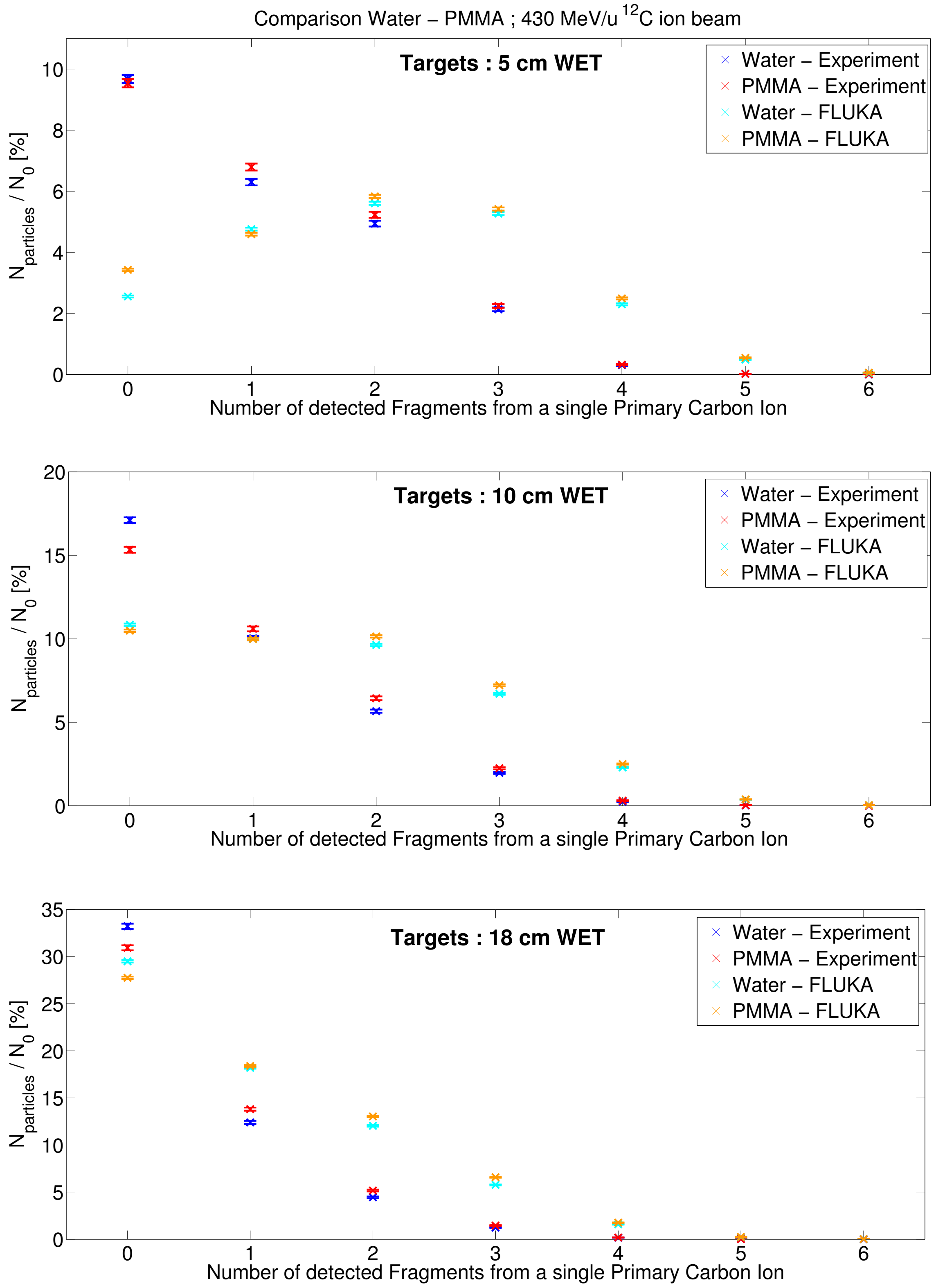

Figure 6.6: Probability of detecting between 0 and 6 fragments from a single primary particle. The results were obtained behind water and PMMA targets 5 cmWET (*top*), 10 cmWET (*middle*) and 18 cmWET (*bottom*) thick, irradiated with a 430 MeV/u carbon ion beam.

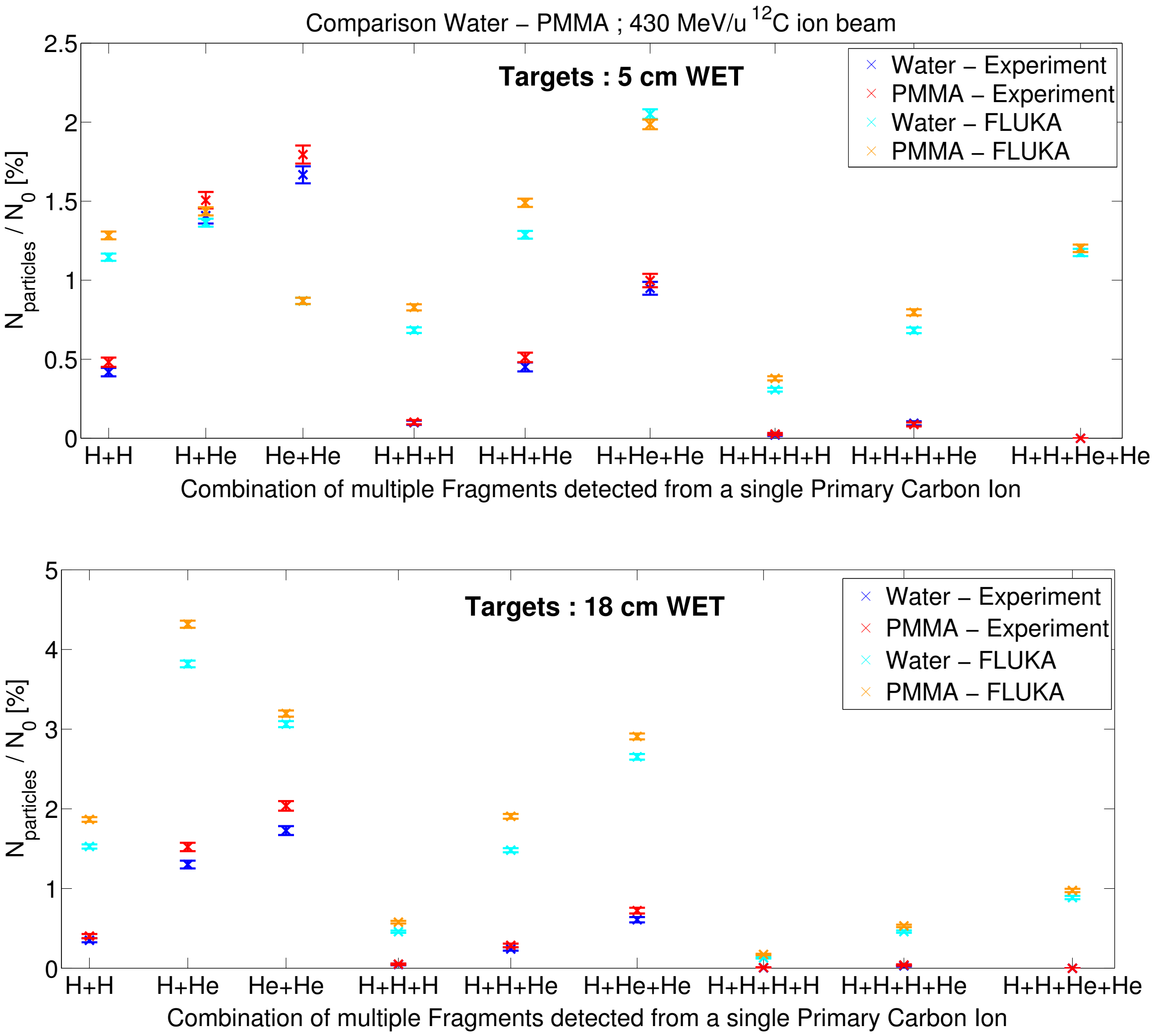

Figure 6.7: Probability of detecting certain combinations of secondary fragments from a given primary ion. The results were obtained with water and PMMA targets 5 cmWET thick (*top*), or with water and PMMA targets 18 cmWET thick (*bottom*), irradiated with a 430 MeV/u carbon ion beam.

All the combinations shown in Figure 6.7 involve only H and He, as the greatest differences were found in those cases. The probabilities of recording combinations of particles including at least one heavy fragment were always smaller than 0.5%, and in general good agreement was found between measurements and simulations. Those data are available upon request.

6.2.2 Analysis of the lateral particle distributions

The lateral distributions of the primary and secondary particles detected behind the targets were investigated in terms of their lateral distances to the primary particle positions in the first detector, as illustrated in Figure 5.7. Due to experimental limits, distances $\leqslant$0.35 cm were considered (see Section 5.4 for more details). The particles were gathered in three groups: carbon ions, secondary H+He, secondary Li+Be+B.

Carbon ions detected behind the targets
The results for carbon ions are shown in Figure 6.8, for three target thicknesses (5 cmWET, 10 cmWET and 18 cmWET) as examples. In general, the percentage of registered particles decreases as a function of the lateral distance to the primary particle position. Broader distance distributions were found for thicker targets, where the cumulative scattering effect is greater, due to the higher amount of material. The comparison between the water and the PMMA targets shows similar results for the experiments, whereas sharper lateral particle distributions were observed in FLUKA, especially in case of thin targets. A further analysis of the distance distributions, by means of the d_{mean} and $d_{max(80\%)}$ quantities, is presented later in this section.

Fragments detected behind the targets
The distributions of H+He and Li+Be+B as a function of the lateral distance to the corresponding primary carbon ion position were also investigated. Figure 6.9 and Figure 6.10 show the results obtained with the thickest phantoms (18 cmWET), behind which the broadest lateral distributions were observed. As expected, the distance distributions of H+He were broader then those of Li+Be+B, due to the smaller masses. Similar results were obtained for all target thicknesses, with distance distributions which became more forward peaked behind thinner targets.

Comparison of the mean lateral distances
The mean lateral distances, d_{mean}, between 0 cm and 0.35 cm, were determined for all targets and each particle species.
As Figure 6.11 shows, the values calculated for the carbon ions, d^C_{mean}, are higher behind thicker targets, as expected. Moreover, greater d^C_{mean} values were found behind the water than the PMMA targets and the differences increase with increasing target thickness (up to 9%). That is probably due to the larger geometrical thicknesses of the water phantoms than the corresponding PMMA targets with the same WET (see Table 6.1).
Also in FLUKA, the d^C_{mean} were higher behind the water than the PMMA targets and the differences increase for thicker targets. However, smaller d^C_{mean} values were determined in the simulations than in the experiments: differences of about 20% occurred in the case of the thinnest targets, and of about 8% in the case of the thickest ones.

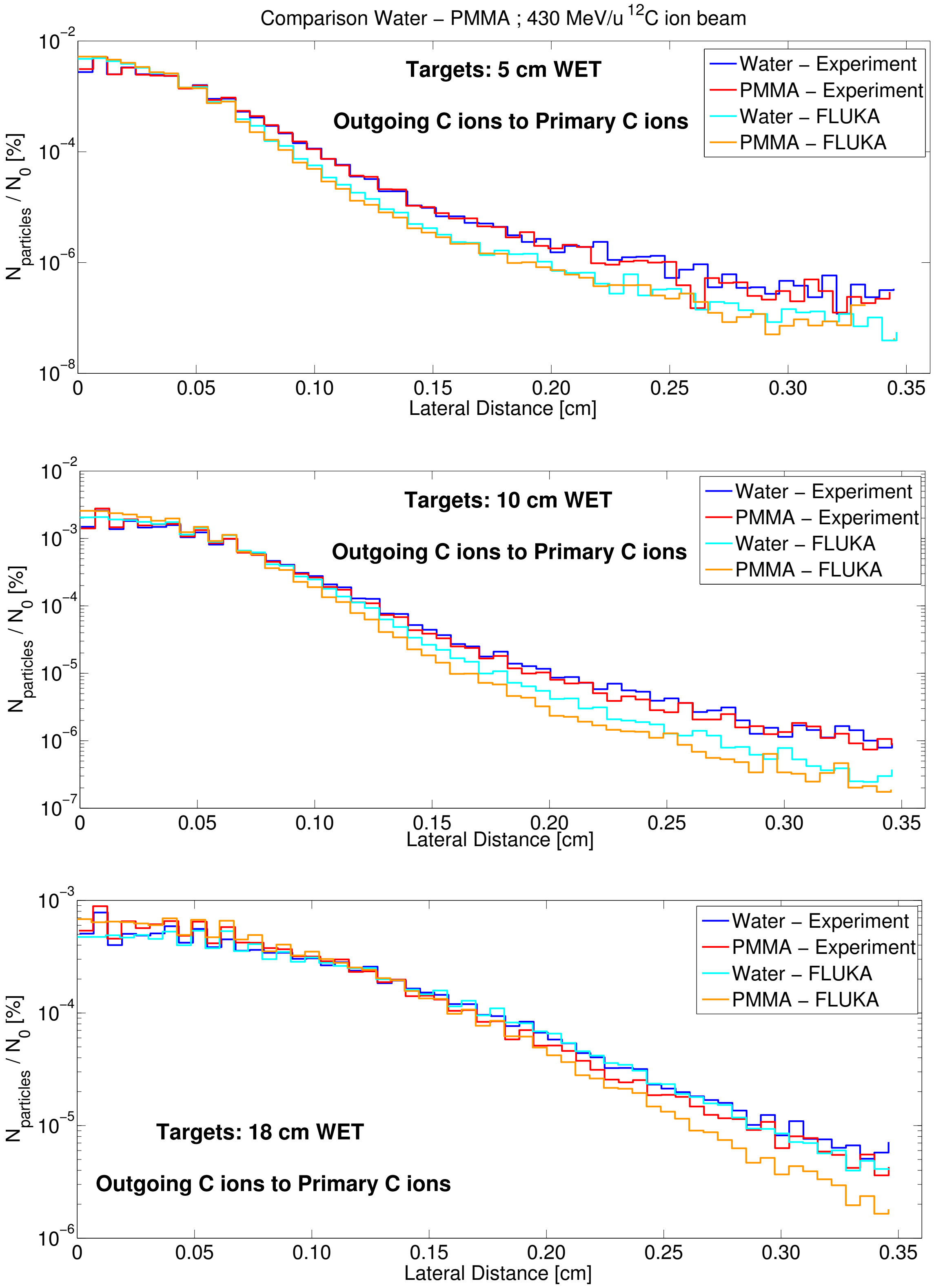

Figure 6.8: Distribution of carbon ions registered in the second detector as a function of the lateral distance to the corresponding incoming carbon ion position in the first detector. The results were obtained with water and PMMA targets 5 cmWET (*top*), 10 cmWET (*middle*) and 18 cmWET (*bottom*) thick irradiated with a 430 MeV/u carbon ion beam.

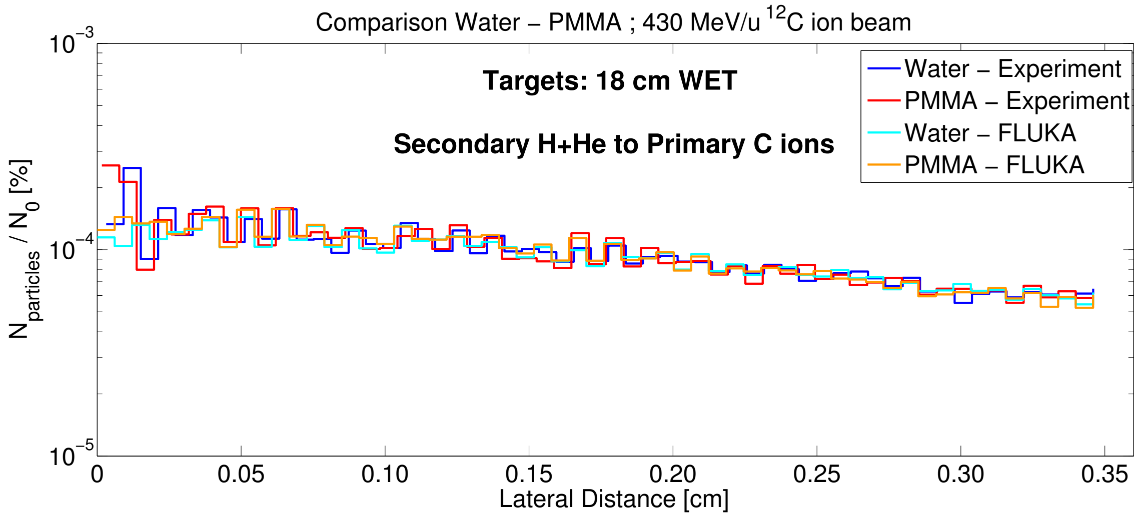

Figure 6.9: Distribution of H+He registered in the second detector as a function of the lateral distance to the corresponding incoming carbon ion position in the first detector. The results were obtained with water and PMMA targets 18 cmWET thick irradiated with a 430 MeV/u carbon ion beam.

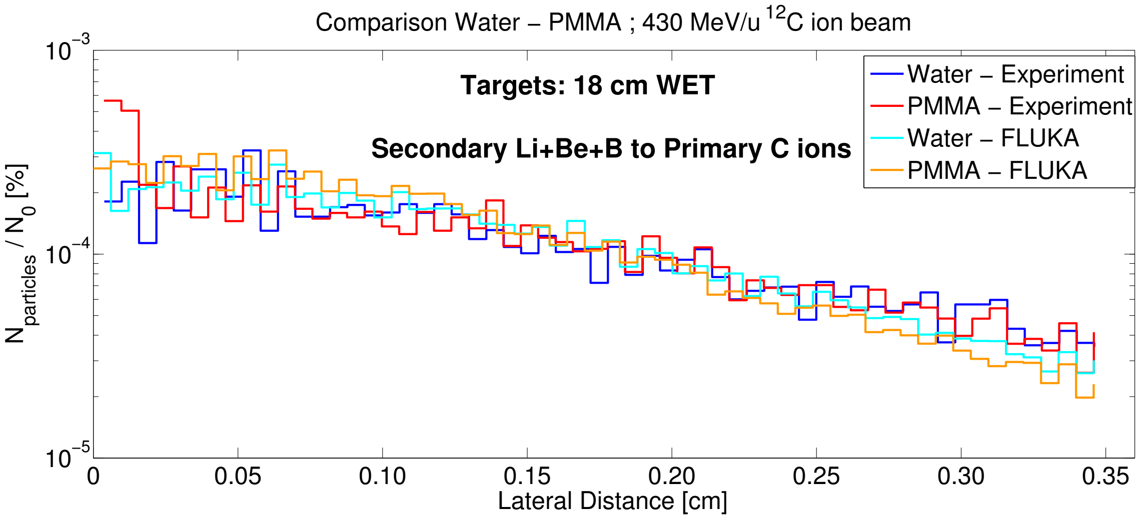

Figure 6.10: Distribution of Li+Be+B registered in the second detector as a function of the lateral distance to the corresponding incoming carbon ion position in the first detector. The results were obtained with water and PMMA targets 18 cmWET thick irradiated with a 430 MeV/u carbon ion beam.

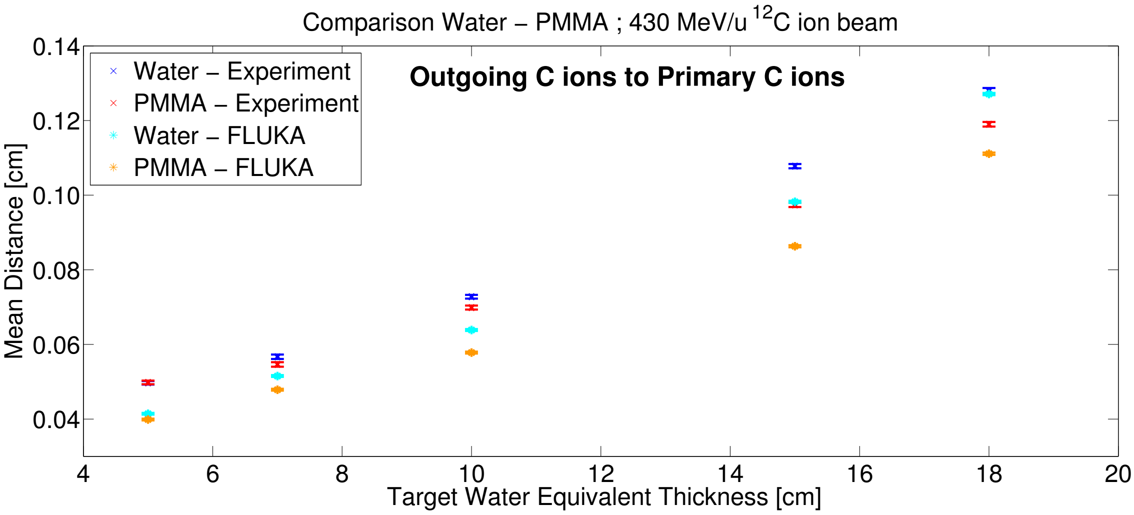

Figure 6.11: Mean lateral distances between the carbon ion positions registered in the second detector and the corresponding incoming primary carbon ion positions in the first detector. The water and the PMMA targets were irradiated with a 430 MeV/u incoming carbon ion beam.

The mean lateral distances between the position of Li+Be+B in the second detector and the corresponding primary particle position in the first detector are shown in Figure 6.12 for all targets. In the experiments, the $d_{mean}^{Li+Be+B}$ values are in agreement within their uncertainties or differ by less than 3%. In the simulations, lower values were obtained than in the experiments, and $d_{mean}^{Li+Be+B}$ was always smaller for the PMMA target than the corresponding water targets. With respect to the experimental data, the differences are between 22% and 28%, depending on the target thickness and material.
As regards the outgoing light fragments (H+He), a better agreement was observed in the mean lateral distances, d_{mean}^{H+He}, determined behind the water and the PMMA targets, and between the experiments and the simulations, than in the case of the heavy fragments. As it can be seen in Figure 6.13, the greatest differences were found in the thinnest targets between the experiments and the simulations, and they are about 4%.

For comparison, the d_{mean} values for the different particle species and target thicknesses are listed in Table 6.6. The results are shown only for three target thicknesses and for the experimental data, as examples. The other data are available upon request.

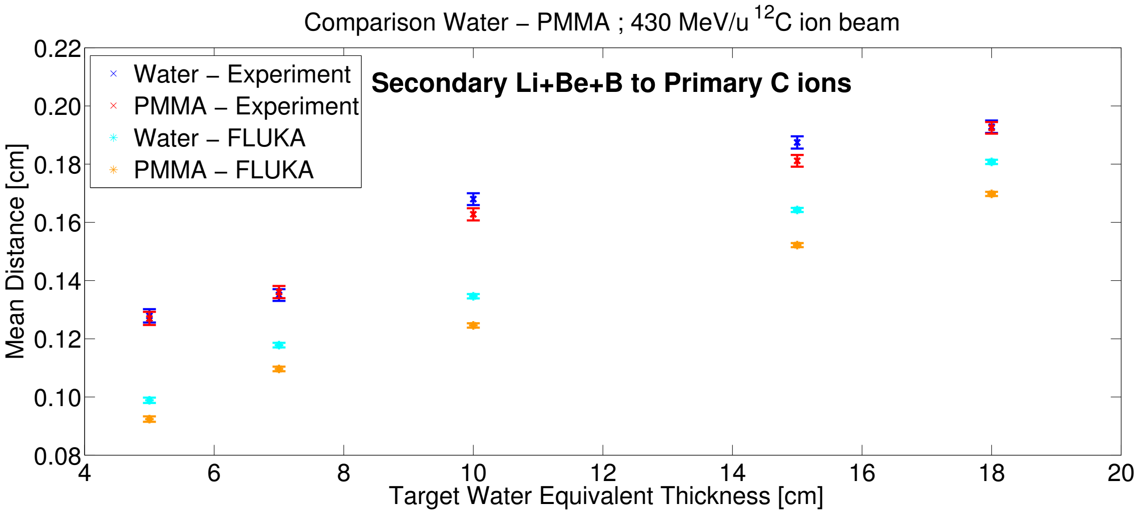

Figure 6.12: Mean lateral distances between the positions of Li+Be+B registered in the second detector and the corresponding incoming carbon ion positions in the first detector. The water and the PMMA targets were irradiated with a 430 MeV/u carbon ion beam.

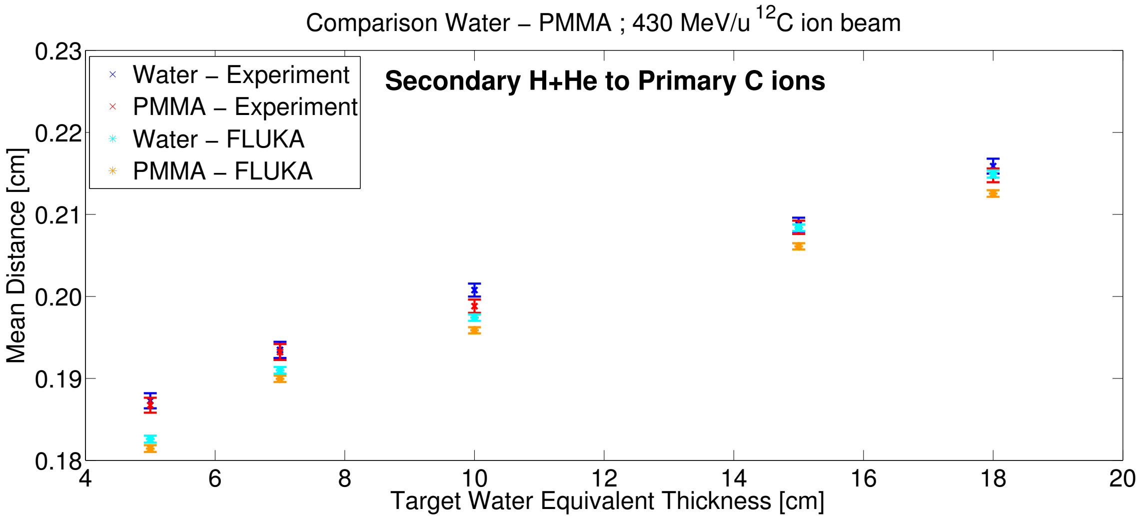

Figure 6.13: Mean lateral distances between the positions of H+He registered in the second detector and the corresponding incoming carbon ion positions in the first detector. The water and the PMMA targets were irradiated with a a 430 MeV/u carbon ion beam.

Table 6.6: Mean lateral distances of different particle species registered in the second detector with respect to the corresponding incoming carbon ion positions in the first detector. The results are shown for three target thicknesses (5 $\mathrm{cm_{WET}}$, 10 $\mathrm{cm_{WET}}$ and 18 $\mathrm{cm_{WET}}$). Measurements were performed with a 430 MeV/u carbon ion beam.

	d^{C}_{mean} (10^{-3} cm)	d^{H+He}_{mean} (10^{-3} cm)	$d^{Li+Be+B}_{mean}$ (10^{-3} cm)
Water 5	49.7 ± 0.5	187.3 ± 0.9	128 ± 2
PMMA 5	49.8 ± 0.5	186.7 ± 0.9	127 ± 2
Water 10	72.8 ± 0.5	200.8 ± 0.8	168 ± 2
PMMA 10	69.9 ± 0.5	198.8 ± 0.8	163 ± 2
Water 18	128.0 ± 0.7	215.9 ± 0.9	193 ± 2
PMMA 18	119.0 ± 0.6	214.8 ± 0.8	193 ± 2

The most relevant findings achievable from Table 6.6 are that:

- $d^{H+He}_{mean} > d^{Li+Be+B}_{mean} > d^{C}_{mean}$, for all targets
- the ratios (d^{H+He}_{mean} / d^{C}_{mean}) and ($d^{Li+Be+B}_{mean}$ / d^{C}_{mean}) decrease with increasing target thickness

The first result was expected, as the lateral particle distributions are in general broader for lighter particles. On the other hand, the second finding is not in accordance with the expectations. Indeed, due to the higher amount of material, the lateral particle distributions both of the carbon ions and of the fragments is broader behind thicker targets. This is in agreement with the results previously shown. However, as fragments have lower masses and charges than the carbon ions, scattering in the phantom should influence the lateral distributions of the fragments more strongly than the primary beam particles. Hence, an increase in the ratio values was expected with increasing target thickness. The opposite trend observed here could be explained by considering that the carbon ions detected behind the phantoms traveled through the whole target; instead, fragments crossed the phantom only between the nuclear interaction point and the end of the target. Moreover, in the previous section, a decrease in the number of detected fragments was observed beyond a certain target thickness (see Figure 6.2, Figure 6.3, Figure 6.4 and Figure 6.5). The fragments lost are expected to be mainly those produced at the beginning of the phantoms, as their probability to travel out of the area covered by the detectors behind the targets or to undergo further fragmentation within the target is higher. According to this theory, in the case of thick targets, the detected carbon ions in the second detector experienced multiple coulomb scattering through the whole phantom, whereas the fragments detected were produced sufficiently close to the end of the phantom or with sufficiently small angles with respect to the beam axis. Therefore the observed decrease in the ratio values of (d^{H+He}_{mean} / d^{C}_{mean}) and ($d^{Li+Be+B}_{mean}$ / d^{C}_{mean}) with increasing target thickness may just be an artifact, due to the geometrical limits of the detection area.

Comparison between d_{mean} and $d_{max(80\%)}$

The maximum distances achieved by 80% of the particles were also calculated for each particle species and target thickness. These quantitiesm compared with the d_{mean} values, can be used for a qualitative estimation of the width of the lateral particle distributions: the greater d_{mean} is with respect to $d_{max(80\%)}$ the sharper the lateral particle distribution is, and vice versa. A comparison between $d_{max(80\%)}$ and the respective d_{mean} can be found in Table 6.7, for three target thicknesses and for the experimental data. The greater value between d_{mean} and $d_{max(80\%)}$ is highlighted for each target and a short summary is provided at the bottom of the table. The uncertainties of $d_{max(80\%)}$ were determined as described in Section 5.4.3.

For all target thicknesses, d^{C}_{mean} was found to be always greater than $d^{C}_{max(80\%)}$, whereas d^{H+He}_{mean} was always smaller than $d^{H+He}_{max(80\%)}$. $d^{Li+Be+B}_{mean}$ was greater than $d^{Li+Be+B}_{max(80\%)}$ only for thin targets and became smaller for the thickest targets.

Table 6.7: Comparison between the d_{mean} and $d_{max(80\%)}$ values, calculated for different particle species and three target thicknesses (5 cmWET, 10 cmWETand 18 cmWET). Measurements were performed with a 430 MeV/u carbon ion beam.

	d^{C}_{mean} (10^{-3} cm)	$d^{C}_{max(80\%)}$ (10^{-3} cm)	d^{H+He}_{mean} (10^{-3} cm)	$d^{H+He}_{max(80\%)}$ (10^{-3} cm)	$d^{Li+Be+B}_{mean}$ (10^{-3} cm)	$d^{Li+Be+B}_{max(80\%)}$ (10^{-3} cm)
Water 5	**49.7±0.5**	43.4±1.7	187.3±0.9	**192.0±1.7**	**128±2**	81.0±1.7
PMMA 5	**49.8±0.5**	43.4±1.7	186.7±0.9	**186.7±1.7**	**127±2**	82.2±1.7
Water 10	**72.8±0.5**	64.1±1.7	200.8±0.8	**217.0±1.7**	**168±2**	150.0±1.7
PMMA 10	**69.9±0.5**	59.0±1.7	198.8±0.8	**212.2±1.7**	**163±2**	145.6±1.7
Water 18	**128.0±0.7**	120.5±1.7	215.9±0.9	**243.3±1.7**	193±2	**198.1±1.7**
PMMA 18	**119.0±0.6**	110.2±1.7	214.8±0.8	**237.7±1.7**	193±2	**196.8±1.7**
Summary	$d^{C}_{mean} > d^{C}_{max(80\%)}$		$d^{H+He}_{mean} < d^{H+He}_{max(80\%)}$		Thickness Dependency	

For the carbon ions, the d^C_{mean} and $d^C_{max(80\%)}$ values were compared between the experimental data and the simulations. The results are listed in Table 6.8 for three target thicknesses (5 cmWET, 10 cmWETand 18 cmWET). Significant differences were found between the experiments and the simulations, especially for the thick targets. In case of d^C_{mean}, the differences are between 8% and 13%, whereas the uncertainties associated to d^C_{mean} are below 1%. The differences become smaller, between 1.3% and 8%, for $d_{max(80\%)}$, whose experimental uncertainties are <4%. In all cases, the values obtained in the experiments are greater than those obtained from the FLUKA simulations.

Table 6.8: Comparison between the d^C_{mean} and $d^C_{max(80\%)}$ values calculated for three target thicknesses (5 cmWET, 10 cmWETand 18 cmWET). The results are compared between experimental data and simulations. Measurements were performed with a 430 MeV/u carbon ion beam. $d^C_{Experiment}$ and d^C_{FLUKA} refer to both d^C_{mean} and $d^C_{max(80\%)}$ calculated in the experiments and in FLUKA, respectively.

	Experiment		FLUKA	
	d^C_{mean} (10^{-3} cm)	$d^C_{max(80\%)}$ (10^{-3} cm)	d^C_{mean} (10^{-3} cm)	$d^C_{max(80\%)}$ (10^{-3} cm)
Water 5	49.7±0.5	43.4±1.7	41.4±0.2	38.0±1.7
PMMA 5	49.8±0.5	43.4±1.7	39.9±0.2	38.1±1.7
Water 10	72.8±0.5	64.1±1.7	63.9±0.3	63.7±1.7
PMMA 10	69.9±0.5	59.0±1.7	57.8±0.3	58.6±1.7
Water 18	128.0±0.7	120.5±1.7	127.1±0.3	124.9±1.7
PMMA 18	119.0±0.6	110.2±1.7	111.1±0.3	109.6±1.7
Summary	$d^C_{Experiment} \geqslant d^C_{FLUKA}$			

6.3 Fragmentation of Helium Ions in Water and in PMMA

For this investigation, a 221 MeV/u helium ion beam was used to irradiate the water and the PMMA targets, which in pair have the same WET (see Table 6.1). The distributions of the outgoing particles behind the targets were compared for the two materials. A detailed description of the experimental apparatus is available in Section 5.1. Monte Carlo simulations of the experiments were performed with the FLUKA code.

6.3.1 Investigation of the ion spectra

Quantification of the particle species registered behind the targets was carried out using the 2D distributions of the measured clusters in variables of cluster signal and cluster size, as described in Section 5.4.2. An example of a 2D scatter plot and of the regions used to identify the particle species is shown in Figure 6.30. In the following, $N_{particles}$ denotes the number of particles (H or He as specified) detected behind the targets, while N_0 is the number of incoming primary helium ions. All results were normalized to N_0.

Helium ions detected behind the targets

The amount of helium ions registered behind the investigated targets was analysed. Figure 6.14 shows the resulting attenuation curves obtained with the water and the PMMA targets, in the experiments and in the simulations.

The experimental results for coupled targets are consistent within their uncertainties, except for the thickest targets where less helium ions (-2%) were measured behind the water than the PMMA target. For the thickest targets, the absolute difference in the geometrical thickness is also the greatest, as shown in Table 6.1.

More He ions were registered behind all targets in FLUKA. The attenuation curves obtained from the water phantoms in the experiments and in the simulations are rather parallel; for the PMMA phantoms, however, the slope is less steep in the experiments. The differences are between 3% and 8% depending on the target thickness and material: they are greater for thicker targets and in the case of PMMA phantoms.

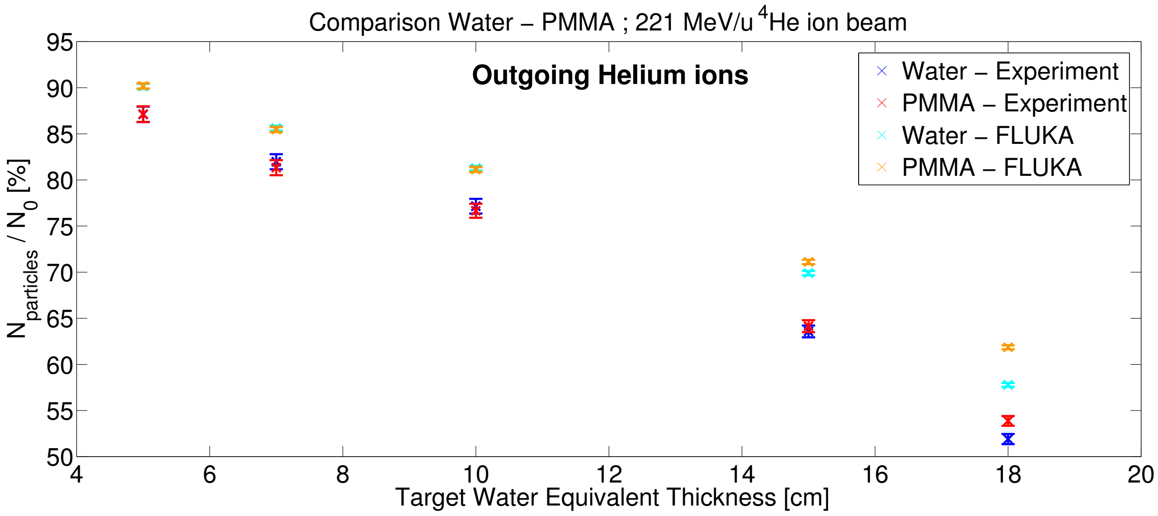

Figure 6.14: Number of helium ions detected behind water and PMMA targets with the same WET, irradiated with a 221 MeV/u helium ion beam. The experimental results are compared with those obtained by FLUKA Monte Carlo simulations. The data are normalized to the number of primary helium ions.

H detected behind the targets

Figure 6.15 shows the number of secondary H detected behind the phantoms. Due to the low abundance of registered particles, the statistical uncertainties are ~10%.
Like the measurements with carbon ion beams (Study 1, Figure 6.2), the number of secondary H detected increases to a certain WET and then decreases. The position of the maximum is also similar in the two cases, despite the different primary particle species. As already discussed in Section 6.2.1, in *Fragments detected behind the targets*, it is possible that the final drop is due to the higher probability that fragments produced at greater distances to the detectors behind the phantoms travel out of the area covered by those detectors.
In general, more fragments were detected behind the PMMA targets, both in the experiments and in the simulations. The absolute differences between the experimental results are $\leqslant$0.5%, which, due to the low abundance of registered particles, correspond to relative differences between 8% and 13%. The differences in the chemical compositions between PMMA ($C_5O_2H_8$) and water, and in the geometrical thickness between coupled target may influence the interaction cross sections and the lateral particle distributions, and therefore cause the observed differences in the results.
Contrary to the measurements with carbon ions, a lower amount of secondary H were found in FLUKA. This result is consistent with the higher amount of He detected behind the targets in the simulations. The differences between experimental and simulated data are <0.5%.

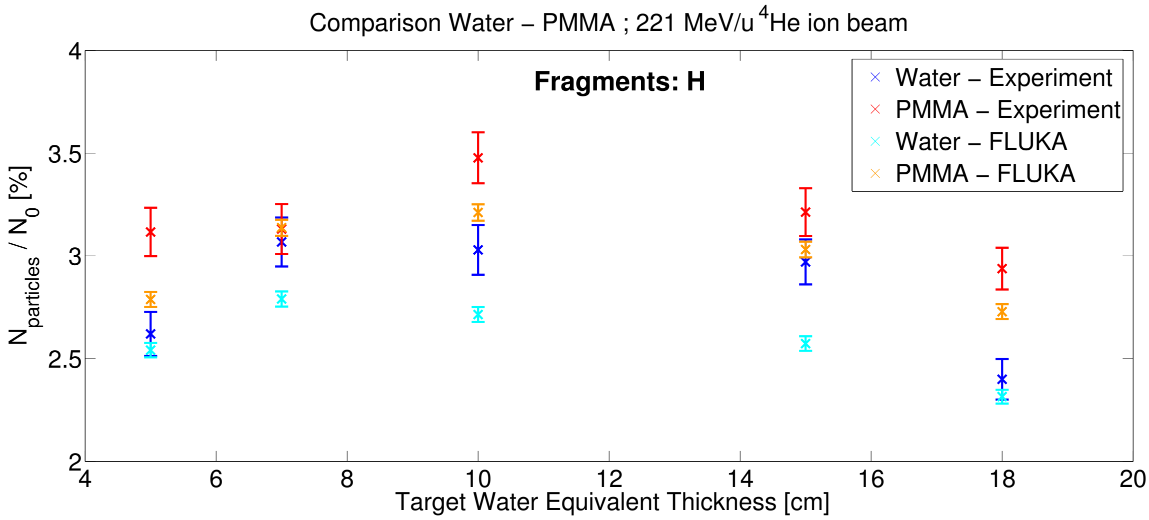

Figure 6.15: Number of secondary H detected behind water and PMMA targets with the same WET, irradiated with a 221 MeV/u helium ion beam. The experimental results are compared with those obtained by FLUKA Monte Carlo simulations. The data are normalized to the number of primary helium ions.

6.3.2 Analysis of the lateral particle distributions

To investigate the lateral particle distributions, the lateral distances between the positions of the particles registered behind the targets and the corresponding primary particle positions in the first detector were determined, as illustrated in Figure 5.7. Only particles with distances $\leqslant$0.35 cm were considered, as discussed in Section 5.4.

Helium ions detected behind the targets

The lateral distance distributions of the helium ions are shown in Figure 6.16 for the thinnest and the thickest targets.

The amount of detected particles decreases with increasing distances. Hence, as expected, the helium ions were mainly scattered at relatively small angles. However, the distance distributions became broader behind thicker targets, as the cumulative effect of particle scattering increased. In general, similar profiles were found for coupled targets in the experimental data.

Sharper distributions were observed in the simulations than in the experiments.

For a quantitative analysis of the results, the d_{mean} and $d_{max(80\%)}$ values were determined and they are analysed later in this section.

H detected behind the targets

The distributions of H as a function of the lateral distance to the corresponding primary helium ion position in the first detector were analysed. An example is shown in Figure 6.17, for the thickest water and PMMA targets (18 cm$_{\text{WET}}$ thick). As expected, the distance distribution of the secondary H was broader then those of the outgoing He ions (see Figure 6.16, bottom). With decreasing target thickness, the distance distributions of H became more forward peaked.

Comparison of the mean lateral distances

The mean lateral distances, d_{mean}, were determined between 0 cm and 0.35 cm, for all targets, and for both the outgoing He and the outgoing H.

As shown in Figure 6.18, the d^{He}_{mean} values increase with increasing target thickness, as a result of the broader lateral particle distributions behind thicker targets. The experimental values measured for the water and the PMMA phantoms were found to be consistent only for the thinnest targets. The differences increase up to 7% for the thickest water and PMMA targets.

On the contrary, an improving agreement was found between the experiments and the simulations with increasing target thickness. The greatest differences (23%) were indeed measured in the case of targets 5 cm$_{\text{WET}}$ thick. Moreover, for all thicknesses, the differences between the experiments and the simulations were higher between the PMMA than the water phantoms.

Figure 6.19 shows the mean lateral distances obtained for the secondary H, d^{H}_{mean}. The results were found to be in agreement within their uncertainties, both between the water

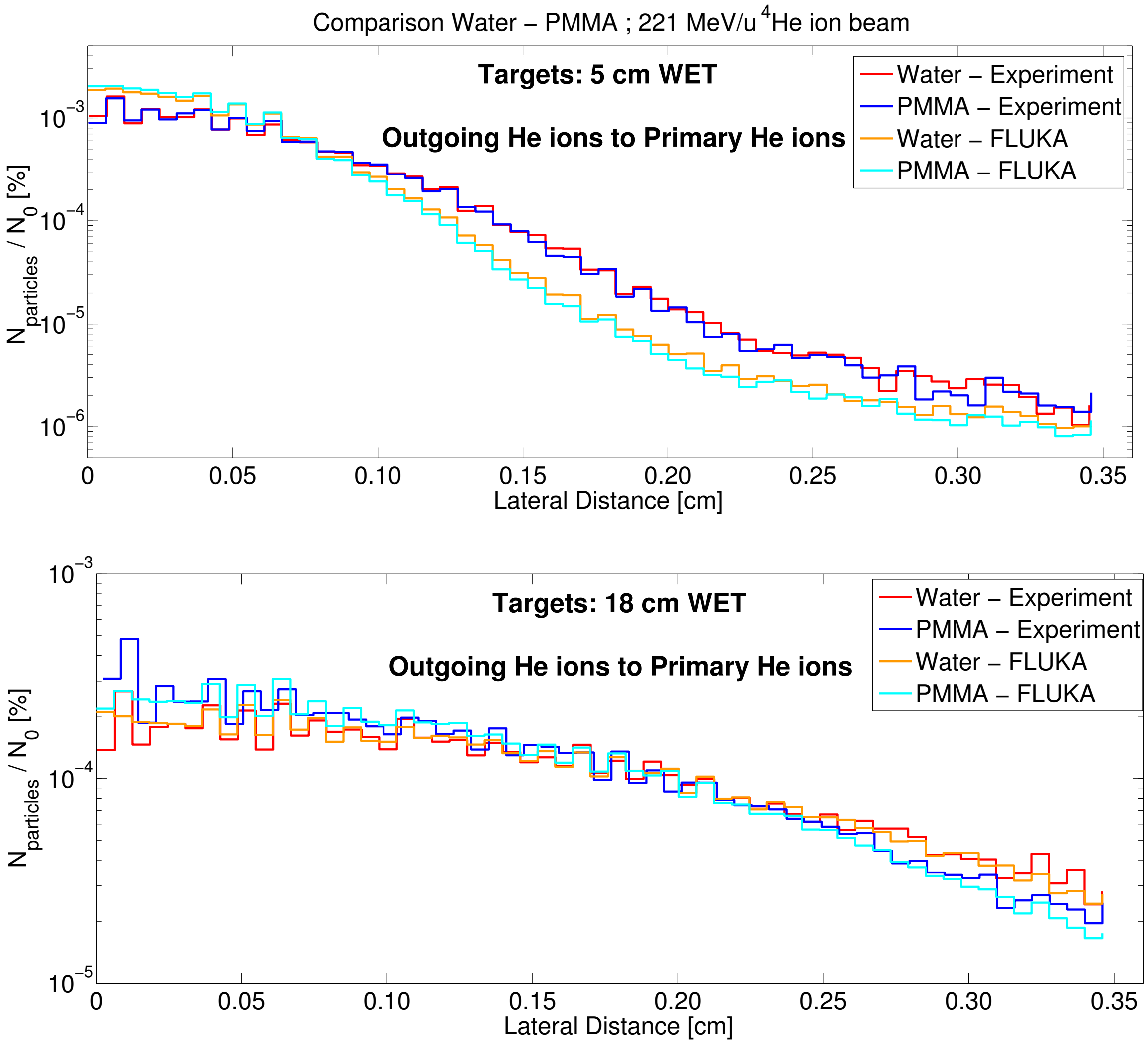

Figure 6.16: Distribution of helium ions registered in the second detector as a function of the lateral distance to the corresponding incoming helium ion position in the first detector. The results were obtained with water and PMMA targets 5 cmWET (*top*) and 18 cmWET (*bottom*) thick irradiated with a 221 MeV/u helium ion beam.

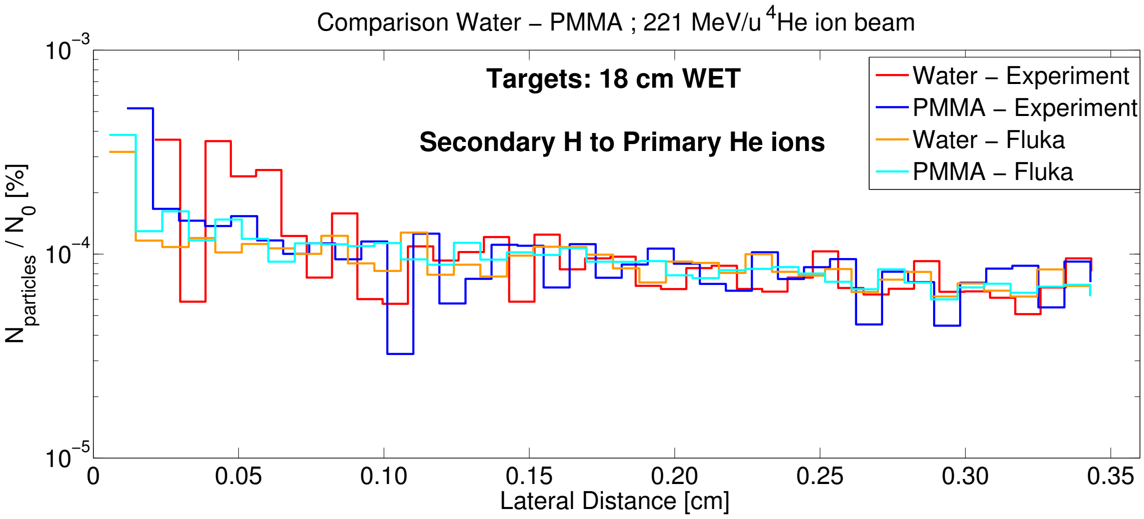

Figure 6.17: Distribution of H registered in the second detector as a function of the lateral distance to the corresponding incoming helium ion position in the first detector. The results were obtained with water and PMMA targets 18 cmWET thick irradiated with a 221 MeV/u helium ion beam.

and the PMMA targets, and between the experiments and the simulations. However, due to the lower amount of detected particles, the experimental uncertainties are greater for d^{H}_{mean} (~2%) than for d^{He}_{mean} (<1%). Moreover, the d^{H}_{mean} values increase more slowly than d^{He}_{mean}, within the same range of target thicknesses. That is in contrast with the expectations, since the cumulative effect of scattering is higher in thicker targets and scattering processes should influence the trajectories of light particles more strongly. In Figure 6.15 a reduction in the percentage of H detected was observed beyond a certain target thickness (about 10 cmWET). The fragments lost are expected to be mainly those produced at the beginning of thick targets, and therefore at greater distances to the second detector. They had higher probability of not being detected behind the phantoms, as the solid angle subtended by the detectors became smaller with increasing distance to them. Moreover, those fragments may undergo further scattering within the phantom. Therefore, an underestimation of the d^{H}_{mean} values may occur in thick targets. Similar results were found in the measurements with carbon ion beams (Study 1, see Table 6.6).

Comparison between d_{mean} and $d_{max(80\%)}$

For the helium ions, the maximum distances reached by 80% of the particles were determined. The results were compared to the mean distance values and to the simulations. The values are listed in Table 6.9 for three targets thicknesses (5 cmWET, 10 cmWET and 18 cmWET). The greater value among d^{He}_{mean} and $d^{He}_{max(80\%)}$ is highlighted in Table 6.9. The uncertainties of $d^{He}_{max(80\%)}$ were calculated as described in Section 5.4.3.

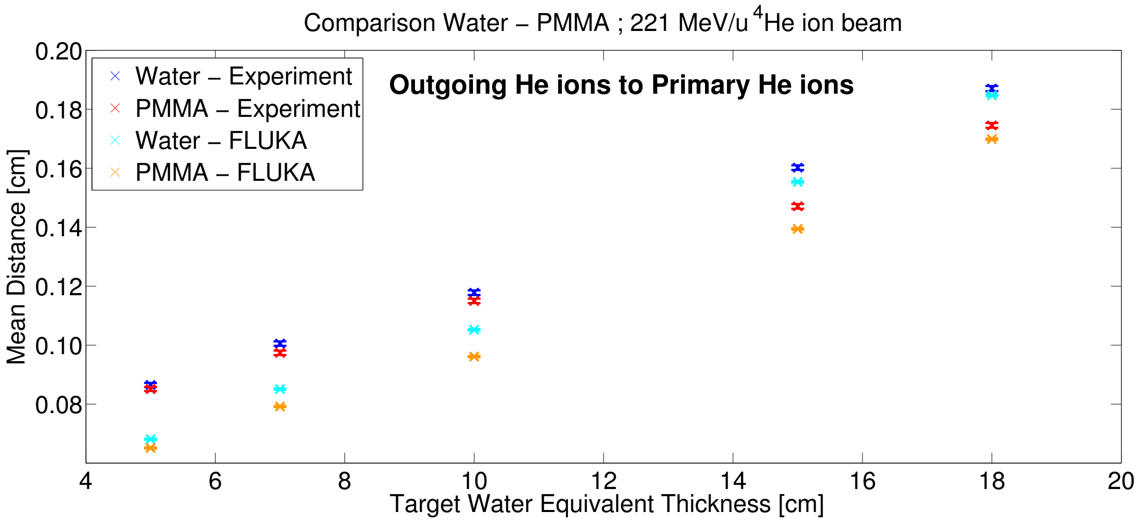

Figure 6.18: Mean lateral distances between the helium ion positions registered in the second detector and the corresponding incoming primary helium ion positions in the first detector. The water and the PMMA targets were irradiated with a 221 MeV/u helium ion beam.

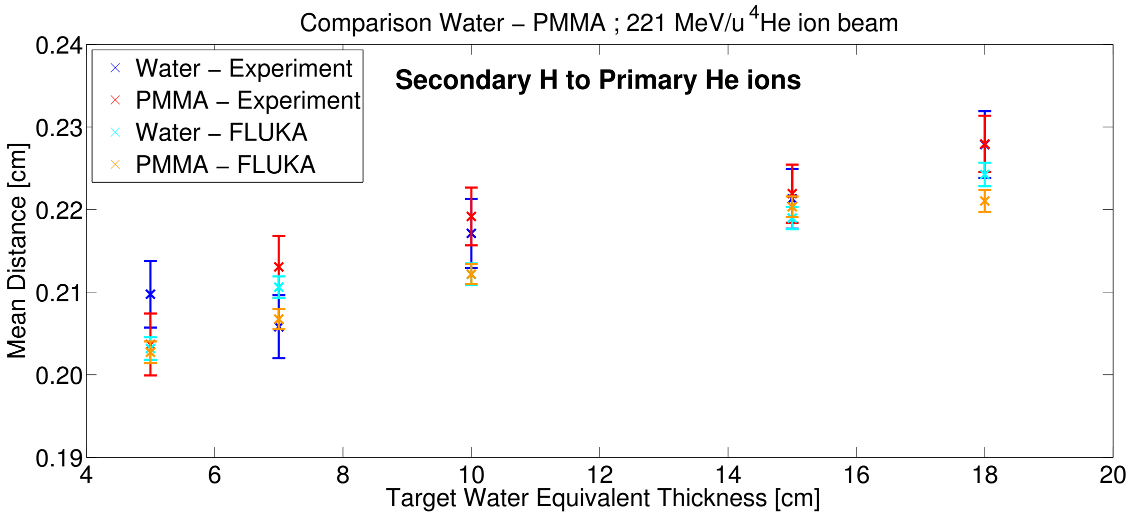

Figure 6.19: Mean lateral distances between the secondary H positions registered in the second detector and the corresponding positions of the incoming primary helium ions in the first detector. The water and the PMMA targets were irradiated with a 221 MeV/u helium ion beam.

Table 6.9: Comparison between the d^{He}_{mean} and $d^{He}_{max(80\%)}$ values, for three target thicknesses (5 cmWET, 10 cmWETand 18 cmWET). Measurements were performed with a 221 MeV/u helium ion beam. $d^{He}_{Experiment}$ and d^{He}_{FLUKA} refer to both d^{He}_{mean} and $d^{He}_{max(80\%)}$ calculated in the experiments and in FLUKA.

	Experiment		FLUKA	
	d^{He}_{mean} (10^{-3} cm)	$d^{He}_{max(80\%)}$ (10^{-3} cm)	d^{He}_{mean} (10^{-3} cm)	$d^{He}_{max(80\%)}$ (10^{-3} cm)
Water 5	**86.5±0.7**	79.3±1.7	68.1±0.2	63.8±1.7
PMMA 5	**85.1±0.7**	79.3±1.7	65.1±0.2	63.7±1.7
Water 10	**117.8±0.8**	110.0±1.7	105.2±0.2	104.6±1.7
PMMA 10	**115.0±0.7**	104.6±1.7	96.1±0.2	94.4±1.7
Water 18	187.0±0.9	**201.6±1.7**	187.4±0.3	201.5±1.7
PMMA 18	174.5±0.8	**177.2±1.7**	169.9±0.3	181.1±1.7
Summary	Thickness Dependency		$d^{He}_{Experiment} \geqslant d^{He}_{FLUKA}$	

d^{He}_{mean} was higher than $d^{He}_{max(80\%)}$ for targets 5 cmWET and 10 cmWET thick, but it was found to be smaller for the thickest targets, behind which the lateral particle distributions were broader. Moreover, both d^{He}_{mean} and $d^{He}_{max(80\%)}$ were smaller for the PMMA than the respective water phantoms, both in the measurements and in FLUKA. This reflects the fact that the lateral particle distributions were sharper behind the PMMA than the water targets. This might be due to the smaller geometrical thickness of the PMMA phantoms with respect to the coupled water targets (see Table 6.1).
The d^{He}_{mean} and $d^{He}_{max(80\%)}$ obtained in the simulations are smaller or equal to the experimental values. The differences decrease with increasing target thickness.

6.4 Fragmentation of Carbon Ions in Tissue and in Water

The interactions occurring in carbon ion beams were investigated and compared between tissue equivalent materials (TEMs) (lung, adipose, inner bone and cortical bone) and water phantoms with the same water equivalent thickness (see Table 6.2). A detailed description of the experimental apparatus and the parameters used can be found in Section 5.1 and in Table 5.1. The experiments were also compared to FLUKA Monte Carlo simulations. The target labelings used in this thesis are listed in Table 6.4.

6.4.1 Investigation of the ion spectra

In order to identify and quantify the particle species registered behind the targets, hand drawn regions in 2D distributions of the measured clusters in variables of cluster signal and cluster size were used, as described in Section 5.4.2. In the following, $N_{particles}$ denotes the amount of particles (H, He, Li, Be, B or C, as specified) detected behind the targets, while N_0 is the number of incoming primary carbon ions. All results were normalized to N_0.

Carbon ions detected behind the targets

The amount of carbon ions detected behind the investigated tissue equivalent materials and water targets are shown in Figure 6.20. A decrease in the number of outgoing particles with increasing WET of the targets is visible. However, to perform a comparison among the tissue surrogates, not only the WET but also the chemical compositions of the materials (listed in Table 4.3) should be considered.

The experimental results were found to be in agreement within their uncertainties, between tissue surrogates and water. A small difference (<1%) was measured only between Adipose and its correspondent water phantom (Water(Adipose)). Hence, the different chemical compositions between the tissue surrogates and water did not influence the results significantly, in the range of investigated target thicknesses and beam energies.

In FLUKA, more carbon ions were detected behind the targets, with differences between 7% (in case of Adipose) and 11% (in case of Lung).

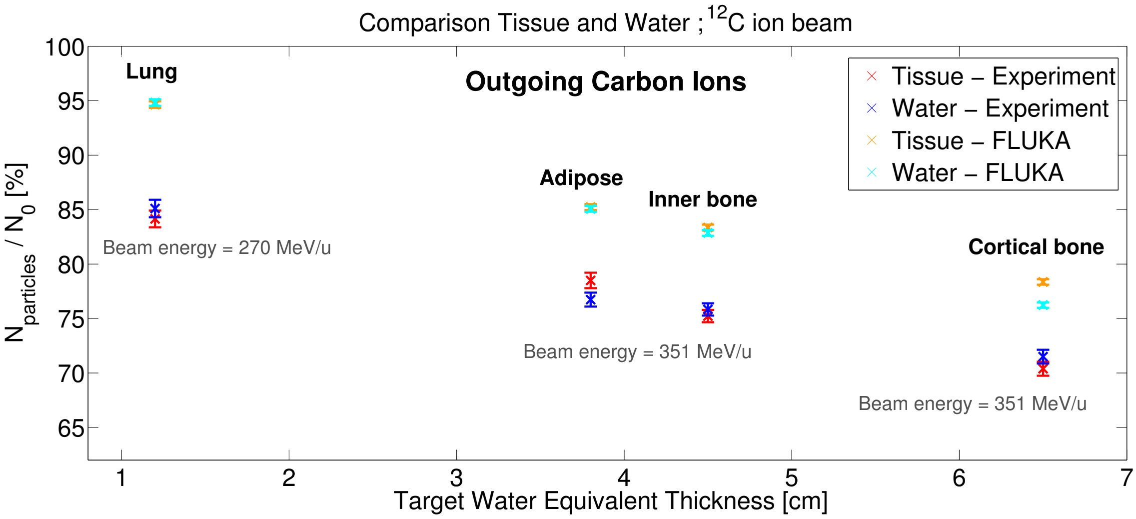

Figure 6.20: Number of carbon ions detected behind tissue equivalent material and water targets, irradiated with carbon ion beams. The experimental results are compared with those obtained by FLUKA Monte Carlo simulations. The data are normalized to the number of primary carbon ions.

Fragments detected behind the targets

The numbers of fragments (H, He, Li, Be) detected behind the targets are shown in Figure 6.21, Figure 6.22, Figure 6.23 and Figure 6.24. As previously discussed in Section 6.5.3, the results for boron were found to be not accurate enough, as regards ion spectroscopy studies, due to the low abundance of detected particles. Therefore they are not shown in this thesis.

For all particle species, both in the experiments and in the simulations, steady increases in the number of detected particles were found as a function of the WET of the targets. Hence, unlike the results obtained in the first two studies (*Fragmentation of Carbon/Helium Ions in Water and in PMMA*, presented in Section 6.2.1 and Section 6.3.1), no maxima were observed here.

In the experiments, good agreement was found in the amount of lithium and beryllium detected behind coupled targets. Nevertheless, significant differences were found for the light fragments (H, He), and especially in the case of lung and cortical bone surrogates with respect to their equivalent water targets. The relative differences are $\sim$42 and $\sim$30% in the amount of H and He registered behind Lung and Water(Lung), and $\sim$14% and $\sim$7% in the amount of H and He registered behind Cortical Bone and Water(Cortical Bone). As shown in Table 6.2, Lung and Cortical Bone have WEPLs which differ more from the value of 1 than Adipose and Inner Bone. Therefore the differences between their geometrical thicknesses and those of the corresponding water phantoms are also higher. Hence, the greatest differences were expected for those materials.

The results obtained from the simulations reproduce the experimental ones well in the case of heavy fragments. Greater differences were observed for the light fragments: the amount of H detected was about 50% higher in the simulations, for all targets.

However, although the results are not consistent, both in the experiments and in FLUKA:

- the percentage of detected H was lower behind Lung than Water(Lung) (Figure 6.21)
- the percentage of detected H was higher behind Cortical Bone than Water(Cortical Bone) (Figure 6.21)
- the percentage of detected He was lower behind Lung than Water(Lung) (Figure 6.22)
- the percentage of detected He was lower behind Cortical Bone than Water(Cortical Bone) (Figure 6.22)

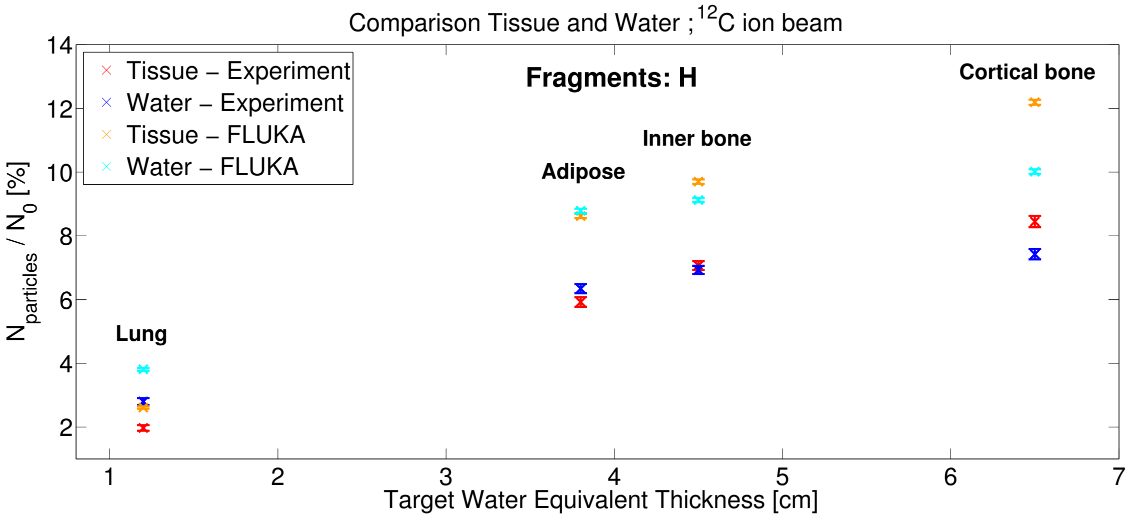

Figure 6.21: Number of secondary H detected behind tissue equivalent materials and water targets, irradiated with carbon ion beams. Initial beam energies equal to 270 MeV/u (in the case of Lung and corresponding water target) or 351 MeV/u (in the other cases) were used. The experimental results are compared with those obtained by FLUKA Monte Carlo simulations. The data are normalized to the number of primary carbon ions.

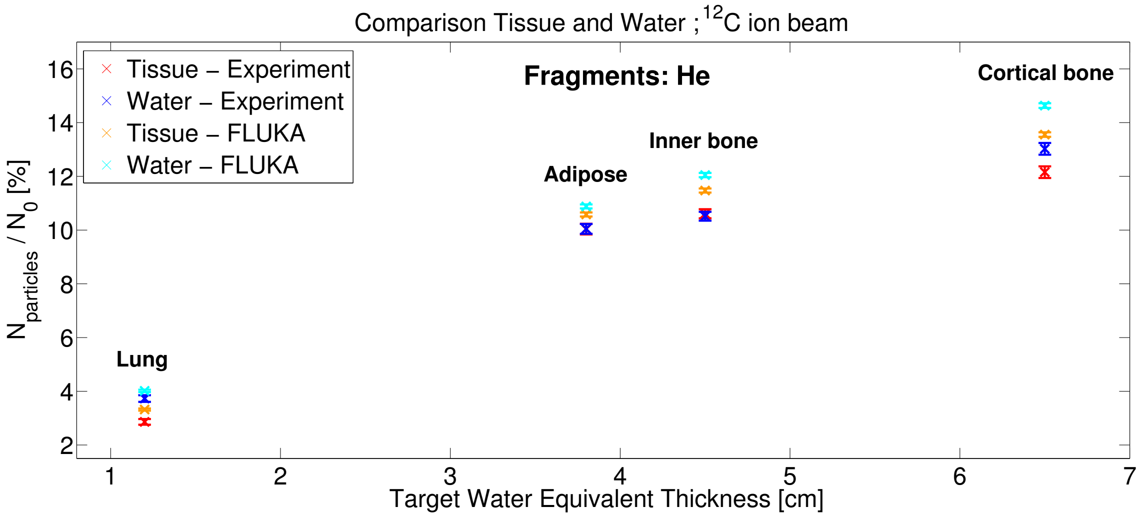

Figure 6.22: Number of secondary He detected behind tissue equivalent materials and water targets, irradiated with carbon ion beams. Initial beam energies equal to 270 MeV/u (in the case of Lung and corresponding water target) or 351 MeV/u (in the other cases) were used. The experimental results are compared with those obtained by FLUKA Monte Carlo simulations. The data are normalized to the number of primary carbon ions.

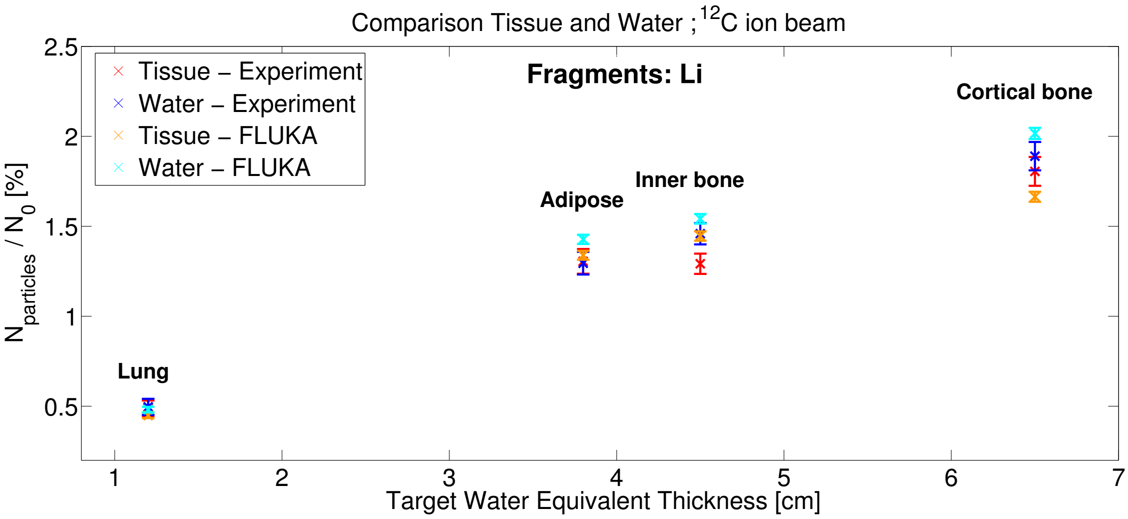

Figure 6.23: Number of secondary Li detected behind tissue equivalent materials and water targets, irradiated with carbon ion beams. Initial beam energies equal to 270 MeV/u (in the case of Lung and corresponding water target) or 351 MeV/u (in the other cases) were used. The experimental results are compared with those obtained by FLUKA Monte Carlo simulations. The data are normalized to the number of primary carbon ions.

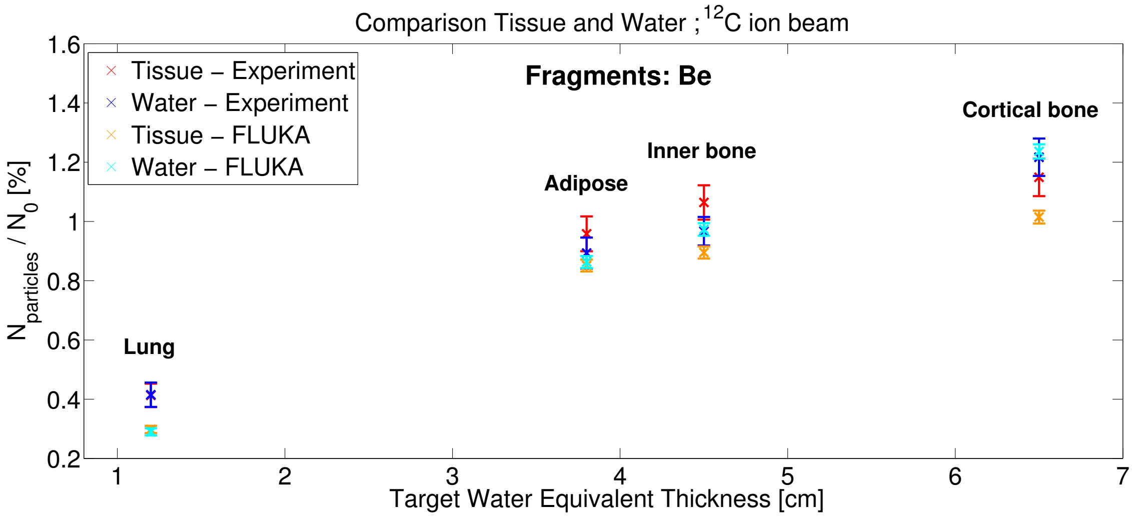

Figure 6.24: Number of secondary Be detected behind tissue equivalent materials and water targets, irradiated with carbon ion beams. Initial beam energies equal to 270 MeV/u (in the case of Lung and corresponding water target) or 351 MeV/u (in the other cases) were used. The experimental results are compared with those obtained by FLUKA Monte Carlo simulations. The data are normalized to the number of primary carbon ions.

6.4.2 Analysis of the lateral particle distributions

The lateral particle distributions were investigated in terms of lateral distances between the particle positions registered behind the targets and the primary particle positions in the first detector (as illustrated in Figure 5.7). Only particles with distances $\leqslant$0.35 cm were considered in the data analysis, as described in Section 5.4.
The distributions of the particles (primary or secondary) registered in the second detector were investigated as a function of their distances to the projected primary particle positions. The particles were gathered in three groups: carbon ions, secondary H+He, secondary Li+Be+B. For each group, the mean distance values were calculated for a comparison among different target thicknesses and particle species.

Comparison of the mean distance values
The mean lateral distances obtained for the carbon ions detected behind the targets, d^{C}_{mean}, are shown in Figure 6.25.
The experimental results are in good agreement within their uncertainty for Adipose and Inner Bone with respect to their equivalent water targets. On the contrary, significant differences were measured between Lung and Water(Lung) (+7%) and between Cortical Bone and Water(Cortical Bone) (-8%). Besides the different chemical compositions of the tissue equivalent materials (Table 4.3) with respect to water, the different geometrical thicknesses may also play an important role. Indeed, Lung is thicker than Water(Lung) by about 71%, whereas Cortical Bone is thinner than Water(Cortical Bone) by about 63%, as reported in Table 6.4. Since the cumulative effect of particle scattering depends on the target thickness, the largest differences were expected for those materials.
Also in FLUKA the d^{C}_{mean} values were found to be greater for Lung than for Water(Lung), and smaller for Cortical Bone than for Water(Cortical Bone). However, the d^{C}_{mean} values determined in the simulations were always higher than the experimental ones. The worst case is with Lung, where the d^{C}_{mean} value is about 35% greater (while the experimental uncertainty is 2%).

The mean lateral distances obtained for H+He and for Li+Be+B are shown in Figure 6.26 and Figure 6.27, respectively.
In the experiments, good agreement was found in the case of Adipose, Inner Bone and Cortical Bone with respect to the water targets. A significant difference (10%) was measured only in the d^{H+He}_{mean} between Lung and Water(Lung).
The d^{H+He}_{mean} values obtained in the simulations were in general smaller than the experimental ones, whereas the $d^{Li+Be+B}_{mean}$ values were in general higher. The greatest differences were found in the case of Lung: the d^{H+He}_{mean} value is about 5% lower, while the $d^{Li+Be+B}_{mean}$ is about 163% higher. However, it should be noted that the abundance of Li+Be+B detected is smaller than H+He, and therefore higher inaccuracies can occur in the results achieved for the heavy fragments.

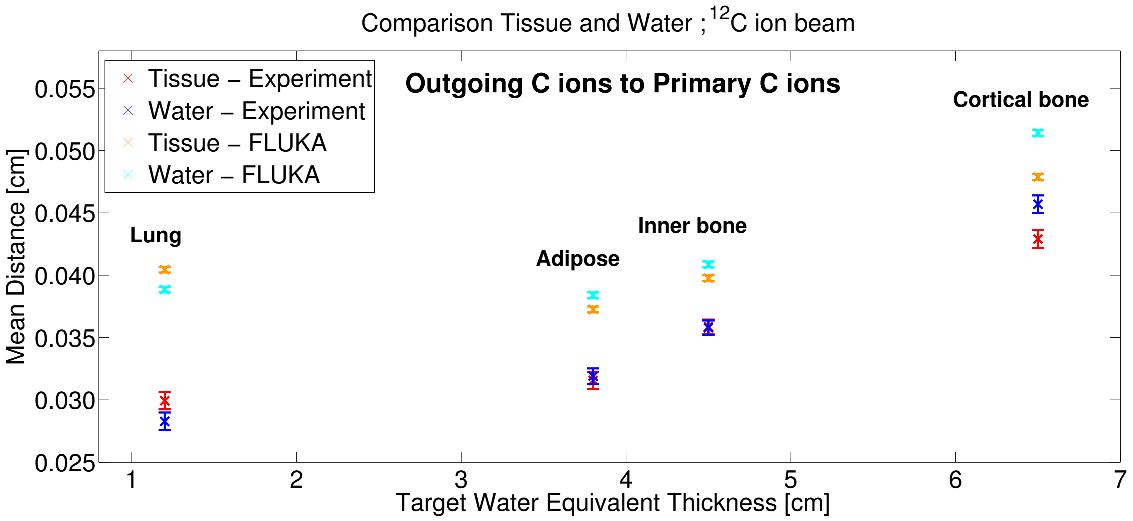

Figure 6.25: Mean lateral distances between the carbon ion positions registered in the second detector and the corresponding incoming primary carbon ion positions in the first detector. The targets were irradiated with carbon ion beams (initial beam energies equal to 270 MeV/u in the case of Lung and corresponding water target, and to 351 MeV/u in the other cases).

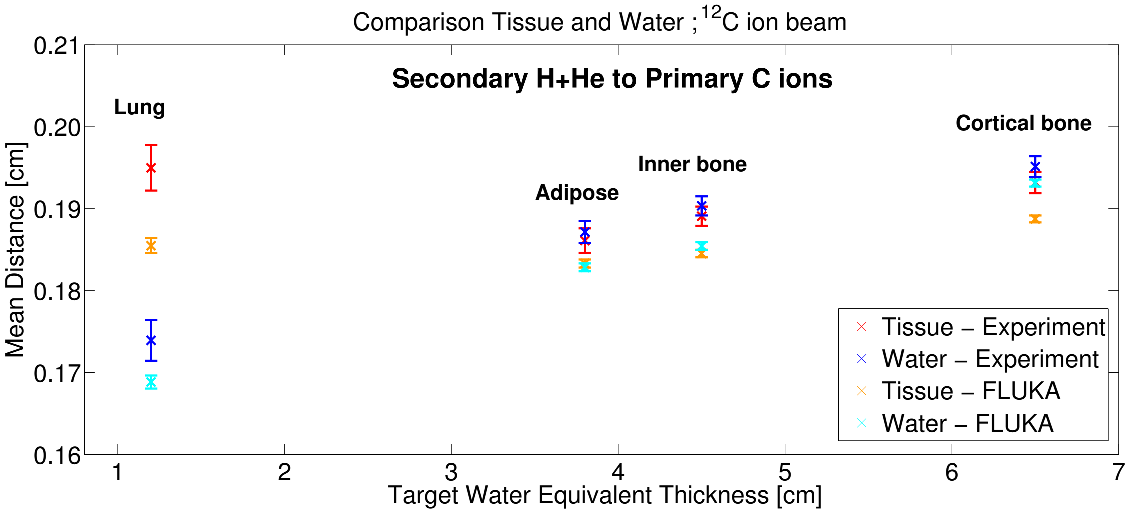

Figure 6.26: Mean lateral distances between the positions of H+He registered in the second detector and the corresponding incoming carbon ion positions in the first detector. The targets were irradiated with carbon ion beams (initial beam energies equal to 270 MeV/u in the case of Lung and corresponding water target, and to 351 MeV/u in the other cases).

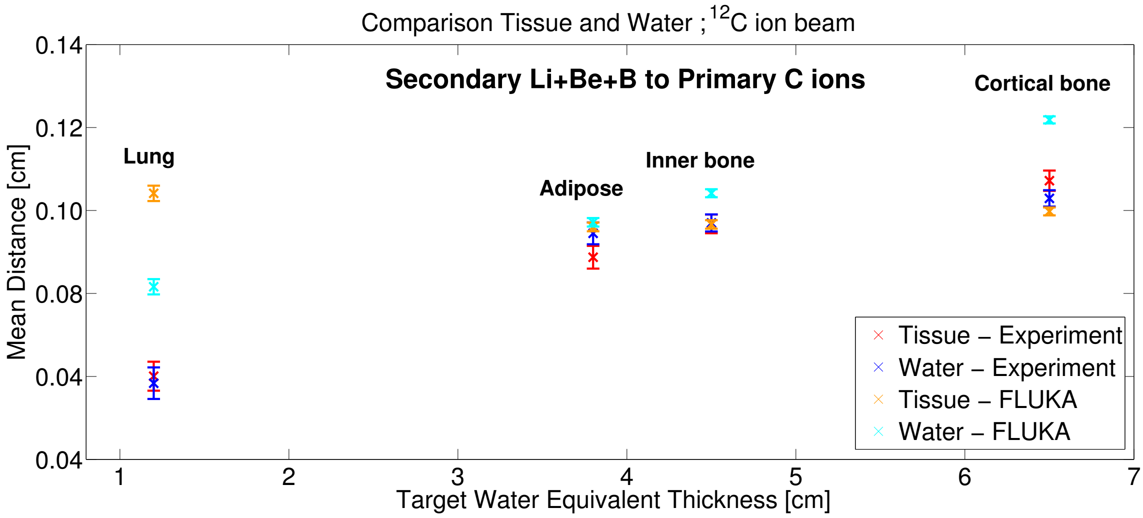

Figure 6.27: Mean lateral distances between the positions of Li+Be+B registered in the second detector and the corresponding incoming carbon ion positions in the first detector. The targets were irradiated with carbon ion beams (initial beam energies equal to 270 MeV/u in the case of Lung and corresponding water target, and to 351 MeV/u in the other cases).

Comparison between d_{mean} and $d_{max(80\%)}$

The mean distance and the maximum distance values reached by 80% of the particles were compared for the carbon ions. As already seen in the previous studies (*Fragmentation of Carbon/Helium Ions in Water and in PMMA*, presented in Section 6.2.2) and Section 6.3.2), the comparison between d_{mean} and $d_{max(80\%)}$ can be used for a qualitative analysis of the width of the lateral particle distributions. The results are available in Table 6.10, where the greater value among d^C_{mean} and $d^C_{max(80\%)}$ is highlighted. The uncertainties of the $d^C_{max(80\%)}$ values were calculated as described in Section 5.4.3.

For a given target, d^C_{mean} was found to be always higher than $d^C_{max(80\%)}$. Therefore, most of the carbon ions were detected in the second detector at small lateral distances to their positions in the first detector. Hence, due to the great mass and energy of the carbon ions, as well as to the relatively small target thicknesses, the primary particles mainly traveled along straight lines parallel to the beam axis, as expected.

The differences between experimental and simulated data are significant, and the d^C_{mean} and $d^C_{max(80\%)}$ values were always higher in FLUKA. Depending on the target, the differences are between 14% and 33% in the case of d^C_{mean}, and between 26% and 46% in the case of $d^C_{max(80\%)}$.

The d^C_{mean} and $d^C_{max(80\%)}$ values determined in the first study (*Fragmentation of Carbon Ions in Water and in PMMA*, see Table 6.7) were instead smaller in the simulations than in the experiments, and in general a better agreement was found in the estimation of the $d^C_{max(80\%)}$ values than the d^C_{mean} values.

Table 6.10: Comparison between the d^C_{mean} and $d^C_{max(80\%)}$ values, calculated between tissue surrogates and water targets with the same WET. The results are compared between experimental data and simulations. Measurements were performed with carbon ion beams. The initial beam energies were equal to 270 MeV/u (in the case of Lung and corresponding water target) or to 351 MeV/u (in the other cases). $d_{Experiment}$ and d_{FLUKA} refer to both d_{mean} and $d_{max(80\%)}$, calculated respectively in the experiments and in FLUKA

	Experiment		FLUKA	
	d^C_{mean} (10^{-3} cm)	$d^C_{max(80\%)}$ (10^{-3} cm)	d^C_{mean} (10^{-3} cm)	$d^C_{max(80\%)}$ (10^{-3} cm)
Lung	**29.9±0.7**	26.2±1.7	40.5±0.2	38.3±1.7
Water(Lung)	**28.3±0.7**	23.0±1.7	38.9±0.2	38.1±1.7
Adipose	**31.6±0.7**	28.0±1.7	37.3±0.2	38.0±1.7
Water(Adipose)	**31.9±0.6**	27.6±1.7	38.4±0.2	38.1±1.7
Inner Bone	**35.9±0.6**	27.8±1.7	39.8±0.2	38.0±1.7
Water(Inner Bone)	**35.8±0.6**	27.7±1.7	40.9±0.2	38.0±1.7
Cortical Bone	**42.9±0.7**	38.2±1.7	47.9±0.2	48.1±1.7
Water(Cortical Bone)	**45.7±0.7**	38.4±1.7	51.4±0.2	48.4±1.7
Summary	$d_{mean} \geqslant d_{max(80\%)}$		$d_{Experiment} \leqslant d_{FLUKA}$	

6.5 Analysis of the experimental uncertainties

6.5.1 Uncertainties in the calculation of the offsets between the detectors

Assessment of the uncertainties

To assess the uncertainty in the calculation of the relative offsets between the detectors, the efficiency of the particles matching procedure was investigated for different positions of the first detector. The first detector position shifts were applied offline in the data sets, after the corrections on the detector misalignment discussed in Section 5.2.2. This analysis was carried out with selected test targets (water, PMMA and tissue surrogates) and using both carbon and helium ion beams. Indeed, different chemical compositions, beam energies and particle species might affect the results differently.

Figure 6.28 shows, as an example, the results obtained with the thickest water target, 18 cm_{WET} thick, irradiated with a 430 MeV/u carbon ion beam. A peak is clearly visible centered at zero. Therefore, the maximum efficiency of the particles matching program was achieved when no additional shifts on the first detector were applied. The experimental misalignments between the detectors were hence properly corrected. Similar results were found for all targets, with peaks always centered around the value zero, or ±1 pixel (~55 μm) in few cases (5 over 28 targets).

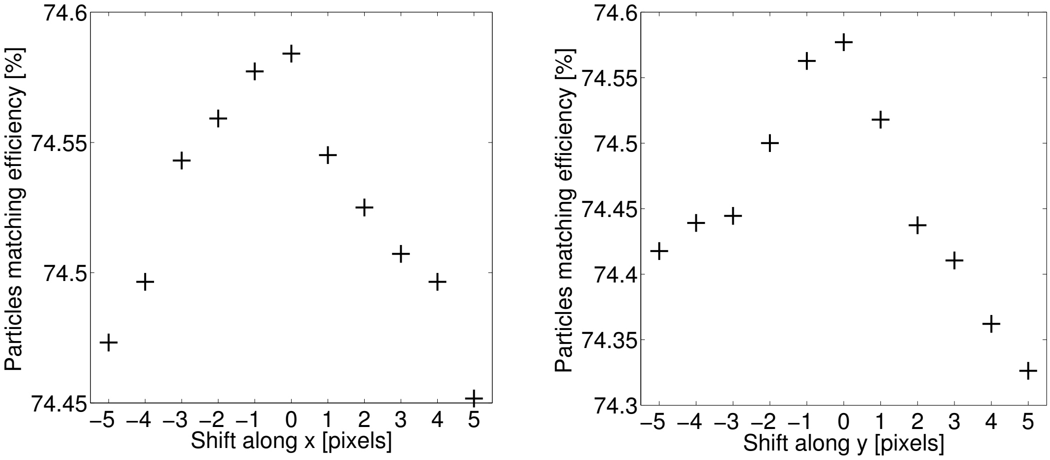

Figure 6.28: Efficiency of the particles matching method (described in Section 5.4), calculated for different positions of the first detector. Shifts along the x and y axis were applied to the first detector position, after correction of the detector misalignment (Section 5.2.2), The results were obtained with a water phantom, 18 cmWET thick, irradiated with a 430 MeV/u carbon ion beam.

Influence of a residual detector misalignment on the results

In the previous section it was shown that the corrections on the detector misalignment were performed with a precision ⩽1 pixel (~55 μm). The influence of a residual misalignment between the first and second detector on the quantification of the particle species and on the lateral particle distributions was investigated. Moreover, a residual misalignment between the detectors could contribute to the differences observed between the experiments and the simulations, where no detector misalignment occurred. The position of the first detector was shifted by ±1 pixel along the x or y axis. As before, these shifts were applied offline in the data sets, after the corrections on the detector misalignment. The results obtained with the first detector in different positions were compared to the reference (that is when no additional shifts are applied) and to the simulations.

The particle species detected behind the targets were quantified by means of hand drawn regions in 2D scatter plots of cluster signal and cluster size, as described in Section 5.4. Table 6.11 shows the results obtained with Water 5 cmWET irradiated with a 430 MeV/u carbon ion beam. For this target the greatest differences between the experiments and the simulations in the first study (*Fragmentation of Carbon Ions in Water and in PMMA*) were found. Only the two worst cases are shown in Table 6.11.

Table 6.11: Number of particles detected behind a water target, 5 cmWET thick, irradiated with a 430 MeV/u carbon ion beam. The reference (highlighted in the table) and the simulated data are obtained without applying any shift to the first detector. The second and third column show the experimental results obtained with the first detector shifted in different positions. Data were normalized to the number of incoming primary ions in the first detector.

	Experiment			FLUKA
	S_x=S_y=0 px N (%)	S_x=-1 px ; S_y=1 px N (%)	S_x=1 px ; S_y=1 px N (%)	S_x=S_y=0 px N (%)
H	**7.95 ± 0.12**	7.92± 0.12	7.90 ± 0.12	11.31 ± 0.08
He	**12.40 ± 0.15**	12.38 ± 0.15	12.41 ± 0.15	13.68 ± 0.08
Li	**1.71 ± 0.05**	1.73 ± 0.05	1.71 ± 0.05	1.70 ± 0.03
Be	**0.98 ± 0.04**	0.98 ± 0.04	0.98 ± 0.04	1.08 ± 0.02
B	**0.97 ± 0.04**	1.07 ± 0.04	1.01 ± 0.04	2.62 ± 0.03
C	**76.8 ± 0.5**	76.8 ± 0.5	76.6 ± 0.5	80.3 ± 0.3

The experimental results are consistent within their uncertainties, for all particle species. Therefore, a residual misalignment between the first and second detector of 1 pixel would not influence the quantification of the particle species significantly. The significant differences observed between the experiments and the simulations are hence not due to experimental inaccuracies in the detector positioning.

The influence of a residual misalignment between the first and the second detector on the lateral particle distributions was also investigated. In Table 6.12 the d_{mean} values obtained with Water 5 cmWET irradiated with a 430 MeV/u carbon ion beam are compared for different positions of the first detector, for different particle groups, and between the experiments and the simulations. Only the worst cases are shown, as examples. At the bottom of the table, the relative differences with respect to the reference measurements, that is when no additional shifts are applied to the first detector, are listed.
Table 6.12 shows that, shifting the first detector in different positions along the x and y axis by 1 pixel, significant fluctuations in the d^{C}_{mean} values occur, whereas the d^{H+He}_{mean} and $d^{Li+Be+B}_{mean}$ values are consistet within their uncertainties. However, the fluctuations observed in the experimental d^{C}_{mean} values are smaller ($\leqslant \pm 4\%$) than the differences between the simulated and the experimental data (17%). It follows that a residual detector misalignment cannot be the only cause for the differences found between the experiments and the simulations. Other sources of uncertainties need to be considered to explain these findings.

Table 6.12: Mean lateral distances of different particle species registered in the second detector with respect to the corresponding incoming carbon ion positions in the first detector. Measurements were performed with a water target, 5 cmWET thick, irradiated with a 430 MeV/u carbon ion beam. The reference (highlighted in the table) and the simulated data are obtained without applying any shift to the first detector. The second and third column show the results obtained with the first detector shifted in different positions . At the bottom of the table, the relative differences with respect to the reference measurements are listed.

	Experiment			FLUKA
	S_x=S_y=0 px d_{mean} (10^{-3} cm)	S_x=-1 px ; S_y=1 px d_{mean} (10^{-3} cm)	S_x=1 px ; S_y=1 px d_{mean} (10^{-3} cm)	S_x=S_y=0 px d_{mean} (10^{-3} cm)
C	**49.7±0.5**	51.1±0.5	51.8±0.5	41.4±0.2
H+He	**187.3±0.9**	187.3±0.9	187.4±0.9	182.6±0.4
Li+Be+B	**128±2**	128±2	129±2	98.9±0.9
Relative deviations with respect to the reference				
	Experiment			FLUKA
C	-	3%	4%	17%
H+He	-	0%	0.05%	23%
Li+Be+B	-	0%	0.8%	2.5%

6.5.2 Uncertainties due to the different WETs of the targets

For all coupled targets, the WETs were found to be in agreement within their uncertainties, as shown in Table 6.1 and Table 6.2. Although the differences in the WETs between coupled targets were smaller than the experimental uncertainty, their influence on the results was investigated. For this purpose, two PMMA targets were used: PMMA 15 cmWET, with WET equal to (14.54±0.03) cm, and PMMA 15^+ cmWET, with WET equal to (14.61±0.03) cm. The WETs of these two targets are not consistent within their uncertainties. The two targets were irradiated with a 430 MeV/u carbon ion beam and the results were compared.

To quantify the amount of particle detected behind the phantoms, the same hand drawn regions in the 2D scatter plots of cluster signal and cluster size were used. As Table 6.13 shows, the results were in agreement within their statistical uncertainties, for each particle species.

Table 6.13: Number of particles registered behind PMMA 15 $\mathrm{cm_{WET}}$ (WET = (14.54±0.03) cm) and PMMA 15^+ $\mathrm{cm_{WET}}$ (WET = (14.61±0.03) cm), irradiated with a 430 MeV/u carbon ion beam. Same hand drawn regions were used in the 2D scatter plots of cluster signal and cluster size. The data are normalized to the number of incoming primary carbon ions.

	PMMA 15 $\mathrm{cm_{WET}}$ N (%)	PMMA 15^+ $\mathrm{cm_{WET}}$ N (%)
H	9.66 ± 0.14	9.61 ± 0.14
He	16.81 ± 0.19	16.76 ± 0.19
Li	2.18 ± 0.06	2.26 ± 0.06
Be	1.59 ± 0.05	1.60 ± 0.05
C	54.1 ± 0.4	54.8 ± 0.4

The mean lateral distances between the particle positions registered behind the targets and the primary particle positions registered in the first detector were also compared. The results, listed in Table 6.14, were consistent within their uncertainties, for all particle groups.

Table 6.14: Mean lateral distances of different particle species registered in the second detector with respect to the corresponding incoming carbon ion positions in the first detector. The results are shown for PMMA 15 $\mathrm{cm_{WET}}$ (WET = (14.54±0.03) cm) and PMMA 15^+ $\mathrm{cm_{WET}}$ (WET = (14.61±0.03) cm), irradiated with a 430 MeV/u carbon ion beam.

	d^{C}_{mean} (10^{-3} cm)	d^{H+He}_{mean} (10^{-3} cm)	$d^{Li+Be+B}_{mean}$ (10^{-3} cm)
PMMA 15 $\mathrm{cm_{WET}}$	97.4 ± 0.5	208.4 ± 0.8	181 ± 2
PMMA 15^+ $\mathrm{cm_{WET}}$	97.0 ± 0.5	208.7 ± 0.8	184 ± 2

As PMMA 15 $\mathrm{cm_{WET}}$ and PMMA 15^+ $\mathrm{cm_{WET}}$ have WETs which differ more than the coupled targets investigated in this thesis, the differences observed in the results (Section 6.2, Section 6.3 and Section 6.4) are not due to the different WETs of the phantoms. Table 6.13 and Table 6.14 also show a satisfactory reproducibility of the results.

6.5.3 Uncertainties related to the hand drawn regions

Measurements with Carbon ion beams

Figure 6.29 shows an example of the 2D distribution of the measured clusters in variables of cluster signal and cluster size, obtained behind a 18 $\mathrm{cm_{WET}}$ thick water target irradiated with a 430 MeV/u carbon ion beam. Hand drawn regions were used to quantify the registered particle species.

To investigate the quality of the method and to assess the influence of different hand drawn regions on the calculated number of particles, the quantification of the particle species was repeated three times in the same 2D scatter plots. A first set of regions was used to calculate the reference values, for all particle species; subsequently smaller and larger regions were drawn to get an under- and an over-estimation of the number of particles detected. This analysis was carried out for various target thicknesses and materials. In Table 6.15, the results obtained with the thickest water phantom, 18 $\mathrm{cm_{WET}}$, are shown as an example, In that target, the highest amount of fragmentation processes took place. The values are in agreement within their statistical uncertainties, except for boron. For this particle species the identification in the 2D scatter plot was more complicated than for the other particles. Figure 6.29 shows that the boron area tends to overlap with the carbon ion region. However, due to the high amount of detected carbon ions, small deviations in the size and shape of the hand drawn regions did not influence the results for the primary particles significantly. On the contrary, for boron, the abundance of detected particles was much lower (about 1%-2%) and relative deviations between 20% and 60% were measured using different regions for the same data set. Therefore, due to the low accuracy achieved, the results for boron were not included in the investigation of the ion spectra.

Table 6.15: Number of particles detected behind a 18 $\mathrm{cm_{WET}}$ thick water phantom, irradiated with a 430 MeV/u carbon ion beam. The values were obtained drawing different regions in the same 2D scatter plot of cluster signal and cluster size. The first estimations of detected particles were used as reference. Subsequently, smaller and larger regions were drawn, which provide an under- and an over-estimation of the number of detected particles. Data were normalized to the number of incoming particles in the first detector.

	Under Estimation N (%)	**Reference** N (%)	Over Estimation N (%)
H	7.61 ± 0.12	7.63 ± 0.12	7.63 ± 0.12
He	13.75 ± 0.17	13.78 ± 0.17	13.86 ± 0.17
Li	1.90 ± 0.06	1.94 ± 0.06	1.96 ± 0.06
Be	1.26 ± 0.05	1.27 ± 0.05	1.27 ± 0.05
B	1.31 ± 0.05	1.58 ± 0.05	2.09 ± 0.06
C	47.6 ± 0.4	48.1 ± 0.4	48.1 ± 0.4

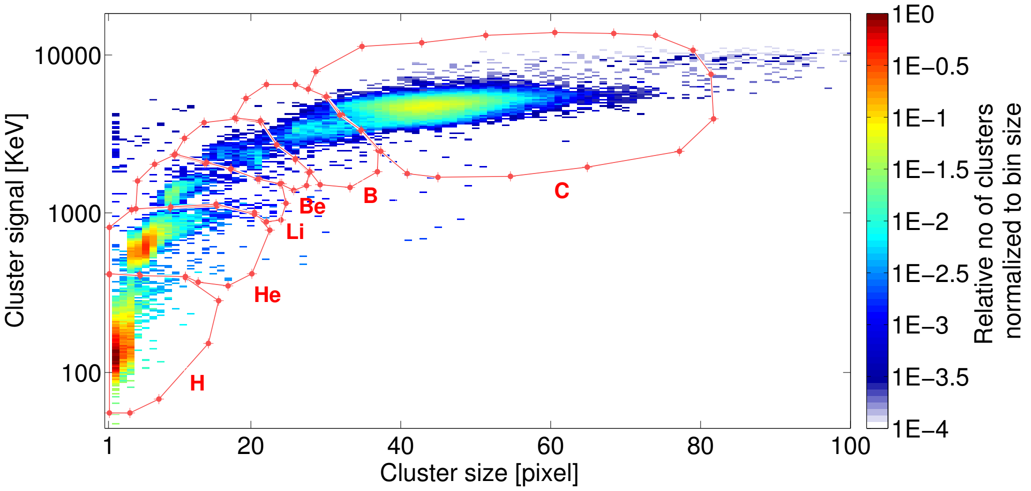

Figure 6.29: 2D distribution of the measured clusters in variables of cluster signal and cluster size, obtained behind a 18 cmWET thick water phantom irradiated with a 430 MeV/u carbon ion beam. Carbon ions as well as fragments produced within the target can be identified and quantified using hand drawn regions (red lines).

Measurements with Helium ion beams

Similarly to the analysis performed with carbon ion beams, the influence of different hand drawn regions on the particle species quantification was assessed for measurements with helium ion beams. As before, for the same experimental data set, three regions were drawn to quantify the particles registered behind the targets. One set of regions was used to obtain the reference values for H and He. Then, smaller and larger regions were drawn to have an under- and an over-estimation of the number of particles detected. This analysis was carried out for different targets. The results obtained with Water 18 cmWET are listed, as an example, in Table 6.16.

The number of detected particles (H and He) obtained with different hand drawn regions are in agreement within their statistical uncertainties. In comparison to the measurements with carbon ion beams, the areas belonging to different particle species are in this case even easier to distinguish, as shown in Figure 6.30.

Table 6.16: Number of particles detected behind a 18 cmWET thick water phantom, irradiated with a 221 MeV/u helium ion beam. The values were obtained drawing different regions in the same 2D scatter plot of cluster signal and cluster size. The first estimations of detected particles were used as reference. Subsequently, smaller and larger regions were drawn, which provide an under- and an over-estimation of the number of detected particles. Data were normalized to the number of incoming particles in the first detector.

	Under Estimation N (%)	**Reference** N (%)	Over Estimation N (%)
H	2.37 ± 0.10	2.42 ± 0.10	2.44 ± 0.10
He	51.9 ± 0.6	51.9 ± 0.6	51.9 ± 0.6

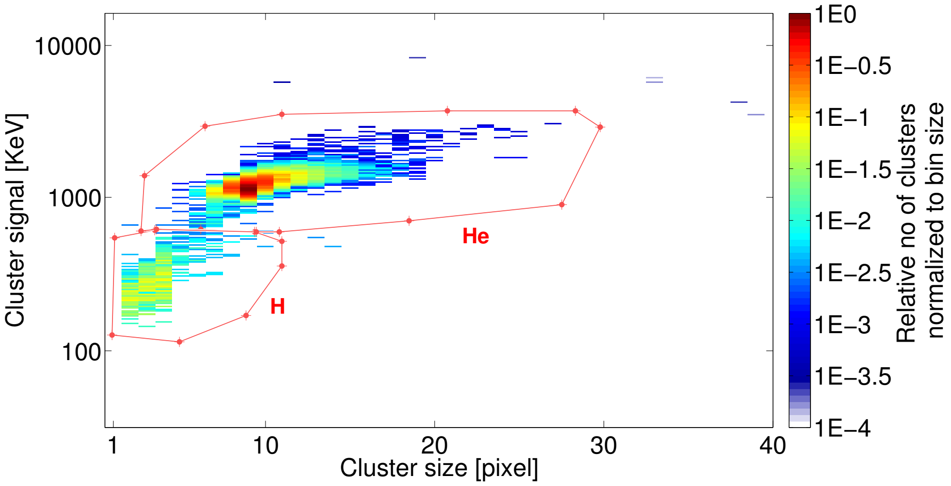

Figure 6.30: 2D distribution of the measured clusters in variables of cluster signal and cluster size, obtained behind a 18 cmWET water phantom, irradiated with a 221 MeV/u helium ion beam. Helium ions as well as secondary H can be identified and quantified using hand drawn regions (red lines).

6.5.4 Summary of the experimental uncertainties

The major sources of experimental uncertainties have been investigated in the previous paragraphs. The findings are summarized in the following:

- Corrections of detector misalignments were performed with a precision $\leqslant$1 pixel (~55 μm) (Section 6.5.1).
- The influence of a residual misalignment between the first and second detector on the quantification of the particle species is negligible when compared to the statistical uncertainties (Section 6.5.1).
- The influence of a residual misalignment between the first and second detector on the lateral particle distributions is not significant or is minor with respect to the differences observed between the experiments and the simulations (Section 6.5.1).
- The differences in the WETs between coupled targets do not influence the results significantly (as regards both the particle species quantification and the lateral particle distributions) (Section 6.5.2).
- The fluctuations in the particle species quantification, due to different hand drawn regions, were found to be smaller than the statistical uncertainties (Section 6.5.3). The only exception is given by boron ions in the measurements performed with primary carbon ion beams. These fragments were the least abundant particles detected. Due to the low reliability, the results for boron were not included in the analysis of the ion spectra.

The statistical uncertainties were associated to the quantification of the particle species, both in the experiments and in the simulations. Other sources of uncertainties (experimental or related to the data analysis method) were considered as described in Chapter 5. Error propagation was performed in accordance to the standard rules.

7 Summary and Discussion

The main challenge in radiotherapy is to deliver a highly conformal dose to the target, while minimizing the unwanted and unavoidable dose in the healthy tissues. Especially in case of young patients, the radiotherapy treatments might affect the growth of normal tissues, bones and nerves. Furthermore, the risk to develop secondary tumors during the lifetime is higher and more relevant for young patients [Allen et al. 2012].

Information on the fragmentation cross sections is required to estimate the beam contamination by light products of the nuclear interactions and consequently to evaluate the dose distributions during treatment planning accurately. In this thesis experiments were conducted to investigate beam attenuation, build-up of secondary and lateral particle distributions for carbon and helium ion beams crossing different materials of clinical interest (water, PMMA and tissue surrogates).

In previous studies regarding fragmentation of carbon ion beams, a telescope system was used [Matsufuji et al. 2011] and time-of-flight measurements were performed [e.g. Gunzert-Marx et al. 2008, Haettner et al. 2013]. The outgoing particles behind the water and the PMMA targets were identified and analysed. In this thesis pixelated semiconductor detectors (Timepix) were used for the measurements. These detectors provide information on the particle arrival time and deposited energy. Moreover, they allow very fast data acquisition and 100% detection efficiency for ions. One of the advantages of the new method is the possibility to considerably reduce the distance between target and detectors to just few cm, as shown in Figure 5.1. This enables to decrease the influence of scattering in air on the outgoing particle trajectories. Moreover, as this experimental setup is much smaller and more manageable than the previous ones, it could be implemented in clinical facilities more easily. However, the different investigation technique required the development of a new analysis method for ion spectroscopy studies [Hartmann 2013]: particle species are identified based on pattern recognition of the clusters generated by each single particle impinging the detector (as described in Section 5.4.2). Moreover, in the present work time coincidence measurements were performed to correlate the particles registered in front of the target with the corresponding particles detected behind the target and belonging to the same event. Therefore, number and type of fragments produced from each single primary ion could be analysed individually. Furthermore, the particles matching process, developed in this thesis and presented in Section 5.4, enabled to improve the quality and reliability of the final findings (as further discussed in Section 7.3).

Monte Carlo simulations of the experiments were performed with the FLUKA code. The same analysis method was applied both to the experimental and simulated data to enable a fair and direct comparison of the results.

7.1 The experimental setup

As Figure 1.1 shows, the contribution of the fragments to the dose in front of the Bragg peak is not negligible, neither for carbon ion nor for helium ion beams. Therefore, measurements were performed in the initial plateau region of the depth-dose curve, where healthy tissues are usually located and which should be spared as much as possible.
In the first two studies (*Fragmentation of Carbon/Helium ions in Water and in PMMA*, Section 6.2 and Section 6.3) the highest beam energies available at HIT were used: 430 MeV/u for carbon ions and 221 MeV/u for helium ions. As the contribution of the fragments increases with increasing initial beam energy, the results achieved in those studies give information on the upper limit within the therapeutic energy range.

The intrinsic beam divergence may affect the estimation of the lateral particle distributions as well as the comparison between the experiments and the simulations. However, both for carbon and for helium ion beams, its influence on the particle positions between the first and the second detector was found to be negligible with respect to the changes in the particle trajectories due to interactions with the target atoms. Hence, the incoming particle trajectories were approximated as straight lines parallel to the beam axis.

The small geometrical acceptance considered in the first detector also enabled to exclude primary particles which were scattered at large angles in the BAMS (see Section 4.1.1): those particle indeed traveled out of the detection area.

7.2 Measurements prior the experiments

7.2.1 Measurements of the target thicknesses in terms of WET

To enable an unbiased comparison between the results achieved with the water and the PMMA targets, or with tissue surrogates and water targets, the WETs of the targets in pairs needed to be as close as possible. Indeed, the WET of any material is the equivalent thickness of water which causes the same loss of the particle energies. As a consequence, if two materials have the same WET, the residual particle energies and ranges behind the targets are the same. However, geometrical thicknesses and chemical compositions of the targets may also influence the physical characteristics of the outgoing particles.

In spite of the limits in the thickiness of the single PMMA slabs available, consistency in the WET values of the coupled targets could be achieved within the experimental uncertainties, as shown in Table 6.1 and Table 6.2. However, Table 6.1 also shows that fluctuations of 1% on the WEPLs determined for the used PMMA targets, composed of several slabs, were found. These differences are due to the variations in the WEPLs of the single PMMA slabs, among which fluctuations up to 5% were measured. The effect was mitigated when the WETs, WEPLs and geometrical thicknesses were measured for the whole PMMA targets.

The WEPL values measured here differ up to 4% from the value measured in Jäkel et al. 2001, equal to 1.165, and from the one used at HIMAC, equal to 1.16 [Matsufuji et al. 2003]. Inaccuracies in the WEPL calculations may lead to significant over- or under-estimations of the calculated WETs, especially with increasing target thickness. Therefore, measurements of the WETs of the investigated phantoms prior the experiments are highly recommended for an accurate and reliable analysis.

The differences in the final WET (listed in Table 6.1 and in Table 6.2) between the coupled targets investigated in this thesis may potentially influence the results. To assess this influence, two PMMA phantoms, whose WETs differ more than the WETs of the coupled targets, were used. The amount and type of particles detected behind these two PMMA phantoms and the lateral distance distributions were compared. All the results were found to be in agreement within their uncertainties, as shown in Table 6.13 and in Table 6.14.
Therefore, the differences in the WETs of the coupled targets were not relevant for the purposes of this work. Other factors which could influence the results significantly are the chemical composition and the geometrical thickness of the targets.

7.2.2 Correction of the detector misalignment

Detector alignment was an important issue for all measurements: imprecise detector positioning may indeed affect the efficiency of the particles matching procedure and the lateral distance distributions. The relative offsets between the detectors in the stack were minimized, as they were mounted together in fixed positions on the motherboard. A more challenging task was instead the alignment of the first detector with respect to the others. In order to reduce systematic uncertainties, the detector positions were kept fixed for the duration of an entire study, and measurements were performed continuously.
Irradiation of the detectors without any phantom (as described in Section 5.2.2) were performed several times within each study to estimate and correct the detector misalignment: a precision $\leqslant 1$ pixel (55 μm) was reached, as shown in Section 6.5.1. Since this method of correcting the detector misalignment was found to be very stable and reliable, it is recommended to be used also for future measurements.
Despite the correction of the relative offsets between the detectors, the effects on the results of a possible residual misalignment between the first detector and the other detectors was investigated. This source of uncertainty may indeed affect the comparison between the experiments and the simulations, where no misalignment between the detectors occurs. In Section 6.5.1 it was estimated that the maximum residual misalignment between the detectors did not exceed 1 pixel ($\sim$55 μm). In order to address its influence on the results, the position of the first detector was shifted along the x and y axis, and the amount of particle species registered behind the targets were compared. Fluctuations smaller than the statistical uncertainties were found (see Table 6.11, for the worst case example). Regarding the mean lateral distances, Table 6.12 shows an example of

results obtained with a water phantom, 5 cmWET thick, irradiated with a 430 MeV/u carbon ion beam, and moving the first detector in different positions (only the worst cases are shown). No significant influence on the mean lateral distances determined for the fragments was found. Instead, differences up to 4% in the d^C_{mean} values were found, while the associated uncertainties are 1.0%. Due to the more forward peaked distributions of the primary ions, the influence of the first detector shifts on the carbon ion lateral distributions was stronger than for the fragments. The observed fluctuations need to be properly considered, as they could affect the final estimations of the lateral particle distributions and the comparison with the simulations.

In the future, a fixed apparatus should be used to connect the two Fitpix devices and to further reduce the uncertainties in the detector positionings.

7.3 Data analysis

7.3.1 The particles matching method

To achieve equivalent results which could be directly compared, the same data analysis procedure was applied to all data sets, both to the experimental and the simulated data. Although the cuts and constrains applied in the data analysis, described in Section 5.4, reduced the number of particles analysed by about an order of magnitude, the influence of the experimental uncertainties on the results was minimized and a higher quality in the final findings could be reached.

Measurements were performed with sufficiently low beam intensity ($<10^4$ particles/s) to guarantee that the particles detected in front and behind the targets were well separated both in space and in time: particles belonging to the same event could then be matched unequivocally. However, only outgoing particles with a lateral distance $\leqslant$0.35 cm from the primary particle positions were investigated. This limit arises from the small areas of the detectors. Larger detectors, currently under development e.g. at the Advacam company, would enable to investigate broader lateral particle distributions. Furthermore, the new generation of Timepix detector (Timepix 3), which allows faster data acquisition and simultaneous measurements in Time- and in ToT-mode in each individual pixel [Poikela, Plosila, and Westerlund 2012, Campbell et al. 2016] would also contribute to improve the studies presented in this thesis. Only one detector layer behind the target, in place of the three detectors currently implemented, would then be necessary, since correlation of the particles in time could be carried out directly in the first and in the second detector. This would enable to simplify the particles matching procedure strongly and therefore to reduce the influence of experimental uncertainties (e.g. related to detector misalignment, particle scattering and fragmentation in the detectors) on the results. In this work the probabilities of fragmentation occurring in the last three detectors were estimated to be between 1% and 3%, depending on the incoming particle species, beam energy, target chemical composition and target thickness.

However, these events could be identified and excluded from the data analysis, both in the experiments and in the simulations, as correlation of the particles could not be performed unambiguously. Indeed:

- if the fragmentation occurred after the sensitive layer of the second detector and before the third detector, a single particle in the second detector was a good match for more than one trajectory (i.e. the trajectories of the arising fragments detected in the third and fourth detectors).
- if the fragmentation occurred behind the sensitive layer of the third detector and in front of the fourth detector, more particles were registered in the fourth than in the third detector at a given time.

In a similar way, overlapping clusters (i.e. clusters produced by particles reaching the detectors close to each other) could be identified and deleted by the data analysis, as unequivocal particle matchings among the three detectors were not possible. Due to the low beam intensity, the probability of overlapping clusters in each detector layer was very small ($<1\%$).

To improve the quality of the investigation method, additional material along the beam path should be reduced as much as possible. A new technology of Timepix detectors, where the chips are through silicon via (TSV) ready [Campbell et al. 2016], gives the possibility to get rid of the bump bonds between sensitive and insensitive layer. The bump bonds may influence the particle trajectories, especially in the case of light and low energetic particles.

7.3.2 Investigations of the ion spectra in mixed fields

Hand drawn regions in the 2D distributions of the measured clusters in variables of cluster signal and cluster size were used to identify different particle species in the second detector, as described in Section 5.4.2. Figure 5.10 shows the improvements achieved in the 2D scatter plots due to the particles matching process: unwanted contributions produced by detector artifacts, electrons and background signals could be excluded. Such background signals arise in each detector layer at different times and therefore they were not included in the data analysis when the particle trajectories were reconstructed through the three detectors placed behind the phantoms.

For measurements with **carbon ion beams**, the uncertainties related to the quantification of different particle species were found to be smaller than the statistical uncertainties, except for boron. The relative uncertainties were $\leqslant 2\%$ for the fragments and $\leqslant 1.0\%$ for the carbon ions (see Table 6.15 for an example). These values are smaller than those obtained in previous studies. For instance, in Haettner et al. 2013, the yields of secondary fragments were measured behind water phantoms irradiated with a 400 MeV/u carbon ion beam (the experiment is described in Section 3.3.1). Identification and quantification of the secondary fragments were performed in 2D scatter plots of particle energy loss and residual energy (ΔE-E). The different experimental parameters and configurations (e.g. beam energy, target thickness, positions of the detectors) do not allow to compare the results directly. However, the experimental uncertainties of the number of particles registered behind the phantoms were estimated to be between 0.3% and 3%, depending on the particle species. Lower uncertainties were reached in this thesis.

Moreover, the possibility to investigate each single event individually and the multiple fragments originated by each single primary ion enabled to gain information on the ion fragmentation processes that could not be achieved in previous studies. This knowledge might be particularly relevant to improve the physics models implemented in the Monte Carlo codes and in the treatment planning systems.

Only for boron, an accurate quantification in the 2D scatter plots of cluster signal and cluster size could not be performed: uncertainties between 20% and 60% were measured. A similar issue arose in the measurements of Haettner [Haettner et al. 2013], too, where a lower accuracy in the determination of the boron yield was found. A characterization of the response of the Timepix detectors to boron ions would contribute to solve this problem.

For measurements with **helium ion beams**, regions belonging to H and He could be well distinguished in the 2D scatter plots of cluster signal and cluster size (an example is shown in Figure 6.30). The fluctuations on the particle species quantification due to different regions drawn in the 2D scatter plots were always smaller than the statistical uncertainties: the relative uncertainties were $\leqslant$2% for H, whereas no significant variations in the number of He were measured (the worst case example is reported in Table 6.16). In Krämer et al. 2016 measurements of H and He behind water targets of different thicknesses were performed in 2D scatter plots of ΔE-E (the experiment is described in Section 3.3.2). The uncertainties in the yields measured in Krämer et al. 2016 arise from the particle identification method and were estimated to be 2% for helium ions and 9% for H. Therefore, also in the measurements with helium ion beams, the ion spectra could be analysed with higher accuracy in the present thesis than in other published studies based on ΔE-E measurements. Moreover, increasing the measurement time, the statistical uncertainties could be further reduced.

Although the method to identify and quantify the different particle species in the 2D distributions of the measured clusters in variables of cluster signal and cluster size was found to be robust, an algorithm to quantify the particle species automatically would further improve the quality of the method. However, the main challenge is with regards to the definition of the constrains needed to distinguish the different regions in the 2D scatter plots. This issue is currently under investigation in the research group at DKFZ.

7.3.3 Analysis of the lateral particle distributions

All the particles registered behind the target with a distance smaller than 0.35 cm to the corresponding primary particle position in the first detector were considered (see Figure 5.8 for an illustration of the method).

In the case of the primary particles, the lateral distributions were found to be rather sharp, especially behind thin targets. Figure 6.8 and Figure 6.16 show some examples of lateral distance distributions obtained with 430 MeV/u carbon ion beams and 221 MeV/u helium ion beams, respectively. For the thickest targets investigated in this thesis, Water and PMMA 18 cm_{WET}, the amount of particles measured at the maximum distance considered, equal to 0.35 cm, was reduced by two order or magnitude in case of carbon ions, and by one order of magnitude in case of helium ions. With decreasing target thickness, the amounts of outgoing carbon or helium ions detected decreased even faster as a function of the lateral distance. Therefore, the used cut at 0.35 cm excluded only a small fraction of primary particles, which were those traveling at greater distances to the beam axis.
The effects of this constrain on the secondary fragments, and especially on the lighter particles, were more relevant. As example, Figure 6.9 shows the lateral distance distributions of H+He behind Water and PMMA 18 cm_{WET} irradiated with a 430 MeV/u carbon ion beam. At the same maximum distance, 0.35 cm, the amount of particles measured was reduced by less than half.

The number of secondary fragments detected was found to increase with increasing target thickness to a maximum, and a subsequent drop was observed. The position of the maximum shifted to greater WETs for heavier fragments, as it can be seen in Figure 6.2, Figure 6.3, Figure 6.4 and Figure 6.5. The loss of fragments detected beyond a certain target thickness was probably due to the greater distances between the fragmentation point and the detectors behind the phantoms, which could be reached in the thicker targets. As the solid angle subtended by the detectors became smaller with increasing distance to them, the probability that the fragments produced at the beginning of thick targets traveled out of the detecting area is higher. Moreover, due to the greater amount of material between the fragmentation points and the detectors, the cumulative effect of particle scattering and the probability to undergo further fragmentation was also higher for the fragments produced at the beginning of the thicker targets.
Larger detectors would enable to investigate particles traveling at greater distances to the beam axis. This would be particularly advantageous in the case of light secondary fragments, which have broader lateral distributions, and in the case of thick targets. Another possibility could be to move the detectors behind the target at different angles from the beam axis, as it was done in other studies (e.g. Gunzert-Marx et al. 2008 and Haettner et al. 2013). However, before performing such kind of measurements, a method to reduce the uncertainties in the detector positioning need to be developed, in order to reach an accuracy comparable to the one achieved in this thesis.

7.4 Fragmentation of Carbon Ions in Water and in PMMA

The experiments were designed to be sensitive to the nuclear interactions: water and PMMA targets with the same WET thicknesses (see Table 6.1) were irradiated with a 430 MeV/u carbon ion beam. The ion spectra and the lateral particle distributions behind the targets were analysed. Only particles in the second detector at lateral distances $\leqslant$0.35 cm to the corresponding primary particle position in the first detector were considered.

As shown in Figure 6.1, the amounts of carbon ions detected behind coupled targets were found to be consistent, within the uncertainties, in the experiments. However, broader lateral distributions were observed for the carbon ions behind water than PMMA targets. Differences up to 10% in the mean lateral distances, d^C_{mean}, for the thickest targets were found (see Figure 6.11). Since the differences in the WETs between coupled targets were found not to influence the results significantly (see Section 6.5.2 and Section 7.2.1), the differences observed in the results should be mainly related to the different geometrical thicknesses and chemical compositions between the targets. Indeed, as Table 6.1 shows, the PMMA phantoms are thinner than the corresponding water targets and the absolute differences increase with increasing target thickness.

Based on the results achieved, the use of PMMA in place of water phantoms in dosimetry would enable a correct assessment of the percentage of residual carbon ions. Nevertheless, a slight underestimation of the lateral beam spread may occur. This could lead to an overestimation of the dose delivered close to the beam axis and an underestimation of the dose deposited at greater distances to it.

The carbon ion attenuation curves obtained from the simulated data have a different slope than the experimental ones, both for water and PMMA targets (as shown in Figure 6.1). However, the sharper distance distributions found in FLUKA (see Figure 6.8 and Figure 6.11) cannot explain the higher amount of carbon ions registered behind the targets in the simulations. As Figure 6.8 shows, the amount of carbon ions detected in the second detector decreases quickly with increasing lateral distances to the primary particle positions in the first detector: within the range of lateral distances investigated (0 cm - 0.35 cm), reductions between 2 and 5 order of magnitude, depending on the target thickness, were observed. Hence, the cut on the maximal lateral distance should not affect the results for the primary particles strongly, especially in the case of thinner targets where the lateral beam spread is lower. Instead, the greatest differences (6%) in the amount of outgoing carbon ions detected in the experiments and in the simulations were found for the thinnest water and PMMA targets.

The influence on the results of a residual detector misalignment, which was investigated in Section 6.5.1, cannot fully explain the differences observed between the experiments and the simulations. In Table 6.11 the d^C_{mean} values obtained shifting the first detector

in different positions are shown. One can see that the fluctuations on the experimental data are $\leqslant 4\%$, whereas the differences between the d^C_{mean} values determined in the experiments and in FLUKA are 17%. Furthermore, 4% represents the upper limit of the uncertainties which should be considered in the experiments, as it was obtained in the worst case scenario.
Other experimental inaccuracies, which could affect the experiments but not the simulations, were considered and their significant effects on the results were excluded by means of the data analysis method (described in Section 5.4).

Similar shapes in the number of secondary fragments detected as a function of the target thickness were observed for measurements with the water and the PMMA targets. However, more particles were detected behind the PMMA targets. The greatest differences (~20%) were found for the lighter particles. The sharper lateral distance distributions observed behind the PMMA than the water targets (see Figure 6.12 and Figure 6.13) might cause the lower amount of fragments registered behind the water targets. Hence, the different geometrical thickness and chemical composition between water and PMMA could influence the resulting secondary fragments and their trajectories significantly.
If PMMA is used in place of water for dosimetric measurements, an overestimation of the dose delivered by the secondaries close to the beam axis may result, while the contribution to the dose from secondary particles traveling at great angles could be underestimated.
However, light fragments, which are produced more abundantly than heavier fragments, contribute to the delivered dose with lower LET components than the heavier particles. On the other hand, due to their broader lateral distributions, light fragments may travel more far away from the beam axis and from the tumor. A deeper knowledge on the particles traveling at great angles would be particularly advantageous to better estimate the unwanted side effects on the healthy tissues.

The results in Section 6.2.1 show that more fragments were measured in the simulations than in the experiments. However, like the experiments, a higher amount of fragments were registered behind the PMMA than the water targets.
Further investigations on the modeling of the experimental setup, accuracy of the phase space, particle transportation and fragment productions would contribute to better understand the observed differences between the experiments and the simulations. The gained knowledge could then be used to improve the particle interaction models implemented in the Monte Carlo algorithms.

7.5 Fragmentation of Helium Ions in Water and in PMMA

Helium ion beams were investigated due to their potential for future applications in radiotherapy [Mairani, Tessonnier, and Dokic 2016]. The interest on these particles is indeed growing fast in the last years, as they can offer advantages to both protons and carbon ions, such as a sharper penumbra than protons and a smaller fragmentation tail than carbon ions. Radiotherapy treatments with these particles are planned to start at HIT in 2017 [Mairani, Tessonnier, and Dokic 2016]. However, the lack of experimental data to benchmark the Monte Carlo codes is an issue for helium ions even more than for carbon ions. It follows an urgent need to improve the physical beam models for helium ions.

In this work the nuclear interactions of a 221 MeV/u helium ion beam in water and in PMMA targets with the same WET thicknesses (see Table 6.1) were analysed. The ion spectra and the lateral particle distributions behind the targets were investigated. All the particles registered behind the targets at a distance $\leqslant$0.35 cm to the corresponding primary particle position in front of the target were analysed.

The amount of helium ions detected in the experiments behind the water and the PMMA targets were found to be consistent within their uncertainties, except for the thickest targets, where differences of 2% were measured (see Figure 6.14). Similar to the measurements with carbon ion beams, significant differences in the lateral distance distributions of the helium ions were found for coupled targets: as Figure 6.18 shows, the differences in the d_{mean}^{He} values increase with increasing target thicknesses, up to 8%. Therefore, also in this case, some limits in the equivalence between water and PMMA regarding nuclear interactions were found. If PMMA is used in place of water in dosimetry, differences in the calculations of the dose distributions could arise, especially with thick targets.

In this thesis a new version of FLUKA still under development was used to reproduce the experiments with helium ion beams. With respect to the version currently available, FLUKA 2011.2c.4, an improving agreement between the experiments and the simulations was observed, both in the amount of helium ions detected behind the targets and in the lateral particle distributions. However, the amounts of helium ions detected behind the targets were found to be between 3% and 8% higher in the simulations than in the experiments. The lateral distributions were narrower in the simulations, especially for the thinnest targets where the d_{mean}^{He} values were about 20% smaller.

Regarding the secondary H, the experimental results were rather well reproduced by FLUKA.

The present work might contribute to provide some of the missing knowledge regarding the nuclear interactions of helium ion beams in water and in PMMA. However, the results achieved here should be complemented by further investigations and measurements, in order to cover a wider range of particle energies and phantom configurations of interest for medical applications.

7.6 Fragmentation of Carbon Ions in Tissue and in Water

The nuclear interactions of carbon ion beams were investigated in tissue surrogates (lung, adipose, inner bone and cortical bone) and in water phantoms with the same WETs (see Table 6.2). For this study, beam energies suitable for standard treatments of prostate and lung tumors were used, as reported in Table 5.1).

Consistency in the number of carbon ions detected behind the tissue equivalent materials and the corresponding water targets was found within the experimental uncertainties, as shown in Figure 6.20. The mean lateral distances determined for the carbon ions, d^C_{mean}, were found to be in agreement within the uncertainties in the case of Adipose and Inner Bone with respect to their equivalent water phantoms (Figure 6.25). On the contrary, significant differences were observed for Lung and Cortical Bone with respect to the water targets: the differences in the d^C_{mean} were +7% for Lung and -8% for Cortical Bone. Higher discrepancies were expected for these two tissue surrogates, as the WEPLs of Lung and Cortical Bone differ from the value of 1 more than the WEPLs of Adipose and Inner Bone (values are listed in Table 6.2).
For the number of secondary particles detected behind the targets and for the lateral fragment distributions, the greatest differences occurred again between Lung and Water(Lung) and between Cortical Bone and Water(Cortical Bone). The worst case was measured between Lung and Water(Lung) and for the light H fragments, were differences up to 42% were achieved while the statistical uncertainties were 5%.
This study showed that a satisfactory equivalence between water and soft tissues like adipose and inner bone, for the investigated target thicknesses and beam energy, takes place. However, tin case of lung and bony structure, the heavier elements present in the lung and cortical bone surrogates with respect to water (see Table 4.3), and the great differences in the target thicknesses (+71% for Lung and -63% for Cortical Bone) may influence the outgoing particle spectra significantly.

In the simulations, more carbon ions were detected behind all the targets (Figure 6.20), with differences up to 10% in the case of Lung. The lateral distance distributions of the carbon ions were broader in FLUKA: differences between 12% (for Cortical Bone) and 35% (for Lung) in the d^C_{mean} values were measured (see Figure 6.25). However, those differences cannot be entirely due to a residual detector misalignment and to the cut on the maximum lateral distance considered (0.35 cm). Indeed, as an example, the influence of experimental uncertainties on the d^C_{mean} obtained with the Lung target was estimated to be less than 2%, whereas the difference between the d^C_{mean} values determined in the experiments and in the simulations is 35%.
Other factors that could cause the differences observed between the experiments and the simulations are inaccuracies in the model of the experimental setup (targets, detectors, beam line) and inaccuracies in the nuclear interaction models.

8 Conclusions and Outlook

Ion radiotherapy enables a more conformal dose distribution to the target than conventional radiotherapy with photons. The prescribed dose can be delivered in deep-seated tumors while the dose to normal tissues is lower. Protons and carbon ions are currently used for radiotherapy treatments, and the interest on helium ions is growing fast. The main advantages of helium and carbon ions with respect to protons are a narrower penumbra, a sharper Bragg peak, and a greater relative biological effectiveness. Moreover, helium ions can provide a more conformal dose to the tumor than protons, and a lower risk of secondary tumors, particularly relevant in case of pediatric patients, than carbon ions. However, the choice of the primary particle is in fact very specific. Factors like α and β values, prescribed dose level and desired end point has to be considered each time [Grün et al. 2015].

The carbon and helium ion fragmentations within the patient tissues may influence the delivered biological dose significantly. The fragmentation processes result in a spectrum of lighter particles with different physical and biological properties than the primary ions. In Kempe, Gudowska, and Brahme 2007 it was calculated that, for a 391 MeV/u ^{12}C beam, the secondary fragments contribute up to 40% to the total dose in front of the Bragg peak; for a 200 MeV/u ^{4}He beam, the secondary particles contribute to the total delivered dose by about 20%. Since healthy tissues are usually located in front of the Bragg peak, the secondary fragments need to be considered in the treatment planning systems to reduce the risks of short- and long-term side effects.

Several studies were performed to investigate the secondary fragments arising in carbon and helium ion beams crossing water and PMMA targets (e.g. [Gunzert-Marx et al. 2008, Haettner et al. 2013, Matsufuji et al. 2011], Krämer et al. 2016). However, until now, a limited range of beam energies and target thicknesses have been investigated.
In this thesis a new experimental method was developed, which makes use of the pixelated semiconductor Timepix detectors. These detectors provide high detection efficiency for charged particles, fast data acquisition, and enable very versatile and small experimental setups. The new method presented in this thesis is promising to investigate the fragment spectra and the lateral particle distributions for therapeutic ion beams, and to gain more detailed information and extra data regarding ion interactions with matter.

Three main studies were carried out:

- **Study 1**: *Fragmentation of Carbon Ions in Water and in PMMA* (Section 6.2)
- **Study 2**: *Fragmentation of Helium Ions in Water and in PMMA* (Section 6.3)
- **Study 3**: *Fragmentation of Carbon Ions in Tissue and in Water* (Section 6.4)

All the outgoing particles detected behind the phantoms at a lateral distance smaller than 0.35 cm to the corresponding primary particle position in front of the targets were considered. Beam attenuation, build-up of secondary particles and lateral particle distributions were analysed and compared for different target materials. As the targets have in pairs the same WET, a direct comparison of the results was possible.

The most relevant findings achieved in the **experiments** are briefly summarized in the following:

- In all three studies, for targets with the same WET, the numbers of primary particles (helium or carbon ions) detected behind the water and the PMMA targets were found to be consistent within the uncertainties.
- Both in the measurements with carbon and with helium ion beams, more secondary fragments (up to 20% in the case of H) were detected behind the PMMA than the water targets in the forward region investigated. That was shown to be partially due to the narrower lateral particle distributions observed behind the PMMA targets.
- A good equivalence between adipose and inner bone surrogates with respect to the corresponding water targets was observed, as regards the fluence of the outgoing ions and the lateral particle distributions. Significant differences were instead measured in the case of Lung and Cortical Bone with respect to the water phantoms. For instance, -42% and +14% of H were detected behind Lung and Cortical Bone, respectively, than in the corresponding water phantoms. However, it should be noted that H contributes with lower LET and therefore with lower RBE to the biological delivered dose than heavier particles.

The differences observed in the experimental results between coupled targets were shown not to be due to the differences in the WETs. The WETs of coupled targets indeed differ by less than 0.5% and these differences did not influence the results significantly, as it was demonstrated in Section 6.5.2.
The findings achieved in this thesis show that:

1) Both in the measurements with carbon and helium ion beams, a more confined dose may result using PMMA in place of water for dosimetric purposes. This effect becomes more relevant with increasing target thickness.
2) The differences in the chemical composition and target thickness between tissue surrogates and water could influence the calculated dose distributions significantly. This work might contribute to improve the accuracy of the conversion between dose to water and dose to tissue.

Monte Carlo **simulations** of the experiments were carried out with the FLUKA code, which is currently used at HIT (Heidelberg, Germany) and at CNAO (Pavia, Italy) to support and to validate clinical calculations in proton and carbon ion treatments [Battistoni et al. 2016]. The findings achieved by the comparison between the experimental and the simulated data are summarized here:

- In all three studies, a lower amount of primary ions (helium or carbon ions) behind the targets was found in the simulations. The greatest differences were measured for the thinnest targets, 5 $\mathrm{cm_{WET}}$, in Study 1 ($\sim$6%), for the thickest targets, 18 $\mathrm{cm_{WET}}$, in Study 2 ($\sim$8%), and for Lung in Study 3 ($\sim$11%).
- In all three studies, more light fragments (relative differences up to 50% for the lightest fragments, H) at a lateral distance to the corresponding primary particle position in front of the target smaller than 0.35 cm were found in FLUKA.
- The lateral particle distributions were in general narrower in the simulations in the first two studies (*Fragmentation of Carbon/Helium ions in Water and in PMMA*), and broader in the third study (*Fragmentation of Carbon ions in Tissue and in Water*). However, the differences between the experiments and the simulations tend to decrease with increasing target thickness.

It was shown in Section 6.5.1 that a residual detector misalignment cannot fully explain the differences observed between the experiments and the simulations. Other factors which could contribute to those differences are:

- inaccuracies in the geometrical model of the experimental setup (e.g. in the detectors and in the chemical compositions and densities of the targets);
- inaccuracies in the simulation of the incoming particle beam (phase-space);
- differences in the probabilities to produce a certain amount and type of fragments from the nuclear interaction processes, between the experiments and the simulations;
- differences in the momentum transferred and in the particle scattering, between the experiments and the simulations.

The analysis of the amount and type of fragments detected from each single primary carbon ion, presented in Section 6.2.1, showed that a greater amount of multiple light fragments (H, He) were detected in the simulations. These unique results, together with the studies on the lateral particle distributions, might contribute to identify the source of the differences observed between the experiments and the simulations.

Outlook

in the first two studies (*Fragmentation of Carbon/Helium ions in Water and in PMMA*) the highest beam energies available at HIT (430 MeV/u in the case of carbon ions, and 221 MeV/u in the case of helium ions) were used. These energies were chosen as the contribution of the fragments is more relevant with increasing initial beam energy. Future measurements should be carried out with different beam energies, target thicknesses and elemental compositions. Moreover, the secondary fragments should be investigated also behind the Bragg peak. The detectors could also be rotated with respect to the beam axis to cover a wider solid angle. The further information gained by those studies would enable to better estimate the contributions of the different particles species to the delivered physical and biological dose, and therefore to evaluate the side effects during and after the radiotherapy treatments with higher accuracy.

This research could also strongly benefit from two new technologies currently under development: larger detectors and the new generation of Timepix detectors (Timepix 3). Larger detectors would allow to investigate broader lateral distributions. They would be particularly advantageous for the lighter particles, which can travel at greater distances to the beam axis. These light fragments are the major responsible of damage in the healthy tissues surrounding the tumor. Moreover, as the lateral particle distributions become broader with increasing target thickness, thicker targets could be investigated without a significant loss of fragments traveling out of the detection area.
With the Timepix 3, measurements in Time- and in ToT-mode can be performed simultaneously in each individual pixel [Poikela, Plosila, and Westerlund 2012, Campbell et al. 2016]. Therefore, just one detector behind the targets would be sufficient, enabling to reduce the amount of materials along the particle paths, and also to simplify the particles matching process and the geometry of the experimental setup in the simulations. Consequently, the influence on the final results of ion interactions in the detectors and of experimental uncertainties, such as detector misalignments, could be decreased.

Bibliography

Ahlen, S.P. (1980). "Theoretical and experimental aspects for the energy loss of relativistic heavily ionizing particles". In: *Rev. Mod. Phys.* ***52****: 121-173.*

Allen, A.M. et al. (2012). "An evidence based review of proton beam therapy: The report of ASTRO's emerging technology committee". In: *Radiother. and Oncol.* ***103(1)****: 8-11.*

Amaldi, U. and G. Kraft (2005). "Radiotherapy with beams of carbon ions". In: *Rep. Prog. Phys.* ***68****: 1861-1882.*

Andreo, P. et al. (2000). *Absorbed Dose Determination in External Beam Radiotherapy: An International Code of Practice for Dosimetry based on Standards of Absorbed Dose to Water - Technical Reports Series no. 398.* IAEA.

Battistoni, G. et al. (2007). "The FLUKA Code: description and benchmarking". In: *Proceedings of the Hadronic Shower Simulation Workshop, Fermilab 6–8 September 2016, A. Albrow, R. Raja eds., AIP Conference Proceeding 896: 31-49.*

Battistoni, G. et al. (2016). "The FLUKA Code: An Accurate Simulation Tool for Particle Therapy". In: *Front. Oncol.* ***6****(116): 1-24.*

Bentzen, S.M. et al. (2008). *Radiation Oncology Advances.* Springer. ISBN: 978-0387-36743-9.

Bethe, H.A. (1952). "Moliere's Theory of Multiple Scattering". In: *Physical review* ***89****(6):1256-1266.*

Böhlen, T. et al. (2010). "Benchmarking nuclear models of FLUKA and GEANT4 for carbon ion therapy". In: *Phys. Med. Biol.* ***55****: 5833-5847.*

Böhlen, T. et al. (2013). "A Monte Carlo-based treatment-planning tool for ion beam therapy". In: *J. Radiat. Res.* ***54****(1): i77-i81.*

Böhlen, T.T. et al. (2014). "The FLUKA Code: Developments and Challenges for High Energy and Medical Applications". In: *Nucl. Data Sheets* ***120****: 211-214.*

Bouchami, J. et al. (2009). "Study of charge sharing in a silicon pixel detector with heavy ionizing particles interacting with a Medipix2 device". In: *Nucl. Instr. and Meth.* ***A 607****: 196-198.*

Bouchami, J. et al. (2010). "Measurement of pattern recognition efficiency of tracks generated by ionizing radiation in a Medipix2 device". In: *Nucl. Instr. and Meth.* ***A 633****: 187-189.*

Campbell, M. et al. (2008). "Study of the charge sharing effect in a silicon pixel detector by means of α-particles interacting with a Medipix2 device". In: *Nucl. Instr. and Meth.* ***A 591****: 38-41.*

Campbell, M. et al. (2016). "Towards a new generation of pixel detector readout chips". In: *JINST* ***11****: C01007.*

Castro, J.R. et al. (1996). “15 years of experience with helium ion radiotherapy for uveal melanoma”. In: *Rad. Oncol. Bio. Phys.* ***36****(1): 200.*

Chen, G.T.Y., J.R. Castro, and J.M. Quivey (1981). “Heavy charged particle radiotherapy”. In: *Annu. Revc. Biophys. Bioeng.* ***10****: 499-529.*

Combs, S.E. et al. (2010a). “Heidelberg Ion Therapy Center (HIT): Initial clinical experience in the first 80 patients”. In: *Acta Oncologica* ***49****: 1132-1140.*

Combs, S.E. et al. (2010b). “Particle therapy at the Heidelberg Ion Therapy Center (HIT) - Integrated research-driven university-hospital-based radiation oncology service in Heidelberg, Germany”. In: *Radiother. Oncol.* ***95****: 41-44.*

Combs, S.E. et al. (2012). “Treatment of pediatric patients and young adults with particle therapy at the heidelberg Ion Therapy Center (HIT): establishment of workflow and initial clinical data”. In: *Rad. Onc.* ***7****: 170.*

Ferrari, A. et al. (2005). “FLUKA: a multi-particle transport code”. In: *Technical Report, CERN-2005-10, INFN/TC 05/11, SLAC-R-773.*

Fowler, P.H. and D.H. Perkins (1961). “The possibility of therapeutic application of beams of negative pi-mesons”. In: *Nature* ***189****: 524-528.*

Gallas, R.R. (2016). “A Novel Method for Assessment of Beam-Tissue Interactions in Helium Ion Radiotherapy”. Master’s thesis, University of Heidelberg.

Garciá-Ramos, J.-E. et al. (2015). *Basic Concepts in Nuclear Physics: Theory, Experiments and Applications.* Springer International Publishing. ISBN: 978-3-319-21190-9.

Granja, C. et al. (2007). “Position-sensitive spectroscopy of ^{252}Cf fission fragments”. In: *Nucl. Instr. and Meth.* ***A 574****: 472-478.*

Grün, R. et al. (2015). “Assessment of potential advantages of relevant ions for particle therapy: a model based study”. In: *Med. Phys.* ***42****: 1037.*

Gunzert-Marx, K. et al. (2008). “Secondary beam fragments produced by 200 MeV u^{-1} ^{12}C ions in water and their dose contribution in carbon ion radiotherapy”. In: *New J. Phys.* ***10****: 075003.*

Gwosch, K. (2012). “Non-Invasive Monitoring of Carbon Ion Beam Therapy by Tracking of Secondary Ions - An Initial Study”. Diploma’s thesis, University of Heidelberg.

Gwosch, K. et al. (2013). “Non-invasive monitoring of therapeutic carbon ion beams in a homogeneous phantom by tracking of secondary ions”. In: *Phys. Med. Biol.* ***58****(11): 3755-3773.*

Haberer, T. et al. (1993). “Magnetic scanning system for heavy ion therapy”. In: *Nucl. Instr. and Meth.* ***A 330****(1-2): 296-305.*

Haberer, T. et al. (2004). “The Heidelberg ion therapy center”. In: *Radiother. Oncol.* ***73****(2): S186-190.*

Haettner, E. (2006). “Experimental study on carbon ion fragmentation in water using GSI therapy beams”. Master’s thesis, Kungliga Tekniska Hogskolan Stockholm.

Haettner, E. et al. (2013). “Experimental study of nuclear fragmentation of 200 and 400 MeV/u (12)C ions in water for applications in particle therapy”. In: *Phys. Med. Biol.* ***58****(23): 8265-8279.*

Hartmann, B. (2013). “A Novel Approach to Ion Spectroscopy of Therapeutic Ion Beams using a Pixelated Semiconductor Detector”. PhD thesis, University of Heidelberg.

Hartmann, B. et al. (2012). “Towards fragment distinction in therapeutic carbon ion beams: A novel approach using the Timepix detector”. In: *IEEE Nucl. Sci. Symp. Med. Imag. Conf.: 4076-4079.*

Highland, L. (1975). “Some practical remarks on multiple scattering”. In: *Nucl. Instr. and Meth.* ***129****(2): 497-499.*

Holy, T. et al. (2008). “Pattern recognition of tracks induced by individual quanta of ionizing radiation in Medipix2 silicon detector”. In: *Nucl. Instr. and Meth.* ***A 591****: 287-290.*

Jäkel, O. (2008). “The relative biological effectiveness of proton and ion beams”. In: *Z. Med. Phys.* ***18****: 276-285.*

Jäkel, O., C. Karger, and J. Debus (2008). “The future of heavy ion radiotherapy”. In: *Med. Phys.* ***35****(12): 5653-5663.*

Jäkel, O. et al. (2001). “Relation between carbon ion ranges and x-ray CT numbers”. In: *Med. Phys.* ***28****(4): 701-703.*

Jakubek, J. (2009a). “Energy-sensitive X-ray radiography and charge sharing effect in pixelated detector”. In: *Nucl. Instr. and Meth.* ***A 607****: 192-195.*

– (2009b). “Semiconductor Pixel detectors and their application in life sciences”. In: *JINST* ***4****: P03013.*

– (2010). “Precise energy calibration of pixels detector working in time-over-threshold mode”. In: *Nucl. Instr. and Meth.* ***A 633****: S262-S266.*

Jakubek M., Jakubek J. et al. (2013). “3D imaging of radiation damage in silicon sensor and spatial mapping of charge collection efficiency”. In: *JINST* ***8****: C03023.*

Joiner, M. and A. van der Kogel (2009). *Basic Clinical Radiobiology.* Hodder Arnold. ISBN: 978-0-340-929-667.

Kamada, T. et al. (2015). “Carbon ion radiotherapy in Japan: an assessment of 20 years of clinical experience”. In: *The Lancet Oncology* ***6****(2): e93-e100.*

Kempe, J., I. Gudowska, and A. Brahme (2007). “Depth absorbed dose and LET distributions of therapeutic ^{1}H, 41He, ^{7}Li and ^{12}C beams”. In: *Med. Phys.* ***34****(1): 183-192.*

Kraft, G. (1999). “RBE and its interpretation”. In: *Strahlenther. Onkol* ***175****(II): 44-47.*

Krämer, M et al. (2016). “Helium ions for radiotherapy? Physical and biological verifications of a novel treatment modality”. In: *Med. Phys.* ***43****(4): 1995-2004.*

Landau, L. (2007). “On the energy loss of fast particles by ionization”. In: *J. of Phys.* ***8****: 201-2015.*

Linz, U. (2012). *Ion Beam Therapy: Fundamentals, Technology, Clinical Applications.* Springer. ISBN: 978-3-642-21413-4.

Llopart, X. et al. (2007). “Timepix, a 65k programmable pixel readout chip for arrival time, energy and/or photon counting measurements”. In: *Nucl. Instr. and Meth.* ***A 581****: 485-494.*

Lühr, A. et al. (2011). “Fluence correction factors and stopping power ratios for clinical ion beams”. In: *Acta Onc.* ***50****: 797-805.*

Ma, C.-M.C. and T. Lomax (2012). *Proton and Carbon Ion Therapy (Imaging in Medical Diagnosis and Therapy).* CRC. Press. ISBN: 978-1-4398-1607-3.

Mairani, A, T. Tessonnier, and I. Dokic (2016). “Biological optimization for helium ion plans”. In: *medicalphysicsweb.*

Mairani, A. et al. (2016). “Biologically optimized helium ion plans: calculation approach and its *in vitro* validation”. In: *Phys. Med. Biol.* ***61**: 4283-4299.*

Marcu, L., E. Bezak, and B. Allen (2012). *Biomedical physics in radiotherapy for cancer.* Springer. ISBN: 978-0-85729-732-7.

Matsufuji, N. et al. (2003). “Influence of fragment reaction of relativistic heavy charged particles on heavy-ion radiotherapy”. In: *Phys. Med. Biol.* ***48**: 1605-1623.*

Matsufuji, N. et al. (2011). “Spatial fragment distribution from a therapeutic pencil-like carbon beam in water”. In: *Phys. Med. Biol.* ***50**: 3393-3403.*

Meroli, S., D. Passeri, and L. Servoli (2011). “Energy loss measurement for charged particles in very thin silicon layers”. In: *JINST **6**:P06013.*

Pinsky, L.S. et al. (2011). “Penetrating heavy ion chargeand velocity discrimination with a TimePix-based Si detector (for space radiation applications)”. In: *Nucl. Instr. and Meth. **A 633**(1): S190-S193.*

Poikela, T., J. Plosila, and T. Westerlund (2012). “Architectural modeling of pixels readout chips Velopix and Timepix3”. In: *J. of Instr. **7**:C01093.*

PTCOG-website (2016). *Facility in operation.* Last access: 10 September 2016. URL: `url=http://www.ptcog.ch/index.php/facilities-in-operation`.

Reinhart, M. (2014). “Monitoring of Therapeutic Ion Beams - Secondary Particle Track Yield Measurements and 3D Reconstruction Techniques”. Master’s thesis, University of Heidelberg.

Rieken, S. et al. (2012). “Proton and carbon ion radiotherapy for primary brain tumors delivered with active raster scanning at the Heidelberg Ion Therapy Center (HIT): early treatment results and study concepts”. In: *Radiat. Oncol. **7**: 41.*

Sánchez Parcerisa, D. (2012). “Experimental and computational investigation on the water-to-air stopping power ratio for ion chamber dosimetry in carbon ion radiotherapy”. PhD thesis, University of Heidelberg.

Schall, I. et al. (1996). “Charge-changing nuclear reactions of relativistic light-ion beams ($5 \leqslant Z \leqslant 10$) passing through thick absorbers”. In: *Nucl. Instr. and Meth. in Phys. Res. **B 117**: 221-234.*

Schardt, D., T. Elsässer, and D. Schulz-Ertner (2010). “Heavy-ion tumor therapy: Physical and radiobiological benefits”. In: *Rev. Mod. Phys. **82**(1): 383-425.*

Schardt, D. et al. (1995). “Nuclear fragmentation of high-energy heavy-ion beams in water”. In: *Adv. Space Rev. **17**: 87-94.*

Schlegel, W., T. Bortfeld, and A.-L. Grosu (2006). *New Technologies in Radiation Oncology.* Springer. ISBN: 978-3-540-00321-2.

Schulz-Ertner, D., O. Jäkel, and W. Schlegel (2012). “Radiation Therapy with Charged Particles”. In: *Semin. Radiat. Oncol. **22**: 170-178.*

Ströbele, J. et al. (2006). “Comparison of basic features of proton and helium ion pencil beams in water using GATE”. In: *Z. Med. Phys. **16**: 249-259.*

Tessonnier, T. et al. (2015). “Experimental dosimetric comparison at Heidelberg ion beam therapy center of 1H, 4He, 12C and 16O ion beam”. In: *Phys. Med.: Eur. J. Med. Phys. **31** e26-27.*

Tessonnier, T. et al. (2016). “Phase Space Generation for Proton and Carbon ion Beams for External Users’ Applications at the Heidelberg Ion Therapy Center”. In: *Front. Oncol.* ***5****(297): 1-15.*

Tobias, C.A. et al. (1964). “Response of the Nervous System to Ionizing Irradiation”. In: *Progress Report on Pituitary Irradiation.* ed. by Haley T.J., Snider R.S., 19-35.

Tsai, Y.-S. (1974). “Pair production and bremsstrahlung of charged leptons”. In: *Rev. of Modern Phys.* ***46****: 815-851.*

Turecek, D. et al. (2011). “Small Dosimeter based on Timepix device for International Space Station”. In: *J. of Instr.*

Vykydal, Z. et al. (2009). “The Medipix2-based network for measurement of spectral characteristics and composition of radiation in ATLAS detector”. In: *Nucl. Instr. and Meth.* ***A 607****: 35-37.*

Wilson, R.R. (1946). “Radiological use of fast protons”. In: *Radiology* ***47****: 487-491.*

Zeitling, C. et al. (2007). “Fragmentation cross sections of 290 and 400 MeV/nucleon ^{12}C beams on elemental targets”. In: *Physical Review* ***C 76****: 014911.*

Acknowledgments

In the following I would like to express my gratitude to all people who supported me during my PhD work, professionally and morally during my PhD work.

I am thankful to Prof. Dr. Jürgen Debus, medical director of the department of Radiation Oncology and Radiation Therapy at the Heidelberg University Medical Center, who employed me within his division.
I also thank Prof. Dr. Wolfgang Schlegel, senior scientist in the department of Medical Physics in Radiation Oncology at DKFZ, for accepting to be the first referee of this thesis.
Furthermore, I wish to thank Prof. Dr. Oliver Jäkel, head of the department of Medical Physics in Radiation Oncology at DKFZ, for supporting and encouraging me to take part in important scientific conferences where I could show the results of my research work.
Prof. Dr. Oliver Jäkel, together with Prof. Dr. Christian Karger, group leader of the research group Applied Medical Radiation Physics at DKFZ, and with Prof. Dr. Schultz-Coulon, professor at the University of Heidelberg, provided me with useful and stimulating advices to carry out my PhD project. I really thank them for their time during the thesis advisory committee meetings.
Furthermore, I wish to thank Prof. Dr. Schultz-Coulon and Prof. Dr. Joerg Jaeckel, professor at the University of Heidelberg, for serving as members in my final examination committee.

Particularly, I wish to thank Prof. Dr. Mária Martišiková, group leader of the research group Novel Detection Techniques for Ion Beams at DKFZ, for giving me the opportunity to develop this project, for her advices, support and research inspirations in the past years, and also for the careful proofreading of this thesis.

I am thankful to the colleagues at the IEAP and Advacam s.r.o. company in Prague, for their help and support with the Timepix detectors. Above all, I thank Dr. Ing. Jan Jakubek, Dr. Ing. Carlos Granja, Ing. Daniel Tureček and Lukáš Opalka.

I wish to thank all the colleagues at HIT who collaborated with me and contributed to make this project possible. In particular, many thanks to: Dr. Stephan Brons for arranging the beam time and supporting me with important scientific information; Dr. Andrea Mairani for discussing with me the results from the FLUKA simulations and for his important hints; Thomas Tessonnier for his help with the FLUKA simulations and also for the pleasant time at PTCOG54 and afterwards.

My gratitude is also addressed to Dipl.-Ing. Gernot Echner and Armin Runz from the research group Medical Engineering at DKFZ, and to the mechanical workshop in general, for building the phantoms which were used in this research work.

Thanks also to Prof. Naruhiro Matsufuji, team leader of Radiation Effect Research Team in the Medical Physics Research Program at NIRS, for hosting me at NIRS/HIMAC. I am sincerely grateful to him, to Dr. Chie Toramatsu and to the whole research group for their help and support during my stay in Japan and during the beam time.

I am very happy of all the colleagues I met in the last years within the research groups E0406, E0408, E0409 at DKFZ. They contributed to make this experience more enjoyable. Above all, I want to thank Dr. Bernadette Hartmann, who particularly supported me at the beginning of this project, and Tim Gehrke, for the interesting professional talks and his continued willingness to help whenever I needed. I am particularly grateful to the group members of E0406, who supported me during the exhausting measurements at HIT. Their contribution was utterly relevant for the development of this work. Thanks also to Shirin Rahmanian for the proofreading of this thesis, and to Kathrin Spindeldreier for helping me in the German learning process and for having been an amazing office mate.

I want to thank all my friends in Heidelberg, for all the pleasant moments and activities we shared in the last years. You have been a such amiable, warm and international crew that I will strongly miss in the future. A special thank to Karin Mössenböck, who first welcomed and introduced me into the friend group.

I dedicate this thesis to my family. Nonostante la distanza, il vostro affetto, supporto e incoraggiamento non sono mai mancati nella mia vita. E solo voi sapete quante difficoltà ho incontrato.